Viscoelastic Braided Stent: Finite Element Analysis and Validation of Crimping Behaviour

UNIVERSITY of LIMERICK

OLLSCOIL LUIMNIGH

Camelia Shanahan

Bernal Institute

School of Engineering & School of Natural Sciences

University of Limerick

Ireland

Supervisors:

Dr. Peter Tiernan

Dr. Syed A.M. Tofail

Submitted to the University of Limerick for the degree of

Philosophiae Doctor (Ph.D.) March 2017

Abstract

In this thesis, validated Finite Element (FE) models for a viscoelastic braided stent are created, to investigate the mechanical behaviour of the stent subjected to crimping and to predict the stent's radial forces. The research is focused on developing and validating two linear viscoelastic material models: one for Polydioxanone, a biodegradable polymer and one for Nitinol, a Nickel Titanium shape memory alloy. Both models are developed using Abaqus, a commercial FE software package. The existing analytical model is corrected and adapted to include the braiding angle as opposed to the pitch angle. The model is also extended by introducing additional design information such as the mandrel design to enable correct fabrication, the braid cover factor and the condition in which the braid is in jammed state. A tensile test and tensile creep experiment are performed on the polymer monofilament in order to characterise its viscoelastic response. Data acquired are used to calibrate the polymer material model. Two experiments are performed on the Nitinol material: a uniaxial tensile test to capture its superelastic-plastic behaviour and a Discrete Scanning Calorimeter analysis to investigate its transformation temperatures. Data acquired alongside creep data available in the literature are used to calibrate the Nitinol viscoelastic material model. Finally, both viscoelastic configurations of the FE models for the braided stent used in a crimping simulation are validated experimentally on in-house built prototypes. The outcomes of the study demonstrate the great benefits in using FE analysis to assess the mechanical behaviour of a viscoelastic braided stent during crimping. The viscoelastic material model developed for Polydioxanone shows an improvement in the accuracy of the stent's mechanical behaviour in comparison to a purely elastic material model. The viscoelastic model developed for Nitinol predicts the radial resistive forces more accurately; however, overall, the superelastic-plastic model gives more accurate estimations. The significance of the work is in confirming the effectiveness of using FE method in the braided stent analysis and in helping design engineers to better understand the mechanical behaviour of the viscoelastic braided stent and therefore to better optimise its design for particular clinical applications.

Dedication

This thesis is dedicated to my loving husband John, who encouraged and supported me every single step of the way. Thank you for your patience, this journey would not have been possible without you.

To my son Ethan, who every single week never failed to ask me about my progress. I'm delighted that my interests in technology have rubbed off on you. Dream big and dare to imagine a better you every day!

To my mum, who has stood by me through all life's storms.

To my dad, I hope you are up there watching over me.

Declaration

I, Camelia Shanahan, hereby declare that the content of this report is the product of my own work. All sources of information used as references are duly acknowledged. This material has not been previously submitted to any University for any type of academic degree and has not been previously published.

_____

Camelia Shanahan

Acknowledgments

First of all, I would like to express my sincere appreciation to my academic supervisor Dr. Peter Tiernan, for his guidance throughout the programme and for giving me the opportunity to work in the exciting field of implantable devices. I would also like to thank my co-supervisor Dr. Syed Tofail, for the valuable time and for his help in bringing this work to a satisfactory conclusion.

I would also like to thank the following:

The technical staff of the Design & Manufacturing Technology department: Jimmy Quinn, Tom Byrnes, Seamus Mason, Ger O'Connor, Kevin O'Flanagan and Seamus Harrold for their expertise in manufacturing technologies

Dr. David Tanner for his advice on FEA

Dr. Karrina McNamara and Ms. Nuala Kitson for their administrative assistance

Dr. Aidan Cloonan for his help with the DSC analysis

Mr. Adrian McEvoy for his assistance with the experimental testing

Aimee Stapleton, Mohamed Jushiddi, Mahendar Kumbham and all the members of MOSAIC research group for their support.

Table of Contents

Table of Figures

List of Tables

List of Publications

Published Research Papers (Appendix 4)

C. Shanahan, S.A.M. Tofail, P. Tiernan, 'Viscoelastic braided stent: Finite element modelling and validation of crimping behaviour', *Materials & Design* (2017), doi:10.1016/j.matdes.2017.02.044.

Research Papers under peer review

C. Shanahan, P. Tiernan, S.A.M. Tofail, 'Looped Ends versus Open Ends Braided Stent: A Comparison of the Mechanical Behaviour using Analytical and Numerical Methods'.

C. Shanahan, P. Tiernan, S.A.M. Tofail, 'Experimentally Validated Finite Element Modelling of Viscoelastic and Superelastic-plastic Nitinol for Stent Application'.

Conference Presentations

C. Shanahan, S.A.M. Tofail, P. Tiernan, 'Experimental and Abaqus FE Analysis of the Crimping Behaviour of a Viscoelastic Polymeric Braided Stent', 33rd International Manufacturing Conference, 31st August - 1st September, 2016, Limerick, Ireland – Highly Commended Paper.

Poster Presentations

C. Shanahan, S.A.M. Tofail, P. Tiernan, 'Experimental Investigation of Biodegradable Polymer Polydioxanone PDO', NUIG-UL Postgraduate Research Day, 29th April 2016, Limerick, Ireland.

Abbreviations and Symbols

2D	Two-Dimensional
3D	Three-Dimensional
B31	2-node linear beam element in space (Abaqus)
B32	3-node quadratic beam element in space (Abaqus)
BMS	Bare Metal Stent
BX	Balloon Expandable Stent
C3D8R	8-node brick reduced integration element (Abaqus)
CAD	Computer Aided Design
Co-Cr	Cobalt-Chromium
CONN3D2	A 3D, 2-node connector element (Abaqus)
DES	Drug Eluting Stent
DMF	Design for Manufacturability
FDA	Food and Drug Administration
FE	Finite Element
FEA	Finite Element Analysis
FEM	Finite Element Method
M_s	Martensite start transformation temperature
M_f	Martensite finish transformation temperature
A_s	Austenite start transformation temperature
A_f	Austenite finish transformation temperature
MIS	Minimally Invasive Surgery
PDO	Polydioxanone
PLA	Polylactic Acid
PLLA	Poly-L-Lactic Acid
PVD	Peripheral vascular disease
NiTi	Nitinol
SEE	Superelastic Effect
SFM3D4R	4-node quadrilateral surface element with reduced integration (Abaqus)
SMA	Shape Memory Alloy
SME	Shape Memory Effect
SMP	Shape Memory Polymer

SX	Self-expanding stent
TTR	Transformation temperature range
a	Crimping machine constant
C	Cover factor
C1, C2, C3	Constants referring to braided stent geometry
d	Wire diameter
d_l	Longitudinal diagonal of the diamond cell
d_t	Transversal diagonal of the diamond cell
(D_0) D	(Initial) average diameter
(D_{e0}) D_e	(Initial) external diameter
D_{head}	Diameter of the crimping head
D_i	Internal diameter
D_j	Jammed diameter
D(t)	Tensile creep compliance
D_{el}	Fourth-order elasticity tensor
$\Delta D(t)$	Transient creep compliance
(E_0) E	(Instantaneous) Elastic modulus
E_A	Austenite elastic modulus
E_M	Martensite elastic modulus
E(t)	Tensile stress relaxation modulus time dependent
$\Delta E(t)$	Transient relaxation modulus
EI	Flexural rigidity
F	Axial load
F’	Axial force acting on one helical spring
F_{load}	Force measured at the load cell
FF	Friction force inside the crimping head
g(t)	Normalised shear relaxation modulus
g_i	Shear relaxation modulus at term i of the series
G	Shear modulus
G_0	Instantaneous shear modulus
G(t)	Time dependent shear relaxation modulus
G_∞	Long-term shear relaxation modulus
GI_p	Torsional rigidity
I	Second moment

I_P	Second polar moment
J(t)	shear creep compliance
(k_0) k	(Initial) curvature of the helical spring
K_1, K_2, K_3	Jedwab's constants referring to braided stent geometry
K_L	Longitudinal stiffness
K_p	Radial pressure stiffness
l	Length of the side of the diamond cell
(L_0) L	(Initial) Braided stent length
L_{helix}	Length of wire in a helix
L_{lever}	Length of lever arm of the crimping machine
L_w	Total wire length in the braided stent
m_b	Bending moment
m_t	Twisting moment
M'	Moment acting on one helical spring
n	Number of wires
N	Number of terms in the series
N_i	Total number of intersections on the stent's surface
N_{iL}	Number of intersections on the length of stent
N_{iT}	Number of intersections on the stent's circumference
N_A	Numbers of annealing steps
N_{S1}	Step number for the annealing step
N_P	Number of pairs of plastic points
P	Radial pressure
(p_0) p	(Initial) Helical pitch
(r_0) r	(Initial) Radius of the helix
RF	Radial force
s	A later time after the initial load when a second load is applied
t	Time
t_h	Number of turns in a helix
T_0	Reference Temperature
T_g	Glass transition temperature
T_m	Melting temperature
(α_0) α	(Initial) Braiding angle

α_j	Jamming angle
$(\beta_0)\ \beta$	(Initial) Pitch angle
γ	Time variable
δ	Axial elongation
ε	Strain
$\varepsilon(t)$	Time dependent strain
ε_{el}	Elastic component of the strain
ε^{L}	Transformation strain
ε_{pl}	Plastic component of the strain
ε_{tr}	Strain due to phase transformation
ε_{V}^{L}	Volumetric transformation strain
$\dot{\varepsilon}$	Time derivative of the strain
$d\varepsilon$	Strain derivative
dt	Time derivative
$d\gamma$	Time derivative
η	Material's viscosity
$(\kappa_0)\ \kappa$	(Initial) Twist of the helical spring
ν	Poisson's Ratio
ν_A	Austenite Poisson's Ratio
ν_M	Martensite Poisson's Ratio
σ	Bending stress
$\sigma(t)$	Time dependent stress
σ_{cL}^{S}	Start of transformation loading (compression)
σ_d	Stress in a Newtonian dashpot
σ_e	Equivalent stress (Mises)
σ_s	Stress in Hookean spring
σ_{tL}^{S}	Start of transformation loading
σ_{tL}^{E}	End of transformation loading
σ_{tU}^{S}	Start of transformation unloading
σ_{tU}^{E}	End of transformation unloading
$\sigma_1^P, \varepsilon_1$	Stress-strain for point #1

$\sigma_2^P, \varepsilon_2$	Stress-strain for point #2
$\sigma_3^P, \varepsilon_3$	Stress-strain for point #3
$\sigma_4^P, \varepsilon_4$	Stress-strain for point #4
$(\delta\sigma/\delta T)_L$	Stress-temperature gradient on the loading step
$(\delta\sigma/\delta T)_U$	Stress-temperature gradient on the unloading step
τ	Shear stress
$\tau(t)$	Time dependent shear stress
$\dot{\tau}(s)$	Time derivative of the shear stress
τ_e	Equivalent shear stress (Tresca)
(Υ_0) Υ	(Initial) Shear strain
$\dot{\psi}(s)$	Time derivative of the shear strain
ψ_i	Relaxation time at term i of the series

Chapter 1
Introduction

Stent crimping is the controlled radial constraining of a stent to a diameter that allows it to be inserted into a delivery catheter prior to deployment. The stenting procedure is performed through Minimally Invasive Surgery (MIS), a technique which enables the surgeon to manoeuvre implantable devices to the target area through keyhole incisions as opposed to traditional invasive 'open' surgery. The procedure leaves smaller scars and the risk of infections is minimised. For these reasons, the hospital stay and rehabilitation for patients are considerably reduced. These advantages make MIS, the preferred technique in many cases of treatment of luminal obstructions. However, the procedure has still some disadvantages: it requires training and experimentation in relation to accurate positioning of the device in the target area, while the implantable device requires providing adequate short-term and long-term functionality. Some of these disadvantages could be overcome by a close collaboration between surgeons and design engineers. Advanced computational modelling could potentially help improve the efficacy of the technique.

Stents are most commonly used in the treatment of arteriosclerosis, a disease which narrows and blocks the blood vessels. When covered by a membrane, stent grafts are efficiently used in the treatment of aneurysms. Stents are also used in the treatment of patients with benign and malignant gastrointestinal tract strictures. Due to their great applicability, a large variety of stent designs exist on the market, employing

different types of materials, different geometries and deployment mechanisms. Even though the supply is vast, there are still some limitations in terms of their functionality such as: restenosis and stent migration where restenosis refers to the reoccurrence of the occlusion inside the lumen and stent migration refers to repositioning of the stent outside the target diseased area. The cause of these limitations may be attributed to inadequate radial forces imparted onto the inner wall of the vessel; therefore an assessment of the radial forces is hugely important prior to introducing a new design on the market. The magnitude of these radial forces can be determined experimentally. An accurate Finite Element (FE) model could also be used to reliably predict these forces.

In this thesis, a linear viscoelastic constitutive material model was developed and calibrated experimentally. The material model was validated by comparing strain predictions with experimental creep test data. Two viscoelastic materials were used in fabricating the prototypes used in the crimping experiments: Polydioxanone (PDO), a biodegradable polymer and Nitinol, a Nickel Titanium shape memory alloy. Finally, the FE models of a self-expanding braided stent used in a crimping simulation were validated experimentally.

The present chapter sets the scene and introduces the research questions, hypotheses and the methodological approach. The gap in the research literature is highlighted and the organisation of the thesis is discussed.

1.1 Background

Self-expanding braided stents are wire-based biomedical structures in tubular form manufactured using textile technologies. Stents are used to restore the opening or patency of an occluded blood vessel, an airway or various regions of the gastrointestinal tract. The deployment of these stents has become a popular method for the management of vascular and non-vascular stenosis, an abnormal narrowing of tubular organs.

Currently, the “ideal stent” that would recover lumen patency and have no biological adverse reaction has not been developed yet, despite the explosion in the stent design witnessed since its first successful introduction (Schatz 1989; Kozarek *et al.* 2013).

New stent designs that are entering the market claim superior functionality over the previous generations and one way to demonstrate their superior function is by making use of the Finite Element Analysis (FEA) and simulate their mechanical behaviour as close as possible to the in-vivo loading conditions. Prior to marketing a new stent, manufacturers need to demonstrate that they have considered the risks of device failure and have taken the necessary precautions against such an adverse outcome. The regulatory bodies recommend extensive testing to be conducted on the stent material and complete devices in order to assess the fatigue behaviour of the material platform and the durability of the stent (Pelton *et al.* 2008). They require every device manufacturer to provide evidence that they have considered all aspects of patient safety, not just the efficacy of a design when applying to place a new product on the market. Furthermore, device manufacturers must demonstrate by objective evidence that they have managed all identified patient risks, either by elimination of the risk or minimising the risk to the greatest possible extent. The gathering of this evidence through extensive testing accounts for a large proportion of development resources. In-vivo studies on stents involve testing performed on animals, as opposed to in-vitro testing which takes place in a laboratory environment. In-vivo testing is generally preferred over the in-vitro testing because it would take into consideration the overall effect an experiment would have upon the tested subject. However, in-vivo testing brings inherent risks for the test subject. When performed on animals, it requires personnel experienced in animal handling and there are concerns raised regarding animal-welfare. On the other hand, in-vitro tests do not require special protocols and approvals. Efforts have been made by the regulatory bodies to develop standards for assessing durability of cardiovascular stents. However, no standardised tests have been developed to assess stent performance, even though in recent years, testing equipment specialised in stent mechanical testing has been developed by some companies (Kemp and Ritchey 2011). Therefore, stent manufacturers develop custom made rigs and procedures in order to assess stent performance. The development process requires in vitro-testing of multiple prototypes to arrive at a stent design that is superior in comparison to its predecessor. Complex technical challenges need to be overcome for creating anatomically accurate testing environments equipped with specialist sensors, all of which holding back the pace of development and resulting in sub-optimal functionality.

Due to the high costs associated with in-vivo testing and the difficulty in implementing consistent in-vitro mechanical tests, in recent years, a number of FE studies have been carried out with the goal of evaluating current designs, understanding their mechanical behaviour and ultimately to optimise their performance. The FE method shows a compelling potential to become a powerful research tool in the analysis of stent design. This leads to the need of an accurate FE model required to reliably predict mechanical behaviour of stents, a FE model which must be built around a validated material model. While some models have been built for metallic balloon-expandable stents and for metallic self-expanding braided stents, models for the viscoelastic polymeric stents, are yet to be developed.

The current research aims to develop validated viscoelastic material models to be used in the crimping simulations development for self-expanding polymeric and Nitinol braided stents. Crimping consists in the reduction of the stent diameter to allow its insertion into a delivery catheter. Crimping enables the stent to be deployed by minimally invasive medical procedures. Minimally invasive stent delivery is de-facto standard for delivery in 21st century medicine.

An accurate FE model is required to reliably predict mechanical behaviour of braided stents when subjected to crimping. Commercial FE software packages e.g. Adina, Ansys, Abaqus, Comsol, Nastran have been employed in stent FEA and in most cases, due to its complexity, a geometrical model is created in advance on 3D CAD software, such as SolidWorks. Popular between researchers in the academia due to the wide material modelling capability, Abaqus was used in this project because it enables the implementation of time-domain viscoelasticity by deriving the creep compliance function and stress relaxation function directly from experimental data. The linear viscoelastic constitutive material model for the polymer was validated by comparing strain predictions with experimental creep test data on a monofilament sample. The Nitinol material model was calibrated using tensile and creep test data available in the literature. The 3D geometrical model of the self-expanding braided stent was created using pyFormex. Finally, the FE models of the stent were used in the crimping simulation and were validated experimentally.

1.2 Research Objectives

1.2.1 Research Questions

The following research questions are investigated in the current study:

1. How can a realistic crimping process for a braided stent be simulated using a commercial FEA software package?
2. What is the effect of implementing viscoelasticity to the accuracy of the radial forces predictions during the crimping/uncrimping process of the braided stent?

1.2.2 Research Hypotheses

The following hypotheses were constructed to find answers to the above research questions:

Hypothesis 1: The crimping process of a viscoelastic braided stent can be realistically modelled using a commercial finite element analysis software.

Hypothesis 2: The linear viscoelastic material model developed for a PDO braided stent shows an improvement in the accuracy of the stent's crimping behaviour in comparison to a purely elastic material model.

Hypothesis 3: The linear viscoelastic material model developed for a Nitinol braided stent shows an improvement in the accuracy of the stent's crimping behaviour in comparison to a superelastic-plastic material model.

1.3 Methodological Approach

From the onset of the programme, it was evident that the required work needed to be conducted in three main areas: analytical, prototyping and experimentation and FEA.

Firstly, an analytical model was created upon the work of Jedwab and Clerc (1993). The model is based on Wahl's theory of mechanical springs and the braiding angle was used as the reference parameter for the braid geometry. The model was used to predict elements of the braid geometry following an axial loading and also some mechanical properties such as braid stiffness and equivalent stress.

The prototyping stage consisted on fabricating the braided structures. Stent prototypes were manually braided in-house using the PDO suture monofilament with diameter of 0.62mm. The prototypes were fabricated from a single piece of filament in a diamond pattern (one over, one under). They were braided on a cylindrical mandrel in a seamless design, which enables crown forming at the extremities of the stent. The stents were heat set for 10 minutes at 50 °C. Stent prototypes were also braided from medical grade Nitinol wire with a diameter of 0.32 mm. The metallic stents were fabricated under the same specification as the polymeric ones and their shape was heat set for 10 minutes at 450 °C.

The materials were subjected to a series of material characterisation experimental tests. The polymeric material was subjected to a uniaxial tensile test and a uniaxial creep tensile test, in order to capture its mechanical properties. The Nitinol wire was subjected to a uniaxial tensile test to assess its superelastic behaviour. A thermal analysis (Discrete Scanning Calorimetry) was also performed on the Nitinol wire, to identify the transformation temperatures of the material. Radial forces were acquired following a series of crimping tests performed on the polymeric and metallic prototypes. The experimental setup for measuring the stent's radial force consisted of a compression device RCM-H60 manufactured by MPT Europe connected to a Zwick Single Column uniaxial tensile testing machine. During this experiment, radial forces required to reduce the diameter of the stent from the initial diameter of 22 mm to a specified diameter were recorded, as well as radial forces that stent exhibited during the uncrimping step.

The FE models for assessing the behaviour of PDO and Nitinol braided stents during crimping were developed using a commercial FE software package (Figure 1-1). Several material models were created and calibrated for PDO and Nitinol: an elastic and a viscoelastic model for PDO; a viscoelastic and a superelastic-plastic model for Nitinol. pyFormex was used as the platform for creating the 3D geometry of the braided stent. pyFormex offers a script-based approach to the 3D structure development allowing for parameterisation of the model. It offers a great advantage in comparison to the traditional CAD development, because variations of the original design can quickly be developed.

Finally, the FE models of the stent were used in the crimping simulation and were validated experimentally.

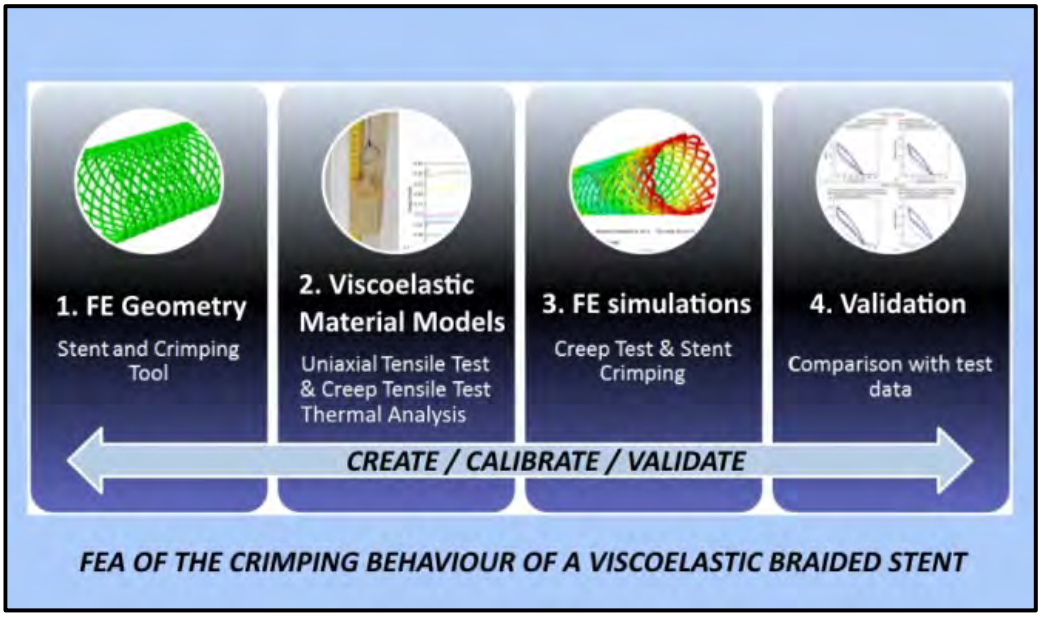

Figure 1-1: Methodology followed during the numerical study: FEA of the crimping behaviour of a self-expanded braided stent.

1.4 Gap in the Literature

Vascular stents are permanent implants. In time, the device becomes embedded inside the lumen due to tissue ingrowth. Surgical intervention is the only method of removal. On the other hand, partially-covered and fully-covered non-vascular stents can be removed endoscopically. The membrane that covers the stent prevents tissue ingrowth and with the help of special add-on design features such as a drawstring at the end of the stent that facilitates the capture and collapse of the stent, these stents can be extracted (Kozarek *et al.* 2013). However, covered stents are prone to migration, which leads to various complications such as bowel obstruction, fistulas and intestinal perforation. The partially covered ones can still embed into the wall in the areas which are not covered. To eliminate the need for a surgical procedure when the stent is needed only temporarily and also to overcome some drawbacks of bare-metal stents such as late stent thrombosis, several medical devices companies have developed biodegradable stents. Some materials used for this purpose are magnesium alloys and biodegradable polymers such as Polydioxanone (PDO), Polylactic acid (PLA) and Poly-L-lactic acid (PLLA) (Wang *et al.* 2014).

Radial stiffness is one of the most important mechanical characteristics of stents (Duerig and Pelton 2002; Stoeckel *et al.* 2002). The Finite Element (FE) method can help quantifying the forces that the stent imparts to the catheter or lumen. The FE model would need to be equipped with a validated material model in order to ensure accuracy of the radial forces predictions. Finite Element Analysis (FEA) helps lowering of development costs, facilitates stent design optimisation and ultimately reduces the time-to-market by shortening the product development cycle. However, despite the advantages in using FEA in stent design, research literature dedicated to self-expanding braided stents is limited and mainly focused on metallic stents, while FE models for the polymeric braided stents are almost non-existent. The FE models developed for materials such as stainless steel and Phynox (De Beule 2008) are the generic linear elastic type, while the ones developed for Nitinol are user defined models covering its superelastic behaviour (De Beule *et al.* 2007; Kim *et al.* 2008; Ma *et al.* 2012; Zhao *et al.* 2013; Frost *et al.* 2014). The only FEA of polymeric braided stents was performed by Peirlinck (2013). Using Abaqus/Explicit, Peirlinck created a linear elastic material model for the polymer and a numerical framework to simulate the deployment and expansion of a braided stent was developed. Nitinol and PDO, however, exhibit viscoelasticity. Both materials store part of the energy due to deformation, and dissipate the rest of the energy; therefore the loading and unloading steps do not follow the same paths.

The lack of scientific efforts in the area of self-expanding braided stents may also be due to the complexity of the geometrical model and the subsequent numerical analysis. Usually, FEA software packages offer functionality that enables creating 3D geometry, however, the braided stent 3D model is highly complex and the common development method is to use a powerful solid modelling CAD software package like SolidWorks. A different avenue to developing the geometry was introduced by De Beule *et al.* (2007) and consists in using pyFormex and then importing it into Abaqus. pyFormex, an open-source tool for advanced geometrical modelling developed in Gent University, Belgium (Verhegghe 2013) is capable of creating large sets of coordinates based on mathematical transformations gathered inside a Python script.

The objective of this thesis is to evaluate the time-dependent viscoelastic response of a braided stent subjected to crimping through the use of experimental and numerical methods. To the best of the author's knowledge, a viscoelastic material model has never been implemented in a FE model of a braided stent. The current research presents the steps required in developing the linear viscoelastic material models for a polymeric and a Nitinol stent, from acquiring test data to Abaqus implementation and calibration. FE models for the braided stent were created making use of these viscoelastic material models. Finally, the FE models were validated by performing the numerical simulation of stent radial compression and comparing the predictions of the radial forces of the braided stent with the experimental test data.

1.5 Scope of the Thesis

This thesis is organised into eight Chapters and accompanying appendices.

'Chapter 1 Introduction' introduces the background and objectives of the current research. The research questions are discussed together with the hypotheses and then the methodology is described. The final section of the chapter presents the contribution to the current state of art and outlines the structure of the thesis.

Understanding the existing knowledge is essential; therefore, '**Chapter 2 Literature Review'** consists of a classification of stents based on design and engineering characteristics. Stent design criteria are described, followed by an account of typical materials, form and platform geometry. Fabrication techniques such as braiding and knitting are presented as well as an introduction to polymer and Nitinol viscoelastic behaviour. Several constitutive equations for one-dimensional response of viscoelastic materials are presented. The chapter concludes with a review of the progress made by researchers in the area of braided stent FE modelling.

'Chapter 3 SX Braided Stents' presents an analytical study that commences with a description of the geometrical parameters of a braided stent. The stent is subjected to axial loading and the calculation of the elongation and of some mechanical properties is presented. The axial force, axial and radial stiffness, the equivalent stress are calculated in terms of braid angle. A description of prototype fabrication concludes

the chapter. Stent prototypes were manually braided in-house using the PDO suture monofilament and medical grade Nitinol wire.

In '**Chapter 4 Experimental Techniques'**, mechanical tests performed in order to determine the mechanical properties of the PDO suture material: uniaxial tensile test and tensile creep test are presented in detail. The short-term uniaxial tensile test is required to determine the instantaneous elastic modulus of polymer, while the creep test is used to determine its viscoelastic, long-term behaviour. To characterise the microstructure of the Nitinol wire, a thermal analysis is performed. The wire is also subjected to a uniaxial tensile test. The crimping experiment is performed on braided stent prototypes fabricated in house. A detailed description of the stent crimping experiment and the technique used to capture raw data required for the calculation of radial force is given. The chapter concludes with the outcome of the experiments.

'Chapter 5 Finite Element Analysis' includes the method of creating the 3D model for the braided stent using pyFormex. In order to perform the crimping process, three different types of crimping tools are designed and the creation of their geometrical models is presented in this chapter. Abaqus ver. 6.14 was chosen to perform the FEA and for this reason, the constitutive equations that Abaqus uses in modelling the linear viscoelasticity of a material are highlighted. The bases of the crimping simulation strategy are also described.

'Chapter 6 Looped ends versus Open ends' investigates whether the analytical model for assessing the mechanical behaviour of an open ends metallic braided stent described in Chapter 3 is applicable to the looped ends stent design. The response of the two stent designs subjected to radial compression in terms of radial forces and equivalent stresses is also presented.

'Chapter 7 Viscoelastic PDO Braided Stent' presents the development of the PDO FE model and the stent crimping simulation. The linear viscoelastic constitutive material model for PDO is developed and calibrated. The FE model is validated by performing the simulation of stent radial compression and comparing the radial force predictions with the experimental data.

In **'Chapter 8 Viscoelastic Nitinol Braided Stent'**, two Nitinol material models - a viscoelastic and a superelastic-plastic material model are developed and compared

for their effectiveness in capturing its complex behaviour during stent loading and unloading. The FE models are validated against the radial compression test data.

‘Chapter 9 Conclusions’ summarises the results. Final conclusions are drawn from the results and recommendations for future work are presented. The contributions of the work and significance of the research are highlighted.

‘Chapter 10 References’ lists all the references in this study in alphabetical order.

Chapter 2
Literature Review

The aim of this chapter is to provide an overview on finite element modelling of self-expanding braided stents. The chapter commences with a classification of stents based on design and engineering characteristics. Stent design criteria are described, followed by an account of typical materials, form and platform geometry. Stent fabrication techniques such as laser machining, braiding and knitting are presented, laser fabrication technology being the preferred technique for tube based stents (Bonsignore 2003). The focus of this work is on viscoelastic braided stents therefore, a brief introduction to polymers and Nitinol is presented and their viscoelastic response is discussed. Several constitutive equations for one-dimensional response of viscoelastic materials are presented. This introduction is followed by a survey regarding state of the art solid mechanical computational models of self-expanded braided stents. The review is organised chronologically and presents the efforts made so far towards building validated models capable of predicting the complex mechanical behaviour of this type of stents. The method of creating the 3D geometry is highlighted, material characterisation and types of simulations performed.

2.1 Stenting Technology

Stents are biomedical structures in tubular form used to restore the opening or patency of an occluded blood vessel, an airway or various regions of the gastrointestinal tract.

2.1.1 Background

The term *stent* was introduced in the medical literature in 1916 by Jan F. Esser, a Dutch plastic surgeon. Esser used a dental impression compound as scaffolding for tissue when performing facial reconstruction (Ring 2001). This compound was invented in 1856 by the British dentist Charles T. Stent (1807-1885), and the term stent derives from his name.

In 1912, Nobel laureate Alexis Carrel, described experiments where glass and metal tubes covered in paraffin were implanted in canine aortae in order to recover the lumen of diseased vessels. Charles Theodore Dotter reintroduced the concept in 1964 and developed several plastic and metallic designs (Dotter and Judkins 1964). In early 1980s, he developed a prosthesis made out of shape-memory alloy Nitinol and implanted it into canine peripheral vessels (Dotter *et al.* 1983; Schatz 1989). The term as known in the medical field today, was used with the advent of Wallstent, a flexible self-expanding prosthesis co-invented by Hans I. Wallsten in the 1980's (Rousseau *et al.* 1987; Wallsten 1987; Wallsten and Imbert 1991).

Stents are used in cardiovascular, pulmonary and gastrointestinal systems of the body, and refer to implantable medical devices that provide support or scaffolding to the wall of a tubular structure, such as an artery, airway or intestine.

Benefits

Contemporary trends in surgical procedures are towards minimally invasive techniques where the incision size is limited, as opposed to traditional invasive 'open' surgery. Minimally invasive surgery involves the use of a laparoscopic device and remote-control manipulation of instruments. The surgical field is observed indirectly through an endoscope or a magnifying display, and the procedure is carried out through the skin or through an anatomical opening. The procedure results in fewer infections, a quick recovery time and less hospital stay for the patients due to the minimal damage of biological tissue at point of entrance of the surgical instruments.

“Stenting” means the intraluminal placement of a stent and it is an example of such a minimally invasive procedure. There is a lower risk of complications than in the traditional procedure; the recovery time is much shorter, people being able to return to their normal activities quickly. In addition, with most patients, the procedure does not require general anaesthesia.

Risks

Major complications related to MIS are not common, but a risk of heart attack, stroke, infection and sudden cardiac death would always exist, even though at a lower rate than in the open surgery procedure. Another complication is the possibility of recurrence of the narrowing in the vessel, or *restenosis*. This would occur because the artery or passageway may perceive the stent as a foreign body and respond by a proliferation of cells (neointimal hyperplasia) in the affected area in order to protect against it. In these cases, patients may require another intervention, a restenting procedure, or bypass surgery to correct the problem.

On rare occasions, a condition known as stent thrombosis would follow stent implantation due to tissue trauma of the vessel or passageway (Honda and Fitzgerald 2003). Stent thrombosis is a blood clot which can cause blockage of an artery and may lead to heart attack or death. Another risk associated with this type of device is the risk that the stent might migrate from the site of implantation region down the arterial lumen.

2.1.2 Stent Types by Release Mechanism

Stent deployment mechanisms required to transport the stent to the desired deployment site use special tubular instruments called delivery catheters. Depending on the release method by which the stent is expanded to the lumen diameter, stents can be classified in two categories: Balloon eXpandable (BX) and Self eXpanding (SX).

BX stents (Figure 2-1)

The BX stent can be either pre-mounted on a balloon catheter or crimped onto the balloon by the physician at time of procedure. The stent is mounted onto the tip of the balloon catheter in a crimped state and after deployment in the affected area it is

expanded to the required diameter by inflating the balloon inside the stent. The procedure is finished with removing the deflated balloon and the catheter. BX stents are predominantly used in vascular interventions.

SX stents (Figure 2-2)

SX stents are mainly used in peripheral vascular lesions and non-vascular applications and in recent years have also been used in coronary arteries (Wijns and Pyxaras 2012). The SX stent is constructed at the relaxed dimensions and subsequently crimped in order to fit into the catheter for deployment. Once the covering sheath is removed, the SX stent expands at the diameter of the diseased lumen, the radial force pushing the inner wall and restoring the luminal patency.

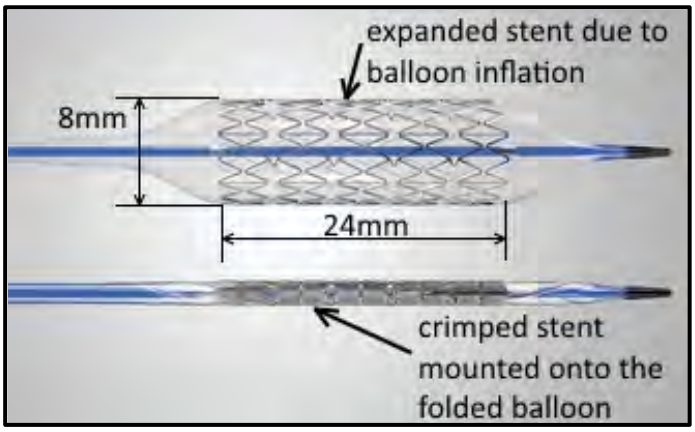

Figure 2-1: Formula Biliary BX stent (Cook Medical 2013a). This BX stent is used for palliation of malignant neoplasms in the biliary tree.

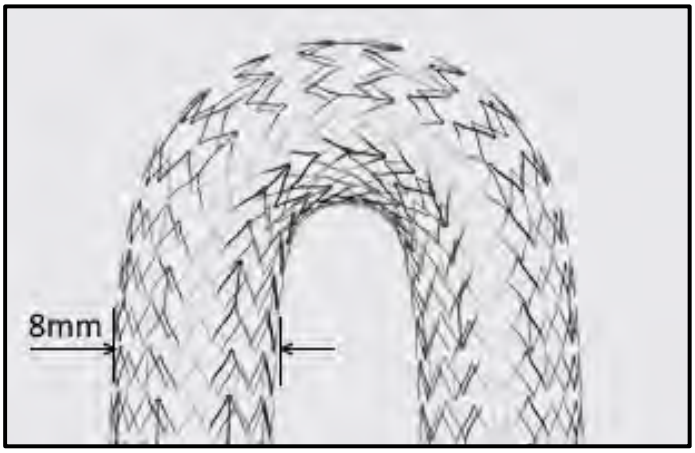

Figure 2-2: Zilver SX stent (Cook Medical 2013b). This SX stent is used in the palliation of malignant neoplasms of the biliary tree.

Duerig and Pelton (2002), Duerig and Wholey (2002) summarised the key differences between the two types of stents relative to their clinical performance. The key mechanical features analysed were: radial strength, radial and axial stiffness, recoil, accuracy of deployment, visibility and fatigue. Their conclusion was that no stent can be considered universally superior to be recommended in any clinical situation, but rather certain types would be more appropriate in specific circumstances.

2.1.3 Stent Types by Clinical Application

From the point of view of their clinical use, stents can be grouped in vascular and nonvascular types:

- *Vascular stenting technologies* refer mainly to stenting procedures for treatment of coronary artery disease (Figure 2-3), carotid artery disease (Figure 2-4) and peripheral vascular disease (Figure 2-5). Vascular stents are used for treating narrowed or blocked passages in the vascular system, with the ultimate goal of improving the blood flow. The stenosis or narrowing of the blood vessels occurs in patients suffering from a disease called atherosclerosis.

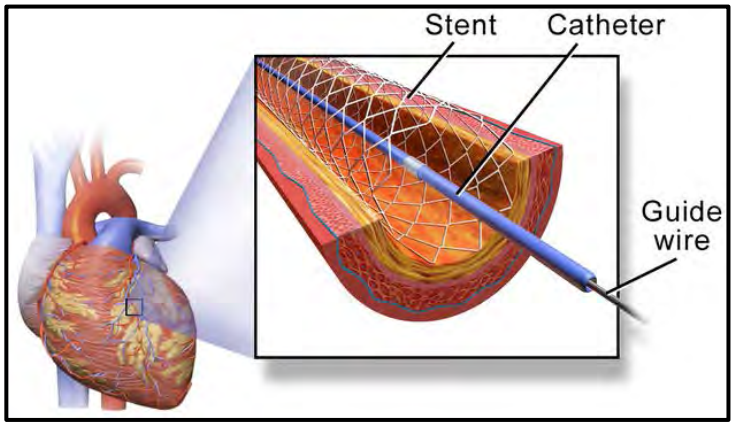

Figure 2-3: Coronary artery application: angioplasty stent (Blausen.com Staff 2014). This stent is placed in the coronary arteries that supply blood to the heart, to keep the arteries open in the treatment of coronary heart disease. The diagram shows the stent expanded inside the artery prior to the removal of the catheter and guide wire.

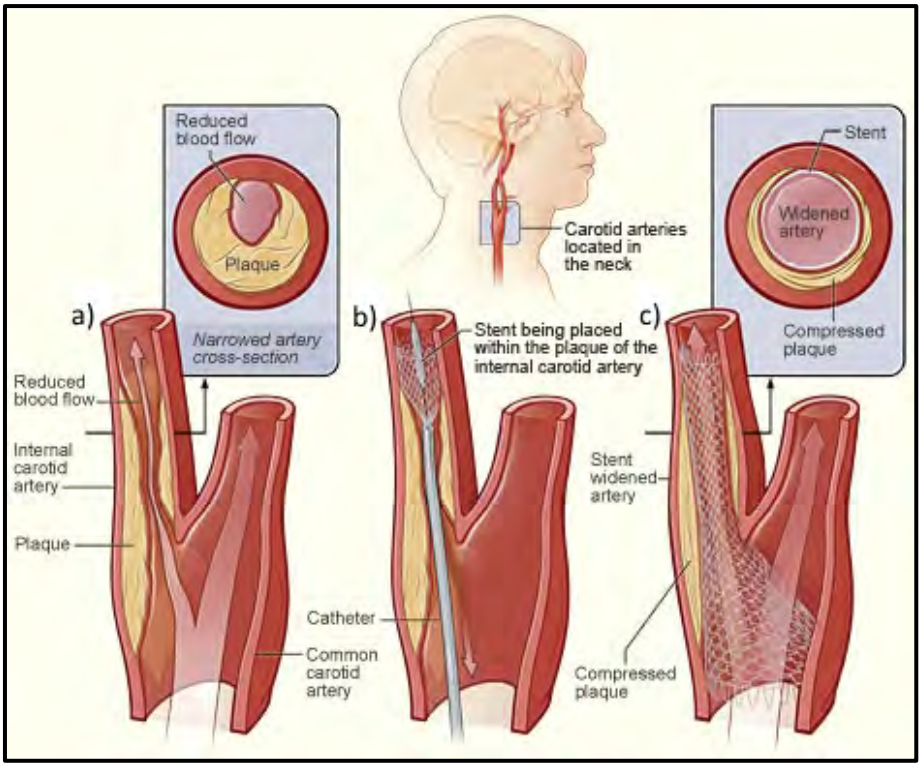

Figure 2-4: Carotid artery stenting (US Department of Health & Human Services National Heart Lung and Blood Institute 2013). The illustration shows the critical steps in the procedure. a) Gaining vascular access b) Crossing the stenosis with a wire c) Deploying the stent across the lesion and restoring the blood flow.

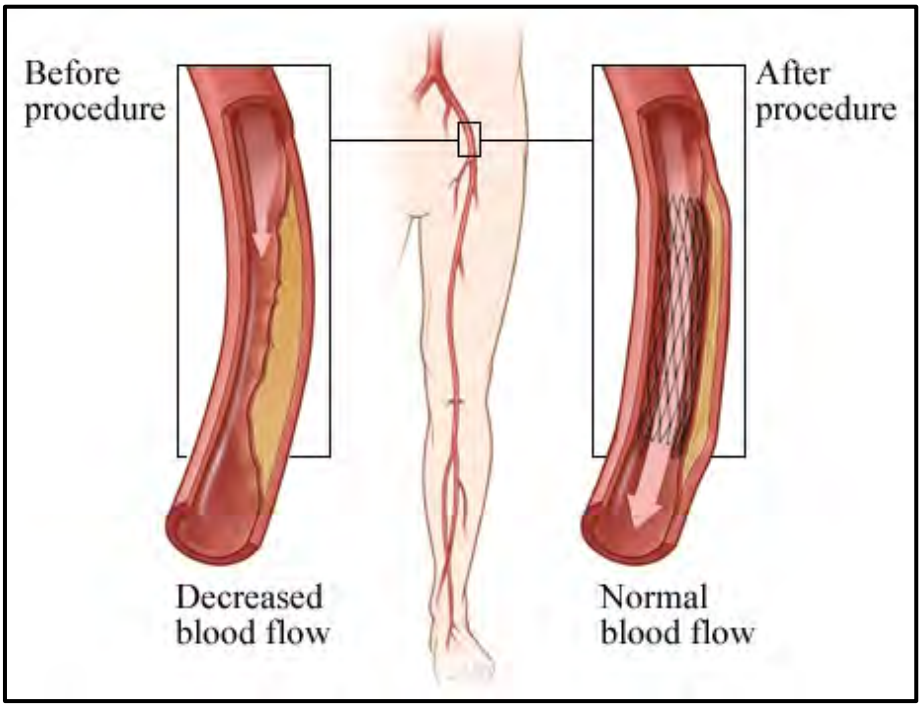

Figure 2-5: Peripheral vascular stenting (Healthwise Inc. 2016). The illustration shows the diseased artery with a decreased blood flow before the procedure and after the blood flow is restored.

- *Nonvascular stenting technologies* are used in the palliative care of obstructions occurring on circulatory passageways which enable transfer of air, food and bodily substances. These circulatory pathways include the airways, the gastrointestinal tract (GI), the biliary tree, and the urinary tract. Stents are used in treatment of both benign and malignant conditions.

Silicone and metallic ***airway stents*** (Figure 2-6) are being used successfully in both benign and malignant cases of airway obstruction caused by external compression, intraluminal disease, or loss of cartilaginous support (Simonds *et al.* 1989; Wilson *et al.* 1996; Wood 2001).

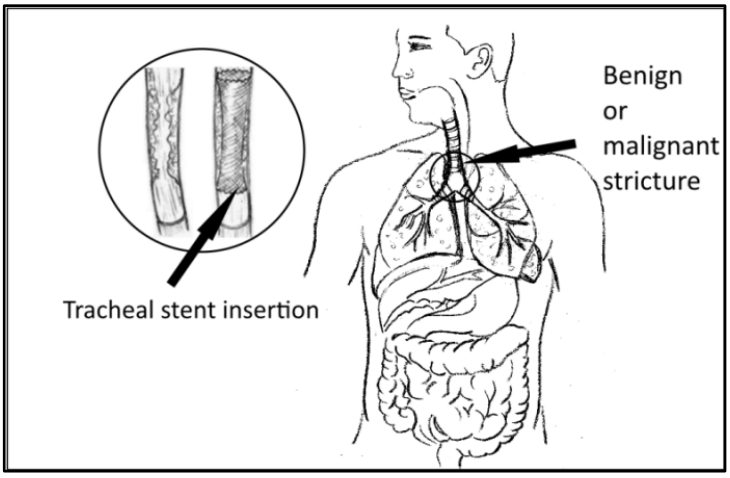

Figure 2-6: Tracheal stent insertion. The illustration shows the tracheal stent insertion inside the section of the trachea where the stenosis occurred.

Gastrointestinal stents (Figure 2-7) are used to restore the patency of various regions of the gastrointestinal tract (esophageal, duodenal, enteral, colorectal, biliary).

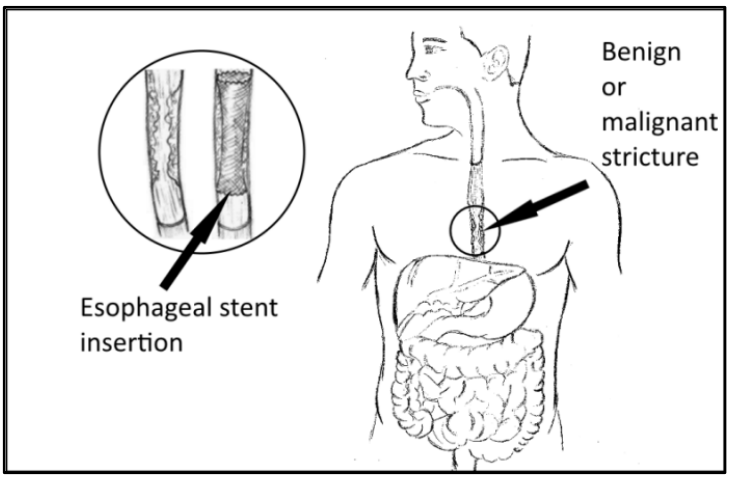

Figure 2-7: Esophageal stent insertion. The stenting procedure is used in the treatment of benign or malignant strictures.

2.2 Stent Design

2.2.1 Introduction

Stoeckel *et al.* (2002) proposed a classification of stents based on design and engineering characteristics, which are illustrated in the stent design pyramid in Figure 2-8.

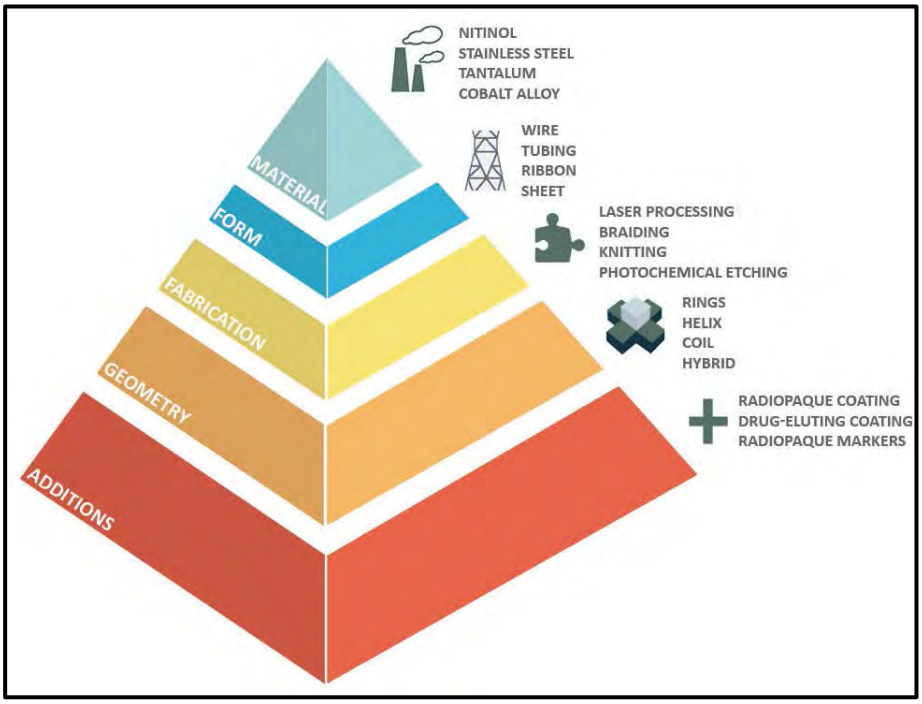

Figure 2-8: Stent design pyramid (adapted from Stoeckel *et al.* 2002) indicating the classification of stents based on raw material type and form, fabrication techniques, stent geometry and enhancements of the basic stent design.

The classification starts with materials used in stent manufacturing: Nitinol, Stainless Steel, Tantalum and Cobalt Alloys and the form they are presented in e.g. wire, tube and sheet. It continues with fabrication methods such as laser cutting and wire forming techniques; geometry characteristics such as helical mesh, open and closed cell. Finally, additions to stents are presented, such as supporting fabrics forming grafts, radiopaque markers for improving visibility during deployment of the device, coatings and linings.

2.2.2 Stent Design Criteria

The two minimally invasive surgical procedures involving stenting - endovascular stenting and endoluminal stenting, although have become preferred methods of treatment for disorders such as occlusions or ruptures of passages, have a high re-intervention rate due to long term complications. While the number of designs commercially available is continually increasing, no standard tests exist for assessing mechanical characteristics of stents. Therefore, each manufacturer would claim specific advantages to their stent designs over the stents belonging to their competitors. Stent design criteria encompass a set of requirements the device must reach in order to be considered successful. Depending on the clinical application, stents are not only designed to satisfy short term requirements such as re-canalisation of the lumen. Long term safety implications, such as major adverse events due to restenosis, incomplete vascularization and thrombosis need also to be considered and represent a major design benchmark. When grouping these ideal stent requirements, four main viewpoints can be identified: safety, performance, manufacturability and deliverability (Figure 2-9).

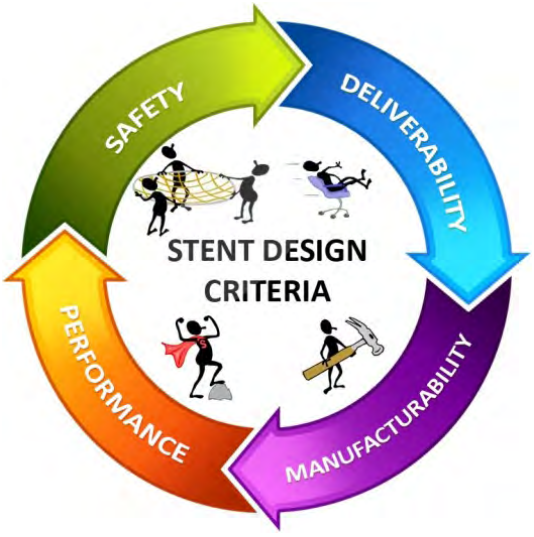

Figure 2-9: Stent design criteria presenting design requirements from four perspectives: safety, performance, manufacturability and deliverability.

This section assesses design criteria for an ideal stent from these four perspectives: safety (biocompatibility, lumen-stent interaction, fatigue, adverse events), performance (radial strength, trackability, conformability, flexibility), deliverability (ease of use, struts thickness, placement accuracy, radiopacity) and manufacturability

(ease of processing, efficiency). Whether intended for the vascular or non-vascular system, the general stent design criteria are common, with only a few minor differences that are highlighted in this review.

Safety

Biocompatibility needs to be considered from the outset of the design process. To ensure biocompatibility of a material or medical device, rigorous testing must be performed to determine the toxicity of the material, whether there are leachable substances and degradation products.

The ISO 10993 series of standards, developed to protect humans, serves as a framework for selecting the tests in order to evaluate biological responses (ISO 2009a). The most important tests related to implantable medical devices and materials are cytotoxicity (ISO 2009b) and hemocompatibility tests (ISO 2002). Cytotoxicity tests refer to cell damage caused by direct contact with the material or with leachable substances. Hemocompatibility tests are used to evaluate the effects of materials or medical devices which come in contact with blood.

Stent corrosion and fracture can cause or contribute to premature stent failure. Therefore, the 2010 FDA Guidance document covering Non-Clinical Engineering Tests for Intravascular Stents (US Department of Health & Human Services Food and Drug Administration 2010) recommends extensive fatigue life analyses to be conducted on the stent material in order to assess the fatigue behaviour of the material platform and the durability of the stent (Pelton *et al.* 2008).

Performance

The performance of a stent refers to its acute clinical outcome. In order to achieve the recanalisation of the lumen, an ideal stent should have the following mechanical properties (Poncet 2000; Lau *et al.* 2004; Lally *et al.* 2005, 2006; Schillinger *et al.* 2006; Wholey and Ender 2007; Isayama *et al.* 2015):

- Excellent radial strength to maintain lumen patency and prevent migration of the stent from the diseased region;
- Enough rigidity to withstand the compressive forces of the vessel wall and exhibit a minimum elastic recoil;

- Excellent longitudinal flexibility and conformability to the lumen host;
- Good flexibility in its crimped state to enable smooth movement through tortuous vessels and to prevent straightening of a curved vessel during expansion;
- Minimal foreshortening during expansion, to allow for accurate deployment (a minimum change in length between the crimped state and the deployed state);
- Good stent apposition and optimum scaffolding to ensure a good vessel coverage;
- Secure fixation for the duration of the treatment but also the ability to be removed in the case of the non-permanent stent placement (requirement for some non-vascular stents).

However, these are very complex properties to achieve in a single design because most of these goals compete against each other, such that an improvement of one property may result in compromising others. For example, a low radial expansion force is required to minimise the risk of restenosis. However, this force needs to be high enough to prevent stent migration. Adequate scaffolding is achieved by ensuring optimum radial resistive force. However, this force needs to be low enough to facilitate crimping and to enable access in high tortuous vessels without fracturing. This study presents the methodology required in the analysis of these radial forces.

Deliverability

The success or failure of stent implantation relies on the deliverability of the stent. Regardless of the clinical context, deliverability helps to position the stent in the targeted area. This feature becomes more important when dealing with lesions situated in tortuous and calcified segments, which are hard to reach. One of the most important features of a stent, deliverability should indicate:

- A minimal delivery system enabled by a low strut thickness;
- Ease of use;
- Good trackability, representing the ability of the delivery system to follow a tortuous path during deployment to the target area;

- High visibility on fluoroscopy achieved by using radiopaque markers made from materials with higher atomic weight (e.g. tantalum, gold, platinum).

Manufacturability

Stent design for manufacturability (DMF) means designing from the perspective of material type and form, tolerances and design platform geometry. Each fabrication technique has strengths and limitations, therefore having a good understanding of these characteristics, enable design engineers produce higher quality and more cost competitive designs.

Material Type - *The* two main choices for material are metallic alloys and polymers. Typical alloys used as stent platform are stainless steel, cobalt alloys and Nickel-Titanium alloys. These metallic alloys must exhibit biocompatibility, high strength and an excellent corrosion and fatigue resistance. Due to their required mechanical properties, these alloys are not easily processed. In the case of Nitinol devices, for example, joining dissimilar materials is very difficult, therefore, the most common method used is crimping. Traditional machining techniques such as milling, turning and grinding can be used, however, the tools would wear very quickly. Due to these difficulties, Nitinol stents would most likely have radiopaque markers joined by crimping to the wires. Laser cutting is the most common material removal technique used in the fabrication of BX stents. Etching and electropolishing are also used mainly to clean the layer of oxide formed on the surface of the material following its fabrication. Plating is sometime performed to enhance the visibility of Nitinol devices under fluoroscopy, but it's a challenging operation due to the oxide layer which must be removed prior to plating. Coatings with silicone, polyurethanes can be applied to reduce the risk of thrombosis (Poncet 2000).

Medical grade polymers, on the other hand, are easier to process. Some of these processes are injection moulding, extrusion and thermo forming. Joining and welding can be performed in case the device has a complex shape, some examples are: ultrasonic welding and laser welding. However, the bioresorbable polymers bring new challenges which refer to handling, testing, processing and validating the bioresorbable components. An important process which must be performed in case of implantable devices is sterilization and some of the methods used are: dry heat and

radiation, however, proper parameters and process type must be chosen in order to avoid deformation, molecular weight loss and hydrolysis (McKeen 2014).

Material Form **-** Metallic alloys and polymers used in stent manufacturing come in a variety of forms such as tube, wire and plate. Some of the forming processes are wire and tube drawing, hot or cold sheet rolling.

Tolerances **-** The industry trend towards smaller micro-machined stents implies sub-micron tolerances. This requirement can be achieved due to continuous advancement in the laser-cutting technology, where automatically controlled high precision systems perform consistently and efficiently.

Simplicity **-** The trend in medical device design and manufacturing is towards miniaturisation while increasing in performance and features. This means a continuous growth in the level of sophistication of the components, manufacturing technologies and automation techniques. “The simpler, the better” does not apply, because due to the strong competition, the stent manufacturers do not focus on delivering basic functionality, but rather aim at enhancing their designs with features that would deliver a competitive advantage over competing devices.

2.2.3 Materials

As implantable medical devices, stents must exhibit excellent corrosion resistance and biocompatibility. They should also be radiopaque, (although radiolucent markers may also be used) and should create minimum interference with the MRI equipment. Biocompatibility of stents refers to their ability to perform their function without causing undesirable effects such as toxin release or harm to the lumen. Corrosion resistance refers to the ability to resist the corrosion action of bodily fluids. Stent corrosion can have a double impact, firstly because it may lead to the alteration of the mechanical properties of the stent, secondly because corrosion means the release of metallic ions in the body.

BX stents are made from materials that can be plastically deformed by balloon inflation. After the balloon is deflated and removed, the stent stays at deformed dimensions with slight recoil. Stoeckel *et al.* (2002) suggest that the ideal material

for these stents needs to have a low yield stress to allow for plastic deformation during balloon inflation and a high elastic modulus for minimal recoil.

SX stents are deployed constrained in the catheter and expand at predefined diameter when the sheath is withdrawn. According to Stoeckel *et al.* (2002), the material should have a low elastic modulus and a high yield stress, i.e. a flexible material that can easily change its shape, difficult to break and to facilitate large elastic deformation. A selection of the current stent designs is presented in Table 1.

Table 1: Some of the current BX and SX stent designs with their characteristics.

MANUFACTURER	STENT	MATERIAL	DESCRIPTION
ABBOTT	Supera® Peripheral Stent System	Nitinol	SX single wire braided design; diameter 4-7mm, length 20-200mm
BOSTON SCIENTIFIC	WALLSTENT Endoprosthesis	Elgiloy	SX stent; braided wires in a tubular mesh shape; diameters 5-24mm and deployed lengths 23-145 mm; recapturable
	Epic™ SX Vascular Stent System	Nitinol	SX stent with tube cut in an open lattice design; diameter 6-12mm, length 20-120mm; MACRO™, MEDIUM and MICRO™ Strut tandem design
	ION™ Paclitaxel-Eluting Coronary Stent System	Stainless Steel	BX stent slotted tube design; a drug (paclitaxel) contained within a thin polymer coating on its surfaces
	PROMUS Element Plus Coronary Stent System	Platinum Chromium Alloy	BX stent slotted tube design; a drug (everolimus) contained within a thin polymer coating on its surfaces
	WallFlex™ Esophageal Stents	Nitinol (silicone coated)	SX Stents braided multi-wire design with flares at both ends; Fully and Partially Covered with Permalume; diameter 18-23mm and length 10-15mm
COOK MEDICAL	Evolution® Esophageal Controlled-Release Stent	Nitinol (silicone coated)	SX single wire braided design; partially and fully covered design with silicone coating; diameter

			20mm, length 80-150mm
	Zilver® Biliary SX Stent	Nitinol	SX laser-cut Nitinol tubing with an interlocking design construction and gold radiopaque markers; diameter 6-10mm, length 40-80mm
COVIDIEN	Visi-Pro™ BX Peripheral Stent System	316L Stainless Steel	BX Tube cut into an open lattice design; tantalum radiopaque markers; stent is mounted onto a 5-fold balloon catheter.
ELLA CS	SX-ELLA Stent Esophageal Degradable BD	Polydioxanone (PDO)	SX braided stent with flared ends design and radiopaque markers at both ends; stent integrity and radial force of the stent maintained for 6 – 8 weeks following implantation; completely disintegrated after 11-12 weeks
MEDTRONIC	Driver Sprint Coronary Stent System	Cobalt Alloy	BX Stent with ultrathin, round, edgeless struts for smooth delivery; modular elements joint together in proprietary laser-fusion patterns for high stent flexibility.
	Protégé™ EverFlex™ SX Biliary Stent System	Nitinol	SX stent cut from a Nitinol tube into an open lattice design; designed with tantalum radiopaque markers at the proximal and distal ends of the stent.

Metallic Stents

316L Stainless Steel is the standard material for the BX stents. The material is easily deformable in its annealed condition and exhibits the required elasticity when fully hardened. Other metals are tantalum, platinum alloys, cobalt alloys and niobium alloys. These materials have a better radiopacity and higher strength enabling designing stents with a small profile. Generally, a BX stent remains permanently inside the vessel or until it is removed through surgical intervention. To eliminate the need for a surgical procedure when stent is needed only temporarily and also to overcome some drawback such as late stent thrombosis, several medical devices

companies have developed bioabsorbable stents. The typical materials for these stents are magnesium alloys. Zinc, with its corrosion behaviour and meeting mechanical behaviour benchmark, is proposed as a new material candidate.

SX stents are mainly manufactured from Nitinol, a Nickel Titanium (NiTi) shape memory alloy. Nitinol is widely used in biomedical applications due to its special mechanical properties, good biocompatibility and corrosion resistance.

The mechanical and chemical properties of the most common metals used in stent manufacture: 316L Stainless Steel, cobalt alloys, binary and ternary Nitinol are presented next. The chemical composition and mechanical properties data sheets for these materials are depicted in Appendix 1.

316L Stainless Steel

The stainless steels are specific types of steel with an increased resistance to chemical agents. Considering their crystal microstructure, stainless steels can be classified into martensitic, austenitic and ferritic stainless steels. 316L Stainless Steel is a low-carbon molybdenum-bearing austenitic stainless steel. This alloy has a superior resistance to corrosion due to the addition of molybdenum and an increase in the nickel content, which makes it suitable to applications in severe settings. The alloy also offers higher creep, stress to rupture and tensile strength at elevated temperature when compared to other chromium-nickel austenitic stainless steels. In addition to excellent corrosion resistance and strength properties, the alloy also provides excellent formability, which is typical of the austenitic stainless steels. Typical applications include food preparation equipment, pharmaceuticals, marine applications and medical implants including stents, pins, screws and orthopaedic implants such as total hip and knee replacements.

Cobalt Alloy MP35N

Cobalt Alloy MP35N is a Nickel-Cobalt base alloy with a unique combination of properties: high strength, outstanding corrosion resistance and fatigue resistance. Medtronic Vascular (2003) have compared the physical and mechanical properties of cobalt alloy MP35N, with those of 316L Stainless Steel, in order to demonstrate its suitability for stenting applications. MP35N alloy is stronger and with a higher

density than stainless steel, which enables design and manufacture of thinner struts without compromising on the radial strength.

Cobalt Alloy ASTM F1058, marketed as Elgiloy or Phynox, is a Cobalt-Chromium-Nickel alloy. Phynox exhibits excellent biocompatibility and corrosion resistance. The alloy has good mechanical properties, high strength and good fatigue resistance (Clerc *et al.* 1997). Cobalt alloys are non-ferromagnetic because the content of iron is small which leads to improved MRI-compatibility in comparison with 316L Stainless Steel.

Nitinol (NiTi) Alloy

SX stents are mainly manufactured from Nitinol. Discovered in the 1959 by William J. Buehler and Frederick Wang during research at the Naval Ordnance Laboratory, Nitinol derives its name from its elements and its founders: Ni (Nickel) – Ti (Titanium) – NOL (Naval Ordnance Laboratory). Nitinol is a near equiatomic shape memory alloy (SMA) utilised extensively in the medical engineering world due to its amazing shape-memory effect, superelasticity, biocompatibility and fatigue resistance properties.

The shape-memory effect (SME) and superelasticity effect (SE) are unique characteristics of SMAs and are credited to their ability to exhibit martensitic transformations. Martensitic transformation is a fully reversible solid-state phase transformation between the parent phase – austenite and the daughter phase – martensite. It is a diffusionless phase transformation in solids characterised by homogeneous movement of atoms resulting in a change in the crystal structure. These movements are small, usually less than the interatomic distances and the atoms maintain their relative relationships.

Martensitic transformation can be induced thermally, in which case the shape-memory effect is exhibited. Martensitic transformation can also be induced mechanically at a temperature above the transformation temperature to austenite, in which case the superelastic property of the alloy is observed.

The shape-memory effect (SME)

The shape-memory effect consists in the material's ability to undergo deformations at a low temperature and then recover its original shape upon heating above a critical temperature. The parent phase, austenite has a cubic structure which is stable at high temperatures. The process (Austenite -> Martensite) starts by a lattice-shear distortion mechanism (Lagoudas 2008) when the temperature is lowered below a critical value. Martensite has a monoclinic structure stable at low temperatures. It has a lower symmetry than austenite, hence the transformation can lead to many types of variants characterised by the same structure but a different orientation. When the temperature is raised, martensite becomes unstable and the reverse process (Martensite -> Austenite) occurs, the crystal structure transforming into a cubic crystalline structure.

The transformation temperature is the temperature at which the phase change occurs. Four different transformation temperatures are required to describe the thermal induced phase change:

- M_s: the temperature at which the transformation from austenite to martensite starts upon cooling the material;
- M_f : the temperature at which the transformation is complete and the phase is fully martensitic;
- A_s: the temperature at which the transformation from martensite to austenite starts upon heating the material;
- A_f : the temperature at which the phase is fully austenitic.

Martensite formation starts instantaneously when the parent austenite cubic phase is cooled below the M_s temperature. By the time the temperature reaches M_f, the phase change is complete and the crystal has a less ordered, monoclinic structure. The reverse transformation into austenite starts at austenitic start temperature A_s and the process concludes when the austenitic finish temperature A_f is reached (Duerig *et al.* 1990). The process is represented in Figure 2-10. The cooling and heating cycle shows thermal hysteresis.

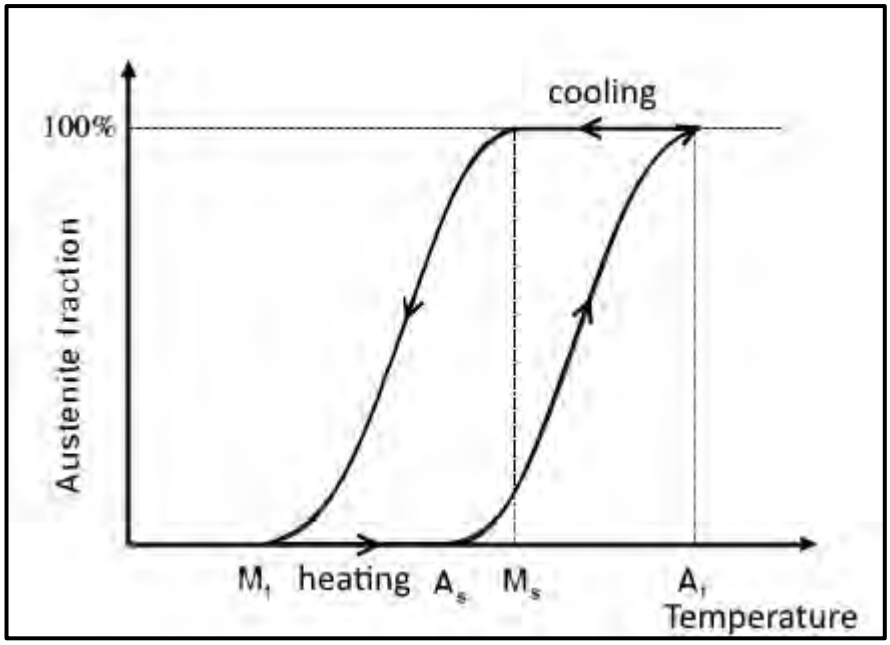

Figure 2-10: Thermal hysteresis curve for Nitinol during the heating and cooling cycle. M_s is the temperature at which thermal martensite starts to form, A_s is the temperature at which the solid phase starts reversing into austenite. M_f and A_f are the temperatures at which the phase transformations are complete.

The shape memory effect (Figure 2-11) is exhibited in case the alloy is deformed below the martensite transformation temperature. If a load is applied to the material while at this low temperature, the martensitic structure is detwinned and the process results in a macroscopic shape change, the deformed shape being retained even after the load is removed. When heated above the A_s temperature, the phase change into austenite starts and when reaching A_f temperature, the microstructure is fully reversed. The phase transformation temperatures are influenced by the percentage of nickel present within the alloy and also by adding a third element to the alloy.

Sometimes, when cooling the material below Ms, or heating above As, the phase doesn't always change directly into martensitic/austenitic structure, but into an intermediate rhombohedral phase known as the R-phase. The formation of R-phase can be attributed to chemical composition and certain thermo mechanical treatments (Miyazaki and Otsuka 1986; Bataillard *et al.* 1998). The R-phase to austenite transformation is reversible, and exhibits a very small hysteresis of 2-5 °C. The SME is very small, while the superelasticity is exhibited at a very narrow temperature range. The R-phase transformation from austenite occurs between 20°C and 40°C in most Nitinol alloys.

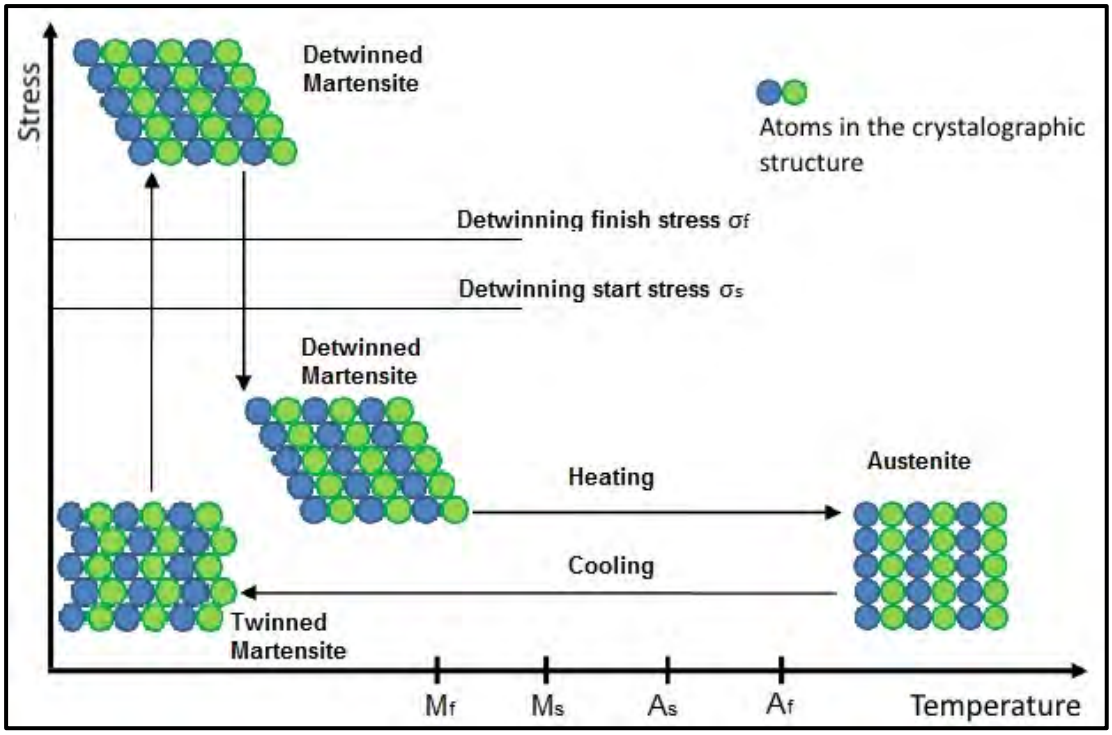

Figure 2-11: Shape memory effect of Nitinol showing the process that occurs at the atomic level when the original shape of a plastically deformed sample is restored upon heating.

The superelastic effect (SEE)

Martensitic transformation can also be induced mechanically at a higher temperature, in which case the superelastic property of the alloy is observed. If a sufficiently large load is applied to the material in the austenitic phase, the material transforms into martensite. Furthermore, after unloading, the original shape is completely recovered.

The mechanical hysteresis appears during loading and unloading of the material in the austenite phase. The Nitinol exhibits a large amount of strain during loading which recovers during unloading. The force needed to initiate the phase transformation is higher than the release force during unloading. Pelton *et al.* (2000) called this mechanical hysteresis - superelastic flags and demonstrated the effect of test temperature on the mechanical properties of the medical-grade Nitinol wire. Tensile tests were conducted at a range of -100°C to 200°C. Wires with an A_s of -2°C and A_f of 11°C were pulled to 6% strain, unloaded to zero stress and then pulled to failure.

Figure 2-12 illustrates stress vs. strain response for superelastic Nitinol in a uniaxial tensile test, for a material having a transformation temperature of 25°C. The material is in austenite phase from position 1 to 2. Upon reaching some level of stress, the material is undergoing a transition from austenite to martensite, this region from position 2 to 3 being called the upper plateau. From 3 to 4, the material has a fully martensitic structure. Upon unloading, the material follows a different stress-strain path from position 4 to 5. This step is followed by a transition back into the parent phase, austenite along the lower plateau to position 6, before full recovering to its original shape at position 1 (Lagoudas 2008).

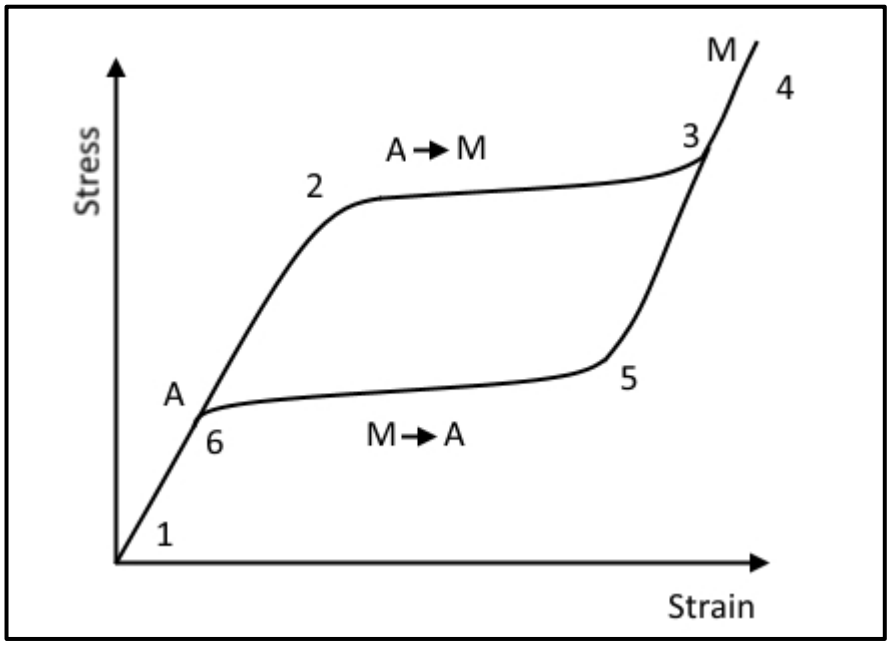

Figure 2-12: Mechanical hysteresis observed between loading and unloading paths showing the phase transformations from austenite (A) to martensite (M) and reverse. The material is in austenite phase in position 1. When reaching a certain stress level at position 2, the transition into martensite begins, which is completed when reaching position 3. In case the stress level increases (position 4), the phase is still martensite, while upon unloading and at certain stress level (position 5), the phase starts changing back to austenite in position 6.

Nitinol has been progressively used in the design of medical devices since late 1980's due to the advantages offered in comparison to other materials (Poncet 2000):

- Recoverability from large deformation: can recover elastically up to 8% strain due to its shape memory and superelastic properties

- Ability to resist kinking and crushing: can resist permanent deformation, a property highly dependent on the operating temperature and the transformation temperature
- Flexibility, torqueability and pushability: can deflect elastically under low stresses, can transfer a rotation action from one end to the other and can transfer axial stresses without buckling
- Ability to generate constant stresses over a large strain range: can exhibit a stress plateau over a large deformation due to its superelastic property
- Constrained or free recovery: can be rigidly constrained when generation of force is required, or can thermally recover its original austenitic shape.

SX stent is one of the most important applications of Nitinol as an implantable medical device and due to the material's superelasticity, SX stent is able to withstand large deformations with the ability to recover its original geometry upon unloading (Stoeckel *et al.* 2003).

NiTiPt Alloys

NiTi alloy has become a popular choice as a material for implantable medical devices due to its amazing shape-memory effect, superelasticity, biocompatibility and fatigue resistance properties. However, the poor visibility under X-ray fluoroscopy of NiTi makes it difficult to accurately position the device in the target area. The same inconvenience also exists in case of monitoring long-term implants and in case of reposition and/or removal of devices. Different methods have been researched in order to improve the radiopacity of the NiTi stents:

- Radiopaque markers have been placed on the circumference of the stent at both ends (Simpson and Boylan 2013). These markers are made entirely from elements with high radiation absorption coefficients, such as Tantalum, Wolfram, Gold and Platinum or by alloying these elements into the NiTi.
- Coating process such as plating of heavy metals onto the stent. Gold is a biocompatible and radiopaque material used for coating stainless steel stents. Experimental usage has shown a promising reduction in thrombus and neointimal formation (Tanigawa *et al.* 1995), however, a few trials in which

gold-plated stents were tested against the bare metal equivalent, showed a higher thrombosis and restenosis rate (Kastrati *et al.* 2000; Nolan *et al.* 2005).

- Alloy addition of a ternary element (iridium, platinum, gold, rhenium, tungsten, palladium, rhodium, tantalum, silver, ruthenium or hafnium) while preserving the superelastic qualities of the NiTi (Boylan 2003; Boylan *et al.* 2006; Chovan *et al.* 2015).

Polymeric Stents

Other materials used in the manufacture of stents are polymers (i.e. Polyethylene, Polypropylene, Polyester). Biocompatibility is critical, therefore, as for any implantable device, rigorous testing must be performed to determine the toxicity of the material, whether there are leachable substances and degradation products. Choosing the right biopolymer is critical for the biofunctionality intended for the device. The material must have adequate physical and chemical properties. It must be light enough to ensure precise handling and other properties such as transparency, colour, lubricity can also be important. From the mechanical perspective, the design engineers must ensure adequate selection by considering the stresses that the product must overcome during its use. The standard plastic stents offer the advantage of low cost. They are BX and SX stents used mainly in refractory benign and/or malignant esophageal stenosis and concurrent tracheoesophageal fistulas. The main disadvantage is the size of the delivery system, measuring up to 42 French for the larger stents.

The biodegradable polymeric stents (BD) enable temporary stenting and are fabricated from biodegradable polymers such as Polydioxanone (PDO), Polylactic acid (PLA) and Poly-L-lactic acid (PLLA). BD stents are SX stents braided from a single filament of biodegradable polymer, or BX slotted tubular stents. BD stents begin to degrade after 4 to 5 weeks and dissolve by gastric acid or other bodily fluids during a period of 2 to 3 months, thus avoiding further procedures and potential morbidity.

Similar to Shape Memory Alloys, Shape Memory Polymers are suitable for manufacturing implantable medical devices which can be delivered via minimally invasive surgeries (Baer *et al.* 2007; Small, IV *et al.* 2010).

Shape Memory Polymers (SMPs)

Shape Memory Polymers are intelligent polymeric materials with the ability to memorise their original shape and return to it from a deformed shape without additional mechanical effort, prompted by a certain stimulus, such as a change in temperature.

Behl and Lendlein (2007), Hu *et al.* (2012), Hager *et al.* (2015) and others have compiled comprehensive reviews of SMPs, presenting their history as well as the current and future developments and concepts.

The term “shape–memory” was proposed by Vernon brothers in 1941 (Vernon and Vernon 1941) for their thermo-plastic resin (polymerised methyl methacrylate PMMA) used in making dental restoration moulds. However, the importance of the SMPs was only recognised in the 1960s, when the smart materials application as heat-shrinkable films and tubes was first introduced. Since then, and especially in the last 10 years, application driven industrial research complemented by academic research has been used to investigate the main mechanisms and design principles of these materials. Dozens of SMPs have been synthesised with applications that span various areas of everyday life. They can be found in electronics and packaging industry as heat-shrinkable tubes (Hitov *et al.* 1964; Perrone 1967), smart fabrics (Mondal and Hu 2006), self-deployable sun sails in aerospace engineering (Liu *et al.* 2014), intelligent medical devices, or implants for minimally invasive surgery (Baer *et al.* 2007; Small IV *et al.* 2010). Japan is considered to be the hub of SMP research, approximately 40% of the research having been published and patented by Japanese researchers according to a literature search conducted in December 2006 (Liu *et al.* 2007).

Previously, in case of SMAs, a temporary shape was set at a low temperature owing to the martensitic de-twinning mechanism. The recovery of the parent shape begins when heating the material above the A_s, the temperature at which the martensite to austenite transformation starts. In contrast, in case of SMPs, a temporary shape can be set and parent shape recovered through different mechanisms. Shape memory research was founded on the thermally induced dual-shape effect of the material. The concept has been extended and indirect actuation of the SME has also been realised

through other stimuli such as irradiation with infrared light, application of electric fields or magnetic fields, immersion in water.

The capability of a polymer to exhibit a SME relies on the polymer's molecular architecture and it is the results of specific polymer processing. The parent shape is achieved by injection moulding or extrusion. Next, during a process called programming, the material is distorted and set into a temporary shape. Upon an external stimulus such as heat, the material would recover its parent shape.

SMPs have several advantages when compared with SMAs (Hu *et al.* 2012):

- SMPs can react to diverse external triggers such as heat, light, magnetic field, chemical action and electricity; these stimuli can coexist, leading to multi-sensitive materials;
- SMPs programming can be highly flexible, being achieved under different stimuli through a single or multi-step process;
- SMPs have a broad range of structural designs; many polymers and foreign materials can be used to develop different SMEs;
- SMPs' properties can be easily engineered and accurately tuned using composites, blending and synthesis methods;
- SMPs can be developed with the aim of exhibiting properties such as biodegradability and biocompatibility when interacting with human body, offering unique opportunities for endovascular devices developed to enhance interventional stroke treatment procedures, including clot removal devices, aneurysm occlusion devices and vascular stents (Baer *et al.* 2007; Small IV *et al.* 2010);
- SMPs can have a low density, property extremely important for applications, such as aerospace devices and airplane components;
- SMPs have a higher capacity for elastic deformation;
- SMPs can be easily processed and at lower costs than SMAs.

Table 2 depicts the main differences between the SMPs and SMAs in terms of physical and mechanical properties (Liu et al. 2007).

Table 2: Comparison between the physical and mechanical properties of SMPs and SMAs (Liu *et al.* 2007).

Property	Shape-memory polymers	Shape-memory alloys
Density g/cm^3	0.9-1.1	6-8
Extent of deformation (%)	Up to 800%	<8%
Young's modulus at T<T$_{trans}$ (GPa)	0.01-3	83 (NiTi)
Young's modulus at T>T$_{trans}$ (GPa)	(0.1-10)x10^{-3}	28-41
Stress required for deformation (MPa)	1-3	50-200
Stress generated during recovery (MPa)	1-3	150-300
Critical temperatures (°C)	-10 – 100	-10 - 100
Transition breath (°C)	10-50	5-30
Recovery speed	<1s – several min.	<1s
Thermal conductivity (W/mK)	0.15-0.30	18 (NiTi)
Biocompatibility and biodegradability	Can be biocompatible and/or biodegradable	Some are biocompatible (NiTi), not biodegradable
Processing conditions	<200 °C, low pressure	High temp. (>1000 °C) and high pressure
Corrosion performance	Excellent	Excellent
Cost	~$10/lb	~$250/lb

An increasing number of research studies focus on the development of biodegradable and/or drug-eluting SMPs (Wache *et al.* 2003; Gall *et al.* 2005; Baer *et al.* 2007; Wischke *et al.* 2009). Bio-degradability property eliminates the need for subsequent device removal, while drug-eluting capability means enhancing its functionality by reducing the occurrence of restenosis.

2.2.4 Form

Raw materials used in the manufacture of stents include tube, wire and sheet. The majority of BX and SX stents are currently made from tubes or wire. A few exceptions made from sheet, such as NIR (Medinol) introduced in 1996 and GR II

(Cook Medical) introduced in 1996, were eventually redesigned from tubing or retracted off the market.

In the sheet design, the pattern was cut initially and then the sheet was rolled in a tubular form and secured by welding or some special locking mechanisms (Stoeckel *et al.* 2002).

The wire stents are created by intertwining or looping wires to create a stable tubular structure. The stents using tubing as material are created by perforating a pattern into the surface of the tube.

2.2.5 Fabrication

The main stent manufacturing techniques currently in use are: laser processing, braiding and knitting (Bonsignore 2003). Traditional fabrication techniques such as chemical etching, micro-electro discharge machining and electroforming have lost their ground in favour of ultrafast laser technology (Tanous 2010).

Laser Processing

Laser processing is the most predominant method of manufacturing stents, particularly coronary and carotid stent designs. The technique, consisting mainly in cutting, fusion and ablation, was adopted due to its unique capabilities: the ability to cut intricate designs, high degree of accuracy, smooth edges which reduces the finishing process, and high throughput. These aspects make laser processing a cost-effective system able to deliver high quality products in a consistent manner (Hetrick 2009).

The industry trend towards smaller micro-machined stents, implying sub-micron tolerances, is the main challenge of the medical device manufacturers. Clinical reports have suggested that strut thickness may influence the restenosis rates (Garasic *et al.* 2000; Kastrati *et al.* 2001; Briguori *et al.* 2002; Pache *et al.* 2003) therefore, medical practitioners are asking for stents designed with thinner struts.

Medtronic Vascular (2003) have aligned to this trend by reducing the strut thickness in their stainless steel coronary stents range with each new generation. Figure 2-13 shows the evolution of these stents from the MSII to S7, which represents the

thinnest version achievable in stainless steel. With the introduction of Driver stent (a laser-fused sinusoidal rings design) in 2003, Medtronic replaced stainless steel with Cobalt Alloy, allowing a further 20% decrease in struts thickness (Medtronic Vascular 2003).

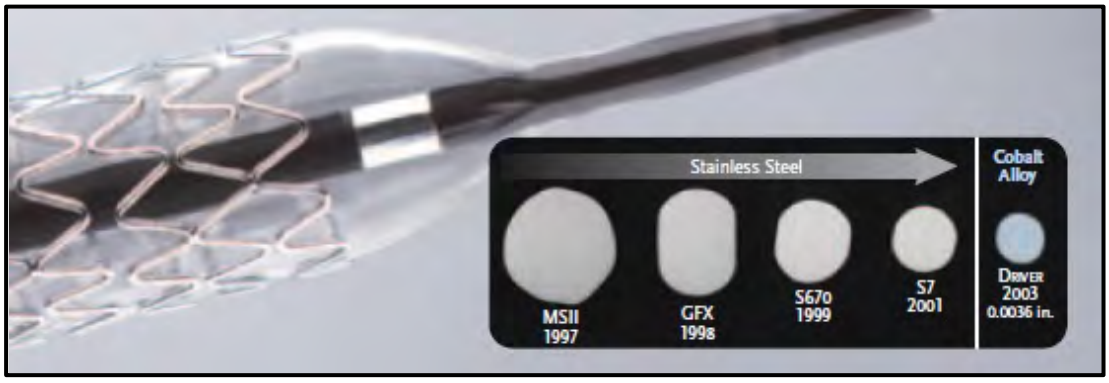

Figure 2-13: The evolution of the coronary stents marketed by Medtronic Vascular, from the stainless steel MSII stent to the Cobalt Alloy Driver stent, showing the gradual decrease in the thickeness of the stent's struts (Medtronic Vascular 2003).

The continuous decrease in the overall dimensions of the stents made the stent manufacturers move away from the conventional machining techniques and turn towards high-speed custom-built laser systems (ROFIN 2014) designed to cut, weld, drill and ablate metal or polymer tubes in an extremely precise and controlled manner (Hetrick 2009). The micro features of the stents have to be processed without compromising the integrity of the rest of the part due to heating. Ultrafast lasers produce little debris and little heat affected zones and therefore are very suitable for the fabrication of stents (Sugioka and Cheng 2014).

Braiding

Braiding is a traditional form of fabric construction and in its simplest definition, braiding means the process of intertwining yarns or fibres in different directions to form flat braids, tubular braids and solid 3D structures (Corbman 1983; Adanur 1995). Due to their construction, braids have some unique characteristics such as high level of conformability, torsional stability and damage resistance (Ko 1987). Typical fibres include natural fibres like cotton and silk, synthetic fibres and thermoplastics as well as engineering fibres like carbon (Figure 2-14), polypropylene, aramid, ceramics, glass fibre and metallic wire.

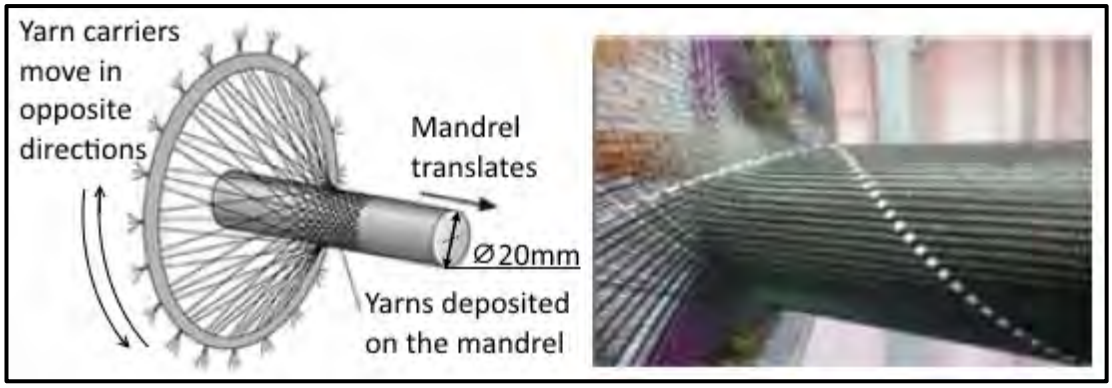

Figure 2-14: Creating a carbon braid preform (adapted from Singapore National Defence R&D Organisation DSO (2012), p.28, illus.).

Braided stents are small diameter tubular structures consisting of two sets of interlacing, spiralling strands, one set clockwise and the other anti-clockwise direction, both lying on the bias relative to the longitudinal axis of the braid. Braided stents can be manufactured on custom-made braiding machines. In this case, the multi-strand design features closed loops at the extremities bonded with the help of laser fusing technology (Figure 2-15a). The stent depicted in Figure 2-15b is created manually using a single piece of Nitinol wire. The seamless design enables crown forming at the extremities of the stent and can be produced on cylindrical or stepped mandrels.

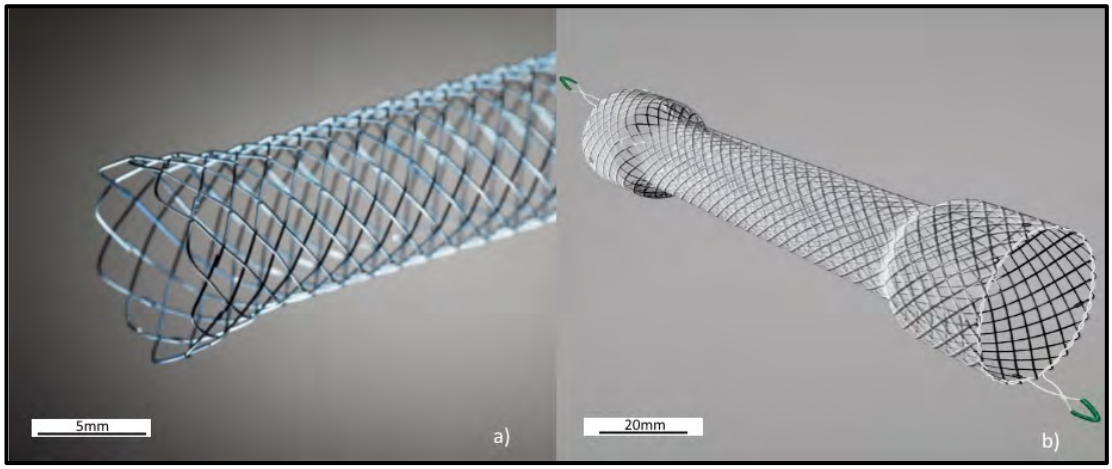

Figure 2-15: Braided stents. a) Multi-wire braided stent: WallFlex Billiary Stent (Boston Scientific 2015) b) Single-wire braided stent: Evolution Esophageal Stent (Cook Medical 2013c).

Knitting

Knitting is a form of interlooping in which the fabric is progressively built row after row. It consists in forming the yarn into loops, each of these loops being released

only after a succeeding loop has been formed and intermeshed with it (Corbman 1983).

Knitting requires usually a smooth, strong yarn with good elastic recovery properties. However, metallic wire can also be used to manufacture a knitted mesh. Knitted structures have a large applicability in the medical devices industry, in form of bandages, casts, surgical gauze, artificial arteries, grafts and stents (Figure 2-16).

Figure 2-16: The Ultraflex Tracheobronchial Stent System is a knitted stent indicated for use in the treatment of tracheobronchial strictures (Boston Scientific 2014).

2.2.6 Platform Geometry

Coil stents are formed from a single piece of wire, the difference between them resulting from the special deflection property of wires. Gianturco-Roubin FlexStent (US Department of Health & Human Services Food and Drug Administration 1993) depicted in Figure 2-17a was characterised by a flat wire coil attached to a single longitudinal strut. Wiktor (1989) proposed an intravascular radially expandable stent design based on a cylindrical open-ended metallic wire coil component and by 1994 his design was marketed by Medtronic (White *et al.* 1994).

BX stents employ mainly a **Slotted tube Design.** These stents are manufactured by laser-cutting slots into a metal tube in a pre-determined design. The spaces cut into the tube allow for plastic deformation during the balloon expansion of the stents. They are produced in crimped or near-crimped condition, the process being followed by deburring and electrochemical polishing as surface treatment. A low strut profile is required to facilitate a low profile for the delivery system. This feature will enable safe positioning of the device in tight, tortuous spaces. BX stent designs have evolved from the Gianturco-Roubin FlexStent (Cook Medical) (Figure 2-17a) to more complex designs which can be grouped in multiple closed cell type designs such as BX Velocity Stent (Cordis, Johnson & Johnson) (Figure 2-17b) and open cell modular type designs such as Multi-Link Stent (Abbott Vascular) (Figure 2-17c).

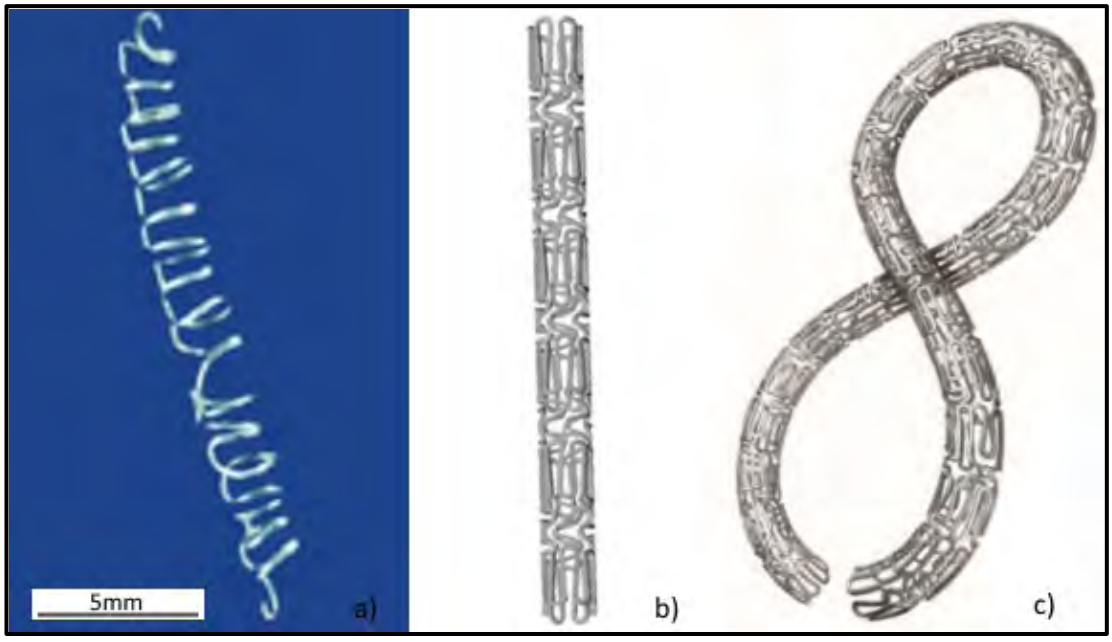

Figure 2-17: BX stent geometries. a) Gianturco-Roubin FlexStent (Cook Medical 1987) b) BX Velocity Stent (Balossino *et al.* 2008) c) Multi-Link Stent (Abbott Vascular 2017).

SX stents can employ a **Tubular mesh Design or a Slotted tube Design.** Generally called woven stents, the mesh stents are manufactured from wire using technologies such as braiding and knitting. They are produced in the expanded dimensions, followed by electro-polishing in order to remove the oxides formed during the manufacturing process (De Scheerder *et al.* 1998; Zhao *et al.* 2002).

Woven stents (Figure 2-18a) provide excellent coverage, however, they shorten substantially after expansion. SX stents in slotted tube design (Figure 2-18b, c) are fabricated by laser-cutting slots into the Nitinol tube in a pre-determined pattern in the expanded configuration. These stents do not deform permanently when crimped inside a delivery catheter. Following deployment, these stents expand to the original dimensions, a step which sometimes is performed with the help of a balloon. These stents are highly flexible and conformable, with medium hoop strength and minimal foreshortening.

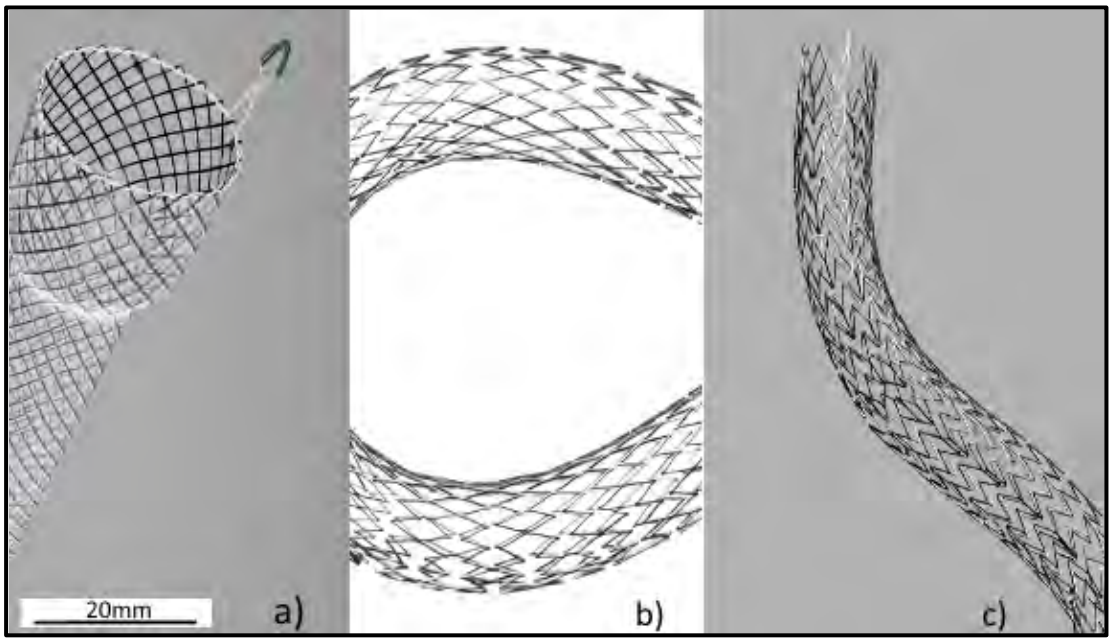

Figure 2-18: Current SX stent geometries. a) Evolution Esophageal Stent (Cook Medical 2013c) b) EverFlex Biliary Stent (Covidien 2015) c) Zilver Biliary (Cook Medical 2013b).

2.2.7 Additions

In this section, enhancements to the stent design related to improving radiopacity, reducing in-stent restenosis and facilitating stent removal are discussed.

Radiopaque markers and coatings

Radiopacity or X-ray visibility is a very important topic for implantable medical devices and stents in particular, because stent visibility facilitates accurate positioning of the device during deployment, detection and monitoring of the stent position. A stent must absorb more X-rays than the surrounding tissue in order to be

fluoroscopically visible. Nitinol is slightly more radiopaque that stainless steel, but far less than other materials such as tantalum, gold or platinum (Poncet 2000). When the thickness of the wire or struts cannot be increased, the radiopacity issue can be addressed by:

- Attaching radiopaque markers made from materials with higher atomic weight (e.g. tantalum, gold, platinum) at both ends of the stent (Stoeckel *et al.* 2002).
- Electroplating or coating the stent material with heavy metals which are not only radiopaque, but are also biocompatible and making sure that the plating layer can withstand similar level of recoverable strain as the base metal.
- Alloy addition of a ternary element to Nitinol (e.g. iridium, platinum, gold, tungsten, tantalum) while preserving its superelastic properties (Boylan 2003; Boylan *et al.* 2006).

Drug-eluting coatings

Drug-eluting stents (DES) have transformed the treatment of CAD due to a reduction of in-stent restenosis. Currently, DES such as Cypher, a sirolimus-eluting stent (SES) from Cordis and Taxus, a paclitaxel-eluting stent (PES) from Boston Scientific are preferred and considered to be superior to bare metal stents in the treatment of coronary diseases. DES consist in the stent platform, drug and stent coating.

The stent coating serves as the interface between the stent platform and the inner wall of the vessel and its purpose is to retain and elute the drug. The most used stent coating technology is non-degradable polymer-based, because of its ability to sustain controlled drug release. In recent years, research has focused on developing biodegradable and biomimetic polymers for the coating, which are considered to be less inflammatory and less trombogenic (Grube *et al.* 2004; Serruys *et al.* 2005; Kandzari *et al.* 2006; Guagliumi *et al.* 2010).

Polymeric coatings and covers

Certain conditions where there is a discontinuity in the lumen, such as a rupture or fistula remain a problem in interventional therapy. A solution to this problem was the development of stent grafts, which integrate a membrane into a stent (Jamshidi *et al.* 2008). Polymeric materials such as Polyethylene terephthalate (PET), Poly tetra fluoroethylene (PTFE), silicone, parylene, polyurethanes (PU) can be applied to the stent surface as a coating or designed as a membrane which covers the stent surface. The addition of the coating reduces tissue hyperplasia and the risk of thrombosis and enables stent removal if repositioning or a temporary placement is required.

2.3 Viscoelasticity

2.3.1 Introduction

Viscoelastic materials are materials which at certain temperatures, exhibit a dual mechanical behaviour incorporating characteristics of both solid materials – elastic behaviour and of fluids – viscous behaviour. The essential difference between elastic and viscoelastic materials consists in the way they store the energy due to deformation (Courtney 2005).

Figure 2-19 illustrates this difference, showing that in case of a linear elastic material, there is a direct proportionality between the strain and stress the material is subjected to. This means that loading and unloading follow an identical path. 100% of the energy due to deformation is stored as potential energy on loading and upon unloading, all of this stored energy is used to restore the initial shape of the material. In contrast with the linear elastic response, viscoelastic materials dissipate some of the stored energy, a phenomenon called hysteresis. This means that unloading follows a different path than on loading. The level of stress attained also depends on the strain rate, which is the rate at which the viscoelastic material is stretched. Viscoelastic response occurs in a variety of materials, from soil and concrete to synthetic and natural polymers. The time-dependent response of these materials is related to their microstructure.

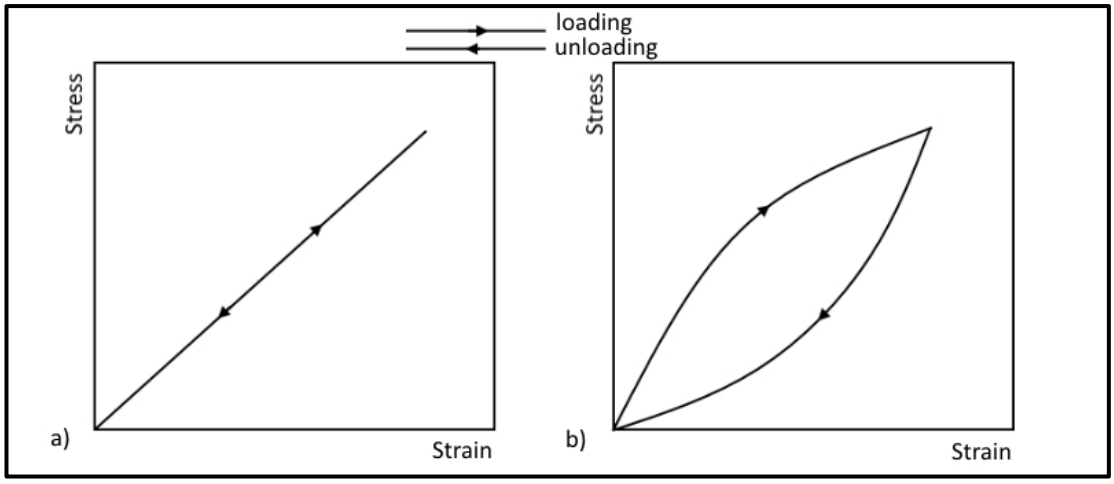

Figure 2-19: Difference between linear elastic and viscoelastic behaviour. a) Linear elastic material showing direct proportionality between stress and strain b) Viscoelastic material showing hysteresis due to different loading and unloading paths.

Polymer Viscoelasticity

Polymers are a typical example of viscoelastic materials. Polymers are chemical compounds consisting of large molecules (macromolecules) created from many repeated subunits (monomers). The ability to dissipate energy makes polymers the perfect choice in shock absorption applications.

Stiffness of materials is generally dependent on the temperature. The elastic modulus is considered constant at room temperature, for materials such as metals and ceramics, due to their high melting temperature, so variations in the material's state at room temperature is neglected. In contrast, polymers have a small temperature range ($-20\,℃\ to\ 200\,℃$) in which they can pass through all states, from brittle behaviour at low temperatures to leathery at glass transition temperature range, then rubbery and finally viscous at high temperatures (Ashby and Jones 1994; Courtney 2005). Considering the polymer's microstructure, the mechanism responsible for the viscoelastic response is the sliding of the molecular chains within the material.

Natural polymers such as hair, bone and tendon also exhibit a time-dependent elastic behaviour. At certain stress levels, these materials can deform elastically up to 10% strain, the strain being totally recovered upon unloading. However, the paths followed during loading and unloading are not identical; rather a pronounced hysteresis is noticed, quantifying the amount of energy that these biomaterials can absorb.

Nitinol Viscoelasticity

The mechanical behaviour of biological materials when loaded/unloaded is completely different than the elastic deformation behaviour exhibited by conventional metallic stent materials like 316L Stainless Steel. However, it is very similar to the behaviour of Nitinol, hence, Nitinol is considered a physiological or biomechanical compatible material.

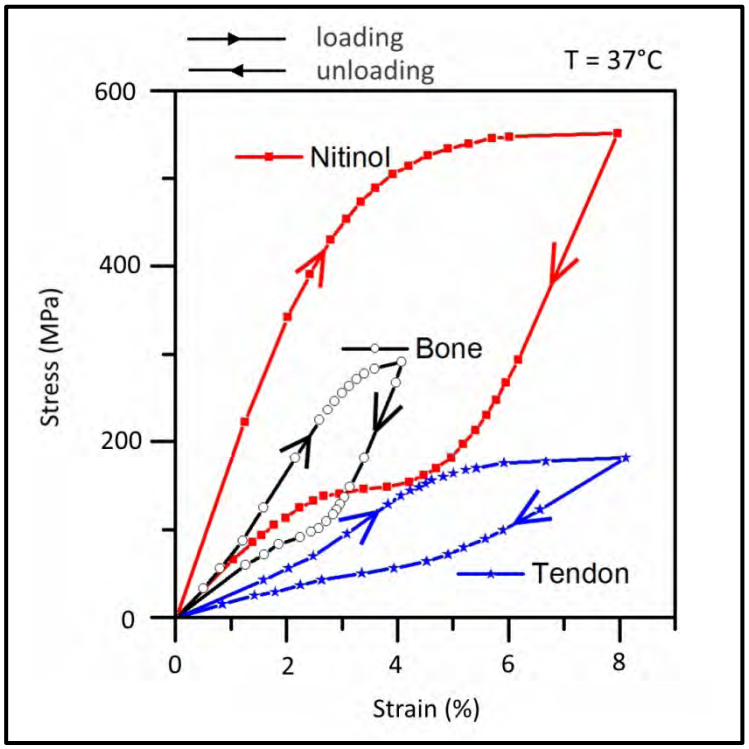

Figure 2-20: Stress hysteresis in biological materials in comparison to Nitinol at body temperature (adapted from Stoeckel *et al.* 2003). The stress vs. strain response of superelastic Nitinol is for a material having a transformation temperature of ~25°C (Pelton *et al.* 2000).

Figure 2-20 shows the stress-strain dependency for bone and tendon, in comparison to medical-grade Nitinol wire with a transformation temperature of ~25°C tested at body temperature (Pelton *et al.* 2000). The loading and unloading paths show plateaus on which these viscoelastic materials are capable to store and recover from large strains without a significant increase, or decrease in the stress level. Large strains of up to 8%-10% can be recovered without permanent deformation (Duerig *et al.* 1999; Stoeckel *et al.* 2003).

2.3.2 Transient Experiments: Stress Relaxation and Creep

To assess the viscoelastic behaviour of materials, transient and dynamic experiments can be performed. Viscoelastic materials can be subjected to two transient experiments: stress relaxation and creep (Figure 2-21). These experiments consist in observing the viscoelastic material's behaviour in time, once it was subjected to a deformation. ***Stress relaxation*** is observed when a material is loaded in order to achieve a certain strain and then for maintaining that strain constant, less and less stress is required, hence the stress relaxes. Considering the proportionality existing between stress and strain, if stress is time-dependent and strain is maintained constant, means that the elastic modulus is also time-dependent. A new parameter called stress relaxation modulus $E(t)$ is defined by dividing the measured stress by the strain applied:

$$E(t) = \frac{\sigma(t)}{\varepsilon} \qquad \textbf{Eq.2.1}$$

where $\sigma(t)$ is the time dependent stress and ε is the strain.

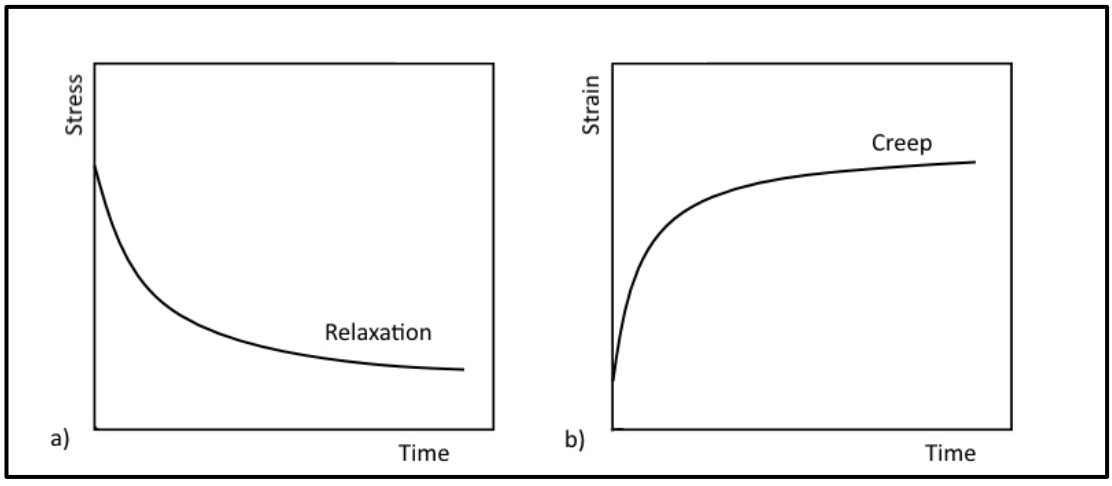

Figure 2-21: Viscoelastic behaviour of a material represented through stress relaxation and creep phenomenae. a) Stress relaxation shows the stress decay in time when a material needs to be maintained under constant strain b) Creep shows the timely increase in strain of a material subjected to constant stress.

Creep is observed when a material loaded under constant stress experiences an increased deformation in time. This behaviour is due to the rotation and movement of segments of the molecules relative to each other. The creep rate is related to the viscosity of the material, the stress applied, temperature and duration of the

experiment. The initial strain ε_0 can be predicted with the help of the instantaneous elastic modulus. After that, the material deforms slowly in time until rupture occurs.

A new parameter called creep compliance $D(t)$ is defined by dividing the measured creep strain by the stress applied and is given by:

$$D(t) = \frac{\varepsilon(t)}{\sigma} \qquad \textbf{Eq.2.2}$$

where $\varepsilon(t)$ is the time dependent strain and σ is the applied stress.

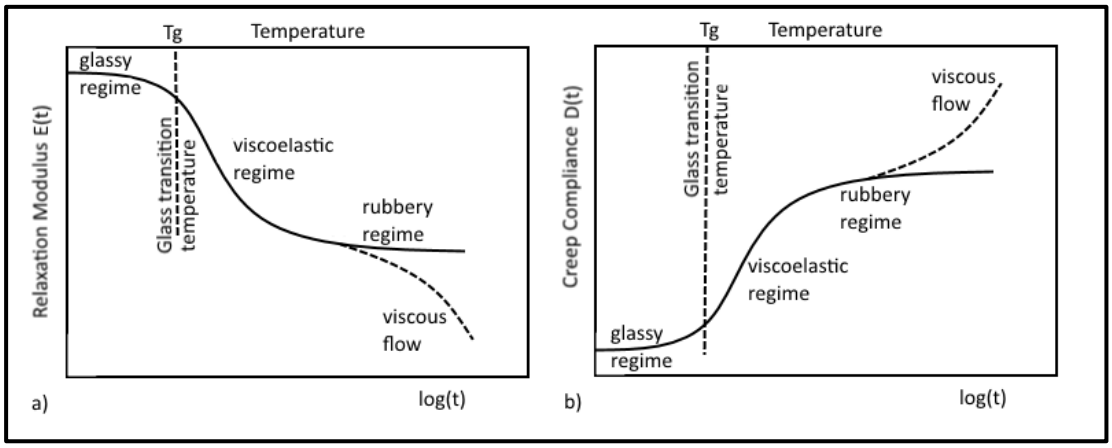

Figure 2-22: a) Relaxation modulus E(t) as a function of time and temperature b) Creep compliance D(t) as a function of time and temperature.

Figure 2-22a shows the relaxation modulus vs. time and temperature for a semi crystalline polymer, such as Polydioxanone with $T_g \cong 20\,℃$ and melting point $T_m \cong 100\,℃$, while Figure 2-22b depicts the creep compliance vs. time and temperature. Both diagrams show the viscoelastic material response to simple extension. Another group of experiments performed on viscoelastic materials are the dynamic tests. These tests are characterised by applying cyclic stress or strain to the material and measuring its response at various frequencies of deformation.

2.3.3 Linear Viscoelasticity

Viscoelastic behaviour of materials can be mathematically described by using differential equations or integrals. Another method is based on assumptions about the molecular structure. Linear viscoelasticity is exhibited in materials subjected to small strains. The creep compliance, as seen in Equation 2.2, is independent of stress, meaning that compliance is the same, no matter the level of stress applied.

This property can be visualised in the strain-stress graph depicted in Figure 2-23, the strain being proportional to the applied stress. At higher strain levels, the material starts to behave in nonlinear fashion, hence the nonlinear viscoelastic behaviour. In this region, there is no linear proportionality between the strain and stress applied.

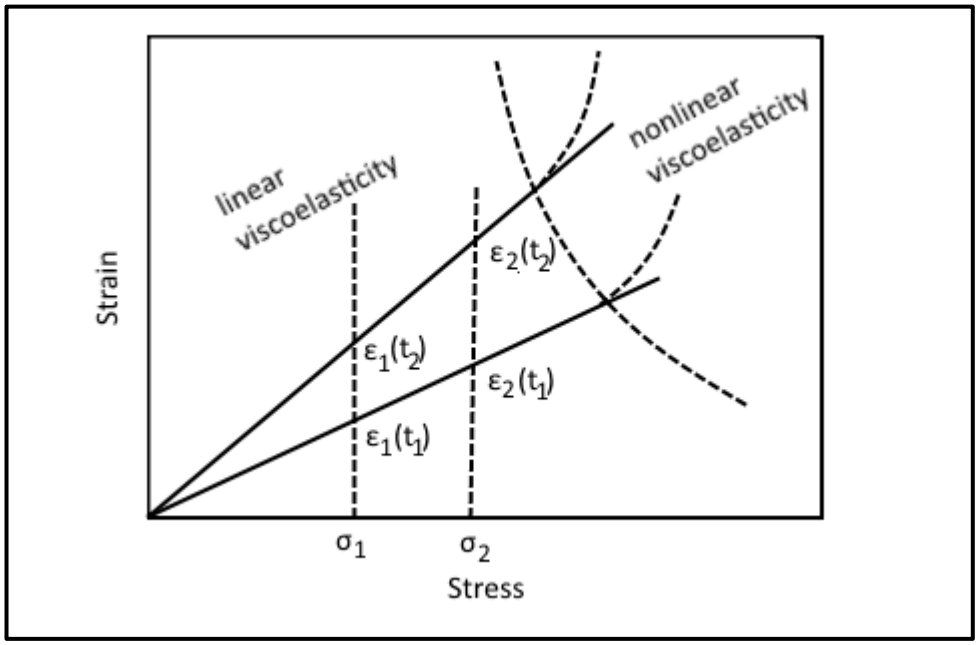

Figure 2-23: Creep compliance represents the slope of lines plotted in the strain-stress graph $\varepsilon(t) = D(t)\,\sigma$. Loading with a constant stress σ_1 leads to an increasing strain $\varepsilon_1(t_1)$ and $\varepsilon_1(t_2)$. If a higher stress σ_2 is applied, the result is a time dependent strain $\varepsilon_2(t_1)$ and $\varepsilon_2(t_2)$. At high stress, the material behaves nonlinearly.

The Differential Model

Viscoelastic behaviour can be described with the help of models which combine mechanical analogues such as springs and dashpots in order to activate the elastic and viscous dual behaviour. The springs are Hookean and the dashpots are Newtonian. The spring represents the linear elastic behaviour of a solid described by Hooke's law:

$$\sigma_s = E\varepsilon \qquad \textbf{Eq.2.3}$$

where σ is the stress, E is the elastic modulus and ε is the strain.

The dashpot represents the viscous behaviour of a fluid described by Newton's law of viscosity:

$$\sigma_d = \eta\dot{\varepsilon} \qquad \textbf{Eq.2.4}$$

where η is the material's viscosity and $\dot{\varepsilon} = \frac{d\varepsilon}{dt}$ represents the strain rate.

By combining these mechanical analogues and connected them in series or parallel, several mechanical models have been developed. The most common ones are presented in Table 3.

Table 3: Mechanical models developed to visualise the viscoelastic effect in materials.

MODEL	DESCRIPTION
The Maxwell Model 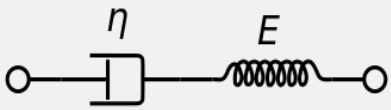	Represented by a spring and a dashpot connected in series. $$\boldsymbol{\sigma_s = \sigma_d = \sigma}$$ Therefore, by combining the two behaviours the following equation can be obtained: $$\boldsymbol{\dot{\varepsilon} = \frac{1}{E}\frac{d\sigma}{dt} + \frac{\sigma}{\eta}}$$ This equation, however, does not properly represent creep behaviour.
The Kelvin-Voigt Model 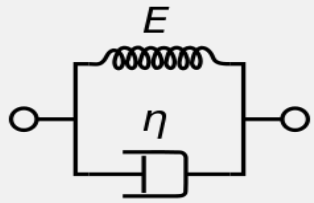	Represented by a spring and a dashpot connected in parallel. $$\boldsymbol{\sigma = \sigma_s + \sigma_d}$$ Therefore, the resulting equation is: $$\boldsymbol{\sigma = E\varepsilon + \eta\dot{\varepsilon}}$$ This equation is better suitable to represent creep behaviour, however, not appropriate for representing stress relaxation.
Standard Linear Solid (Three Parameter Solid) 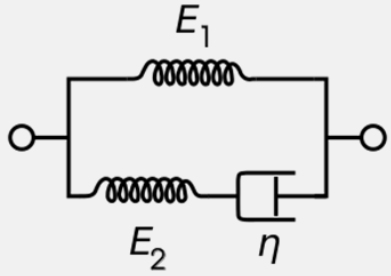	Consists of a Maxwell model and a linear spring connected in parallel. It combines three mechanical analogues: two elastic springs and a dashpot. Therefore, the following equation is obtained: $$\boldsymbol{\dot{\varepsilon} = \frac{1}{E_1 + E_2}\left(\frac{d\sigma}{dt} + \frac{E_2}{\eta}\sigma - \frac{E_1 E_2}{\eta}\varepsilon\right)}$$

The integral model

Boltzmann superposition principle states that creep strain in a material is related to the entire loading history and the strains due to multiple load steps contribute independently and collectively to the total strain. The first condition means that a material remembers deformations that occurred previous to the current loading. The second condition means that each additional load would produce the same additional strain. The condition is valid also when a load is removed (Brinson and Brinson 2008).

According to Boltzmann principle, the total strain of a material subjected to multiple loading is given by:

$$\varepsilon(t) = D(t-\gamma_1)\sigma_1 + D(t-\gamma_2)\sigma_2 + D(t-\gamma_3)\sigma_3 \qquad \textbf{Eq.2.5}$$

where $D(t)$ is the creep compliance at a given time, $\gamma_1, \gamma_2, \gamma_3$ are the times at which three consecutive stresses $\sigma_1, \sigma_2, \sigma_3$ are applied.

Equation 2.5 can be written into a generalised form by making use of hereditary integrals:

$$\varepsilon(t) = D_0\sigma + \int_0^t \Delta D(t-\gamma)\frac{d\sigma}{dt}d\gamma \qquad \textbf{Eq.2.6}$$

where D_0 is the instantaneous creep compliance, σ is the stress applied, $\Delta D(t)$ is the transient creep compliance and τ is a variable referring to the loading history.

Boltzmann's superposition principle can also be applied in representing the stress relaxation data:

$$\sigma(t) = E_0\varepsilon + \int_0^t \Delta E(t-\gamma)\frac{d\varepsilon}{dt}d\gamma \qquad \textbf{Eq.2.7}$$

where E_0 is the instantaneous elastic modulus and $\Delta E(t)$ is the transient relaxation modulus.

2.4 Finite Element Analysis of Stents

Engineering problems in general, can be represented using mathematical models of the physical problem, where the physical problem is described by a set of linear equations, differential and integral equations. However, the complexities found in most real-world problems render impossible solving by hand the governing equations of the underlying physical problem. This is where Finite Element Modelling (FEM) comes into play and proves to be a valuable technique for solving the complex equations and provide design engineers with an approximate, but acceptable solution to the problem. Finite Element Analysis (FEA) and numerical simulations in structural mechanics give a full representation of the stress levels and deformations in response to loading the system, up front in the design process.

2.4.1 The Basics of FEA

The FEA process of a stent starts with understanding the physical problem, identifying all the distinctive features of the structure, symmetry issues and possible simplifications, material nature, type of loading and interaction within the system and with the environment. Once the geometry of the stent is generated, a material model needs to be assigned in order to couple the model with the mechanical properties of the material. Next, boundaries, loads and interactions are defined. Boundary conditions are used to represent parts and properties that are not or cannot be modelled. By applying loads, the structure distorts and stresses are induced. Next step is the discretisation, or meshing, which consists in dividing the stent model into a finite number of discrete regions, called elements, whose behaviour can be described using a set of equations. The finite elements are joined by shared nodes. The collection of finite elements and their nodes make up the mesh of the model. In a stress analysis problem, the displacements of these nodes are the fundamental variables that are calculated by the FE software. Once displacements are known, the strains are determined using derivatives of the displacement fields. The governing equations are solved and the solutions are joined together to generate an approximate solution for the entire system. The final step is post processing and consists in the examination of the generated results and deciding whether the model accurately describes the analysed problem.

The following subchapter reviews the literature on the numerical studies for stents with a focus on the SX braided design.

2.4.2 FEA of SX Braided Stents

The market share of SX braided stents is continuously expanding, therefore there is a need to understand their mechanical behaviour under loading conditions in order to better optimise their design. The FE models need to be equipped with accurate material models capable of capturing the mechanical response of the materials. However, despite the advantages in using FEA in stent design, research literature dedicated to SX braided stents is limited. The lack of scientific efforts in the area of SX braided stents may be due to the complexity of the geometrical model and the subsequent numerical analysis. In terms of material models, a generic linear elastic type has been implemented for metallic stents made of stainless steel or Phynox (Elgiloy), while for Nitinol stents, user defined models covering its superelastic behaviour were developed. FE models for the polymeric braided stents are almost non-existing.

Computational studies for assessing the behaviour of braided SX stents have been carried out since 2005. Canic et al. (2005) analysed mechanical properties of two bare-metal stent grafts: WALLSTENT® Endoprosthesis, an Elgiloy braided stent and AneuRx® stent-graft, a stented graft with self-expandable Nitinol stent rings. The stents' response to hemodynamic forces was compared using mathematical modelling, numerical simulations and experimental measurements. The study was performed under the assumptions that the geometry of the treated vessel is cylindrical, the flow of blood through the cylinder is axially symmetric and that the prosthesis is impermeable. The results of the study identified WALLSTENT as extremely compliant, while the fabric-covered, fully supported stent-graft (AneuRx) exhibited minimal compliancy (the change in the diameter of the prosthesis was minor during a cardiac cycle).

De Beule *et al.* 2007 and De Beule 2008 used FE to analyse the mechanical behaviour of the SX metallic braided stent called Urolume WALLSTENT (Boston Scientific). The geometrical model and meshing were done with the help of pyFormex, a Python based scripting language used for the automated design of

spatial structures and the generation of complex 3D geometries by means of sequences of mathematical transformations. Abaqus was used in the analysis of stent behaviour during axial elongation and radial compression. The FE models were validated using the experimental results reported by Jedwab and Clerc (1993) and (Wang and Ravi-Chandar 2004). The material model implemented for Nitinol covered only its superelastic behaviour and was developed using a User Defined Material Model subroutine (UMAT @ working temperature of 22 °C), while for Phynox and stainless steel stents, a linear elastic model was used. The numerical simulations of free stent expansion provided a good representation of the deformability for the Nitinol and Phynox stents, however, the behaviour of the stent was compromised by the effect of plastic deformation in the case of the stainless steel stent.

Kim *et al.* (2008) developed an experimentally validated model to simulate the mechanical performance of SX Nitinol braided stents during compression and bending, based on sample stents created on a braiding machine built in the laboratory. Geometrical models for the wire stents were created with the help of a pre-processor program in C# programming language by considering the motion of the wire carrier during the braiding process. Kim *et al.* (2008) modelled the Nitinol material as a VUMAT in Abaqus/Explicit, covering its superelastic effect. Hysteresis was observed between the loading and unloading behaviour of the stent during compressive loading. The conclusions of this study were that the hysteresis was caused by the slippage between the constituent wires and the material's superelastic behaviour. Bending behaviour of the braided stents was analysed by observing the cross-sectional shape of the stent during flexing. It was established that bending behaviour was more strongly influenced by the braiding angle than by the number of wires. Kim *et al.* (2008) concluded that braiding angle was the most important parameter in determining the overall mechanical behaviour of the stent.

Zhao *et al.* (2012) evaluated the effect of fabrication technique on mechanical behaviour of stents by conducting FEA on braided (SX Expander stent) and welded wire stents with the same nominal dimensions. The geometrical models of the stents were created with Abaqus/Explicit and a user defined material model for Nitinol was developed (VUMAT subroutine) to outline the stress induced transformation

between austenite and martensite. Also modelled were the sheath (SFM3D4R elements) and the stenosed artery (C3D8R). The mechanical properties of the artery were obtained experimentally and fitted into a reduced polynomial hyperplastic constitutive equation. A hyperelastic-perfect plastic model was used to describe the mechanical response of the plaque. Crimping into a sheath followed by deployment into a stenotic artery was simulated. Zhao *et al.* (2012) were the first to assume a frictional contact and applied a friction coefficient of 0.05 to the stent wire sliding as well as stent-artery interface. The study presented a discussion on the different behaviour of the two types of stents subjected to crimping, discussion covering changes in stent length, cell geometry, radial strength and wire stresses. The results showed a reduced plastic deformation of the braided stent after deployment, which was attributed to the relative sliding between wires. This behaviour impacted on the radial strength, which was lower than the value recorded on the welded model; therefore, the deployed braided stent was more conformed to the anatomic shape of the lesion and much less efficient at restoring the patency of the stenotic vessel. The welded wire stent exhibited a high capacity for pushing the occlusion outward and it reached an almost uniform shape after deployment. The welded joints caused larger deformation and high strain on the stent struts, which indicate a potential earlier failure for the welded stent. In addition, higher contact pressure at the stent-lesion interface and higher arterial stresses were observed in the artery supported by the welded stent (Zhao et al. 2012).

In 2013, Zhao *et al.* conducted FEA on two braided esophageal stents: cup-spherical and straight-shaped. Stress and axial elongation of the stents were compared while changing parameters such as number of wires, wire diameter and length. Zhao *et al.* (2013) developed parametric models of the stents using APDL (ANSYS Parameter Design Language). The models were meshed using 3D beam elements, and a Nitinol material model covering its superelastic behaviour was used. Direct proportionality between the maximum stress and the wire diameter was pointed out as well as between elongation and the length of stent. In the case when all parameters are the same, the axial elongation of cup-spherical-shaped stent is less than that of straight stent meaning less foreshortening of the cup-spherical-shaped stent than that of the straight stent.

Frost *et al.* (2014) performed an experimental and theoretical investigation of the mechanical response of a single wire braided stent with crowns in order to estimate fatigue properties of the stent during cyclic loading. Abaqus/Standard was used in FE computations. Frost *et al.* (2014) employed a rate-independent constitutive model for Nitinol, where R-phase transition was addressed (Sedlák *et al.* 2012). Excellent correlation between the numerical solution and experimental results was reported. It was concluded that the developed model was well suited for FE simulations of the mechanical response of stents. The critical areas with respect to fatigue life performance, were the flexions at the end of the stent. FE simulation provided a reliable estimate for the pressure-stent diameter relation.

Muliana and Rajagopal (2012) have analysed the response of nonlinear viscoelastic biodegradable polymers under mechanical loading coupled with degradation, their work being based on a quasi-linear viscoelastic (QLV) model. The material model was implemented for the PLLA cylindrical stent and the arterial wall using a user subroutine UMAT in Abaqus.

Kim *et al.* (2010) were the first to investigate polymeric braided stents through FEA. The research focused on braided stents fabricated from shape memory polyurethane fibres and the feasibility of developing these temperature-responsive stents was explored. A constitutive equation describing the one-dimensional thermally-induced shape memory behaviour of the polymer was used in creating the material model. The temperature-responsive deployment behaviour of these stents was investigated by simulating their implanting procedure. The polymeric stents showed a gradual expansion as the temperature increases to body temperature, offering the possibility of preventing the creation of a sudden overpressure to the wall of the vessels during their deployment.

FEA of polymeric braided stents was also performed by Peirlinck in 2013. His work consisted in the development of a numerical framework to simulate the deployment and expansion of biodegradable esophageal stents. The geometrical model of the stent was developed in pyFormex, while the analysis was done in Abaqus/Explicit, where a linear elastic material model was used and a steric interaction and friction between the wires was implemented. A degradation study for the biodegradable Ella stent was developed and incorporated in the FE model. The deployment of the

polymeric braided stent within an esophagus was simulated and the results provided knowledge on the stent's capability of opening a tortuous esophageal lumen.

2.5 Summary

The FE studies generally present good results and demonstrate the capabilities that FEM offers to the understanding of the complex mechanical behaviour that SX stents exhibit during deployment. Furthermore, it validates the necessity of building complex numerical models in order to deal with the intricacy introduced by polymers and shape memory alloys with their thermo-mechanical, super-elastic and viscoelastic properties, but also with the complexity of the stent geometry and the interaction between stent and occluded lumen.

Using FE in the analysis of stent design, assessing the influence of various stent design parameters to its clinical performance would enable stent manufacturers to evaluate and improve an array of designs prior to manufacturing and clinical testing. This is strategically important because it reduces the development costs and time-to-market.

Chapter 3
SX Braided Stents

An analytical model for a generic braided stent is described in this chapter. The fundamental concepts regarding the mechanical behaviour of a braided stent under certain loading conditions are presented, based on the theory of mechanical springs by Wahl (1944) and the work of Jedwab and Clerc (1993). Braiding angle, as oppose to pitch angle is used in the equations devised for the change in stent diameter, stent length and mechanical properties such as axial stiffness following an axial loading. Some errors were identified by De Beule (2008) in the work of Jedwab and Clerc (1993) and this chapter verifies and highlights the correct model formulation.

3.1 Analytical Study

3.1.1 Tubular Braid Geometry

The analytical model developed for a generic braided stent uses the pitch angle as one of the reference braid geometrical parameters (Jedwab and Clerc 1993; De Beule 2008). However, the braiding angle, which is the complement of the pitch angle, is the braid parameter which is commonly used by braid manufacturers. The braiding angle is the angle between any helix and the longitudinal axis of the braid (Figure 3-1). The following work uses the braid angle in the mathematical representations of the model.

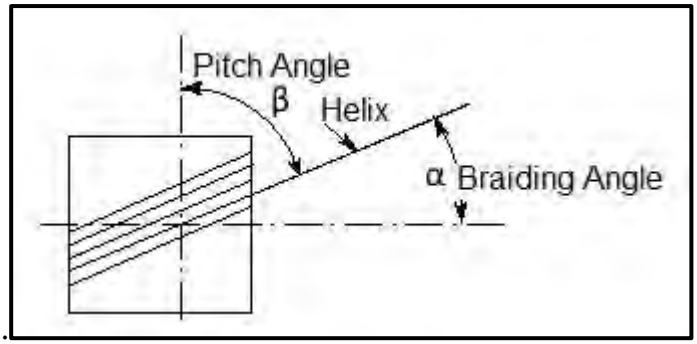

Figure 3-1: Braiding angle vs. pitch angle. The braiding angle is the acute angle measured between the axis of the braid and the axis of a helix.

When considering the tubular braid diameter (Figure 3-2), three parameters can be identified: internal diameter D_i, external diameter D_e, and an average diameter D. The relationship between the three parameters is:

$$D_e = D_i + 4d = D + 2d \qquad \textbf{Eq.3.1}$$

where d is the diameter of the wire.

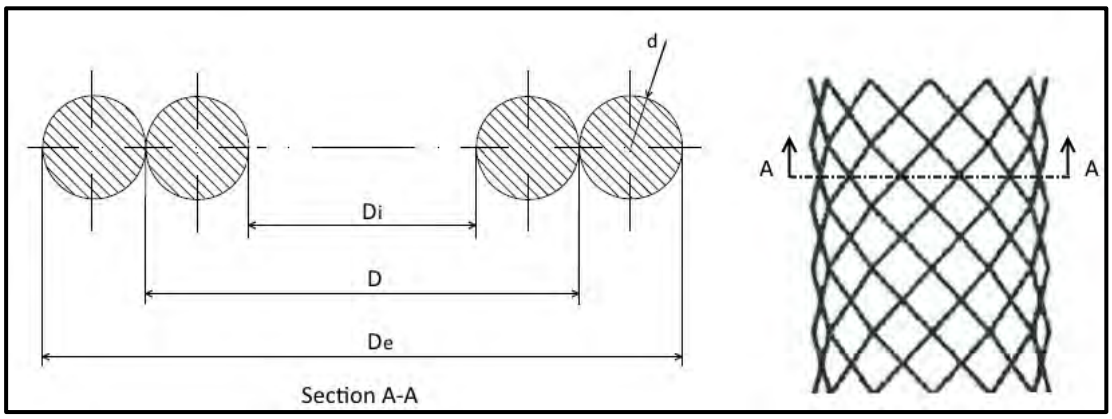

Figure 3-2: Tubular braid cross section A-A depicting two diametrically opposed wire intersections which can be visualised as two tangent circles for each of the wire intersections. The circle diameter represents the wire diameter d.

The geometrical parameters and mechanical properties of a braided stent are listed in Table 4.

Table 4: Geometrical parameters and mechanical properties of a braided stent.

Parameters/Properties	Unit	Description
(D_0) D	(mm)	(Initial) average diameter
(D_{e0}) D_e	(mm)	(Initial) external diameter
d	(mm)	Wire diameter
(L_0) L	(mm)	(Initial) Stent length

(α_0) α	(deg)	(Initial) Braiding angle
(p_0) p	(mm)	(Initial) Helical pitch
n	-	Number of wires
t_h	-	Number of turns in a helix
L_w	(mm)	Total wire length in the braid
δ	(mm)	Axial elongation
F	(N)	Axial load
P	(N/mm^2)	Outer radial pressure
K_L	(N/mm^2)	Longitudinal stiffness
K_p	(N/mm^3)	Radial pressure stiffness

3.1.2 Axial Elongation

When subjected to an axial force F, the stent increases its length from an initial value of L_0 to a final length L (Figure 3-3). In the same time, the stent undergoes a change in the diameter ($D_{e0} \rightarrow D_e$) and a change in the braiding angle ($\alpha_0 \rightarrow \alpha$). Similarly, the pitch value changes ($p_0 \rightarrow p$). The stent elongation is given by: $\delta = L - L_0$.

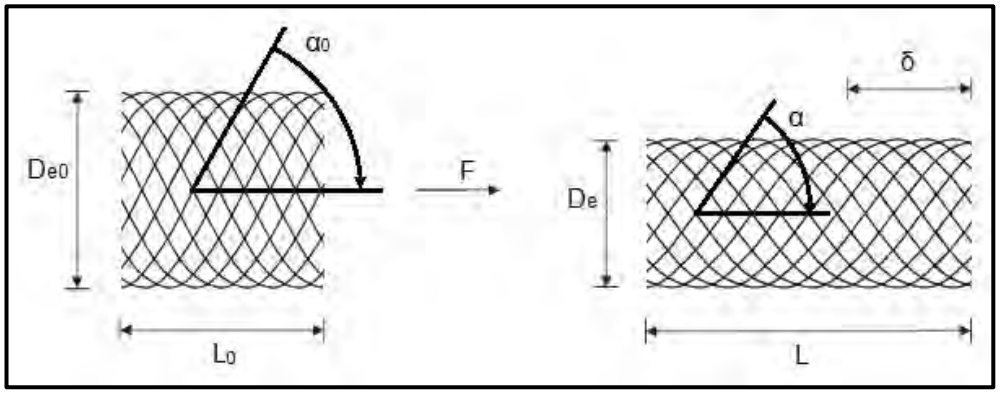

Figure 3-3: Elongated stent under axial loading. The braided structure in the unloaded state has a braiding angle α_0, length L_0 and an external diameter D_{e0}. When subjected to an axial force F, the structure elongates with a value δ. The braiding angle becomes α, length become L and external diameter reduces to D_e.

Figure 3-4 depicts the tubular braid and its 2D surface after being sectioned along the line of a helix. This helix becomes the segment $|AB_0|$ and the surface of the braid is geometrically represented by the parallelogram $AB_0C_0D_0$ in the initial phase, and ABCD when under the action of axial force F. Side $|AD_0|$ and |AD| represent the circumference of the stent in the two phases.

$$|AD_0| = \pi D_0$$

$$|AD| = \pi D$$

Considering ΔAD_0E_0 ($\angle AD_0E_0 = 90°$), the relationship between the braiding angle, helical pitch and circumference of the braid is given by:

$$\tan \alpha_0 = \frac{|AD_0|}{|D_0E_0|} = \frac{\pi D_0}{p_0} \rightarrow \alpha_0 = \tan^{-1}\left(\frac{\pi D_0}{p_0}\right) \quad \textbf{Eq.3.2}$$

The number of turns t_h in a helix is given by:

$$t_h = \frac{L_0}{p_0} \quad \textbf{Eq.3.3}$$

The length of the wire $|AE_0|$ in a single pitch L_{helix} is given by:

$$L_{helix} = |AE_0| = \sqrt{p_0^2 + (\pi D_0)^2} = \frac{\pi D_0}{\sin \alpha_0} \quad \textbf{Eq.3.4}$$

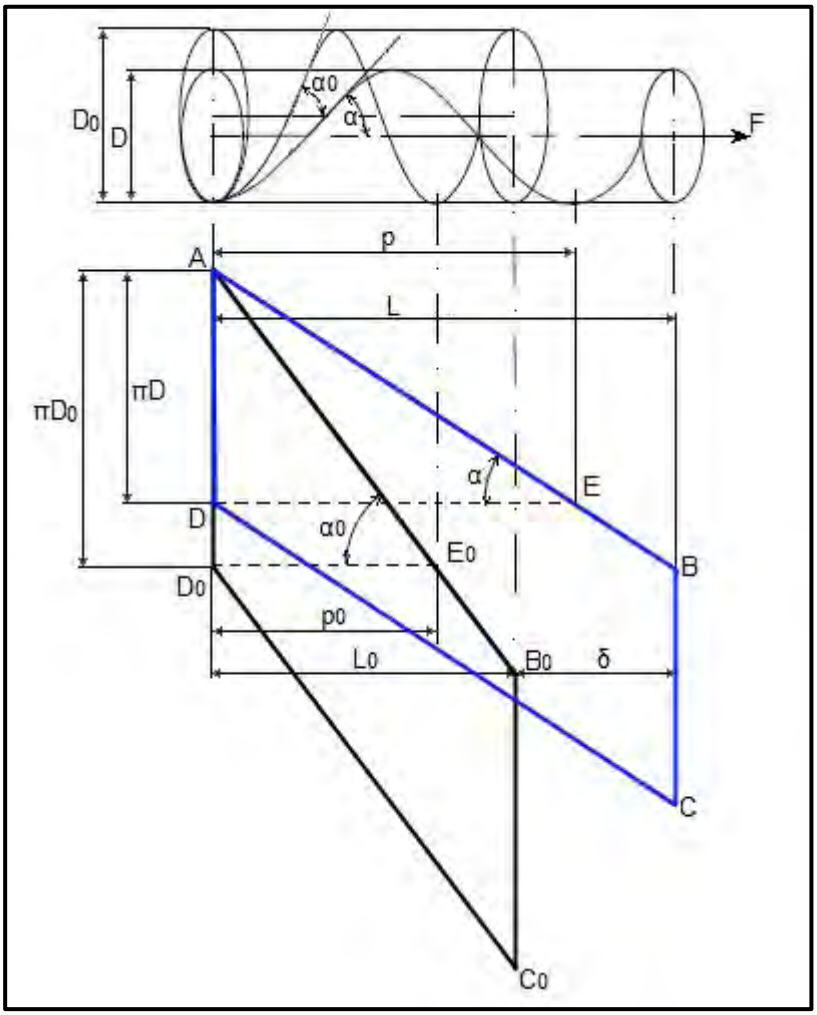

Figure 3-4: Geometry of the braid after the structure has been split along the helix $|AB_0|$ to generate parallelogram $AB_0C_0D_0$. The structure deforms into parallelogram ABCD following the axial loading.

Therefore, the length of the wire $|AB_0|$ in a helix is:

$$|AB_0| = t\sqrt{p_0^2 + (\pi D_0)^2} = \frac{\pi D_0}{\sin \alpha_0} t \quad \textbf{Eq.3.5}$$

The total length of wire L_w required in manufacturing the stent is given by:

$$L_w = nt_h\sqrt{p_0^2 + (\pi D_0)^2} = \frac{\pi D_0}{\sin \alpha_0} nt_h \quad \textbf{Eq.3.6}$$

Similarly, in ΔADE ($\angle ADE = 90°$):

$$\tan \alpha = \frac{|AD|}{|DE|} = \frac{\pi D}{p}$$

$$t_h = \frac{L_0}{p_0} = \frac{L}{p}$$

The length of the wire in a single pitch L_{helix} is given by:

$$L_{helix} = |AE| = \sqrt{p^2 + (\pi D)^2} = \frac{\pi D}{\sin \alpha} \quad \textbf{Eq.3.7}$$

Therefore, the length of the wire in a strand is:

$$|AB| = t\sqrt{p^2 + (\pi D)^2} = \frac{\pi D}{\sin \alpha} t_h \quad \textbf{Eq.3.8}$$

Jedwab and Clerc (1993) have proposed a mathematical model for a metallic SX braided stent (Urolume™ Wallstent® made out of Phynox), model that describes the stent's mechanical function in terms of its geometrical and mechanical properties. During the stent axial loading, the length of the helix doesn't change and any changes in the stent diameter is accommodated by changes in the helical pitch (Wang and Ravi-Chandar 2004). Therefore, a relationship between the initial braid diameter and the diameter after loading can be identified:

$$|AB_0| = |AB| \rightarrow \frac{D_0}{\sin \alpha_0} = \frac{D}{\sin \alpha} \rightarrow D = D_0 \frac{\sin \alpha}{\sin \alpha_0} \quad \textbf{Eq.3.9}$$

The initial length of the braid is:

$$L_0 = |AB_0| \cos \alpha_0 = \frac{\pi D_0 t_h}{\sin \alpha_0} \cos \alpha_0 \quad \textbf{Eq.3.10}$$

while the length after deformation is given by:

$$L = |AB| \cos \alpha = \frac{\pi D t_h}{\sin \alpha} \cos \alpha = \frac{\pi D_0 t_h}{\sin \alpha_0} \cos \alpha \quad \textbf{Eq.3.11}$$

Therefore, the axial elongation of the braid is:

$$\delta = L - L_0 = \frac{\pi D_0 t_h}{\sin \alpha_0}(\cos \alpha - \cos \alpha_0) \qquad \textbf{Eq.3.12}$$

3.1.3 Mandrel Design

The SX braided stent is manufactured by overlapping wires around a metallic, cylindrical mandrel acting as a core (Figure 3-5). The mandrel has a grooved surface for enabling the correct, uniform alignment of the criss-crossing wires. A number of parameters are required when designing the mandrel such as length, diameter, the number of wire intersections along the stent length and across the circumference.

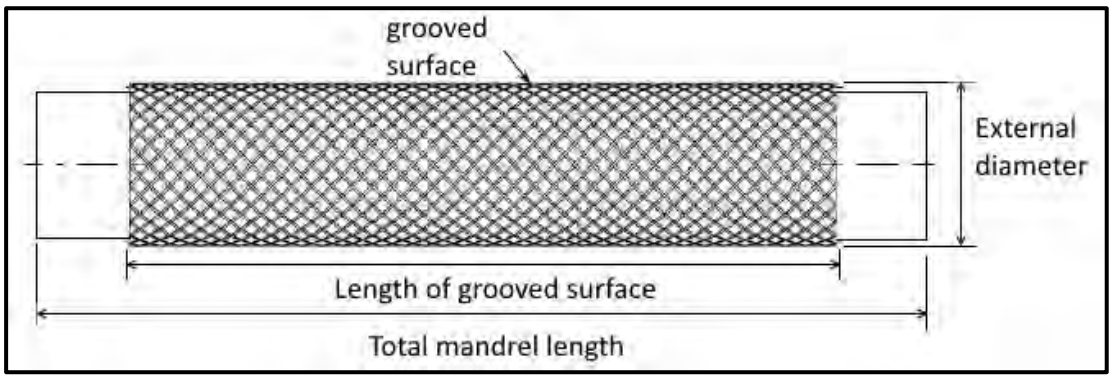

Figure 3-5: Cylindrical mandrel for stent braiding presenting a grooved surface to enable correct alignment of the wires.

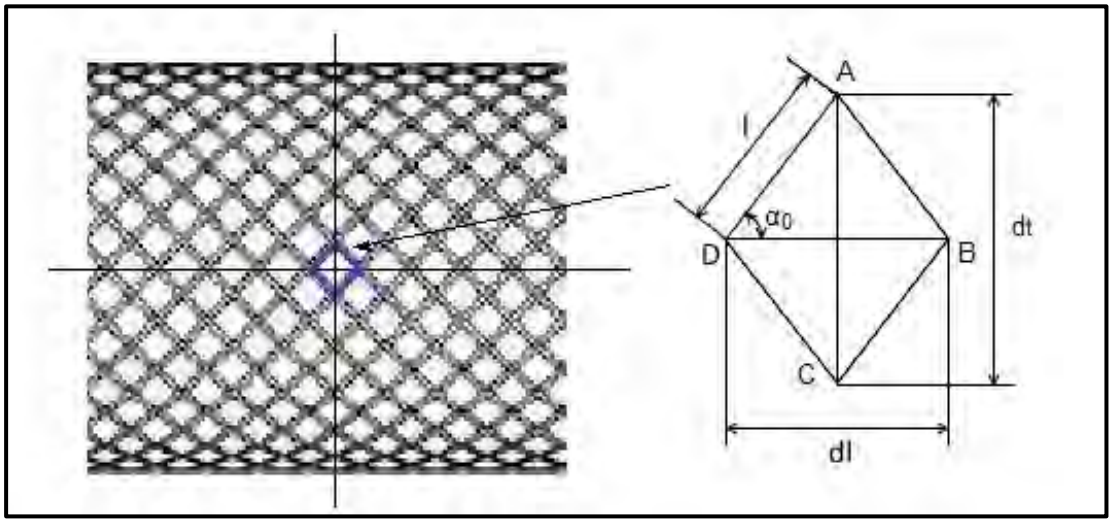

Figure 3-6: The mandrel's grooved surface showing the criss-cross pattern where a unit cell can be represented by a diamond geometry.

Where d_t is the transversal diagonal, d_l is the longitudinal diagonal and l is the length of the side of the diamond.

$$\tan \alpha_0 = \frac{d_t}{d_l} \qquad \textbf{Eq.3.13}$$

From Equations 3.2 and 3.12 ⇒

$$\frac{d_t}{d_l} = \frac{\pi D_0}{p_0} \quad \textbf{Eq.3.14}$$

The transversal diagonal is found by dividing the circumference of the stent into the number of crowns which represent half of the number of wires in the structure.

$$d_t = \frac{\pi D_0}{\frac{n}{2}} = \frac{2\pi D_0}{n} \quad \textbf{Eq.3.15}$$

From Equations 3.14 and 3.15 the longitudinal diagonal becomes:

$$d_l = \frac{2p_0}{n} \quad \textbf{Eq.3.16}$$

From Equation 3.16, the number of intersections in the length of the stent N_{iL} is given by the equation:

$$N_{iL} = \frac{L_0}{d_l} = \frac{nL_0}{2p_0} \quad \textbf{Eq.3.17}$$

The total number of intersections required can be found by multiplying the number of intersections in the length of the stent N_{iL} with twice the number of intersections on the circumference of the stent N_{iT}:

$$N_{iT} = \frac{n}{2} \quad \textbf{Eq.3.18}$$

$$N_i = \frac{n^2 L_0}{2p_0} \quad \textbf{Eq.3.19}$$

The length of the side of the diamond *l*, is given by:

$$l = \sqrt{\left(\frac{d_t}{2}\right)^2 + \left(\frac{d_l}{2}\right)^2} = \frac{1}{n}\sqrt{(\pi D_0)^2 + p_0^2} \quad \textbf{Eq.3.20}$$

3.1.4 Braid Cover Factor

The braid cover factor refers to the area the braid is covering the surface of the mandrel (Zhang *et al.* 1997). The cover factor can be expressed in terms of the braiding angle, diameter of the braid/mandrel and wire diameter (Eq. 3.21).

$$C = 1 - \left[1 - \frac{nd}{2\pi D \cos\alpha}\right]^2 \quad \textbf{Eq.3.21}$$

A braid can reach a jammed state when stretched or shrank at maximum. When in the jammed state, the braid length cannot change anymore due to a change in the braid angle and a further increase in the axial load leads to permanent deformation of the braid strands. The jammed state is characterised by two parameters: jammed angle and jammed diameter. Knowing the value of these parameters is critical in determining the diameter of the catheter used in the stent deployment. From Eq. 3.7 and Eq. 3.21 the cover factor in terms of helix length can be obtained, which is a constant quantity:

$$C = 1 - \left[1 - \frac{nd}{L_{helix} \sin 2\alpha}\right]^2 \quad \textbf{Eq.3.22}$$

In order to obtain the angle values for which the braid is jammed, the cover factor must be 1. This condition leads to Eq. 3.23 and Eq. 3.24:

$$\alpha_j = \frac{1}{2}\sin^{-1}\left(\frac{nd \sin\alpha_0}{\pi D_0}\right) \quad \textbf{Eq.3.23}$$

$$D_j = \frac{nd}{2\pi \cos\alpha_j} \quad \textbf{Eq.3.24}$$

Where n is the number of wires, d is the wire diameter, D_0 *and* α_0 are the initial diameter of the braid and the initial braiding angle.

3.1.5 Mechanical Properties

3.1.5.1 Spring Analysis

When the braided stent is subjected to a tension load F, the stent undergoes a change in length, diameter and braiding angle, with axial elongation shown by Equation 3.10. The structure of the braid is made from a set of identical interwoven helical springs for which the mechanical response is well established (Love 1927).

Based on Wahl's theory of helical springs with ends fixed against rotation and the theory of bending and torsion of thin rods, the curvature and twist of a helical spring in the initial phase and after deformation are given by:

Curvature $$k_0 = \frac{\cos^2 \beta_0}{r_0} = \frac{\sin^2 \alpha_0}{r_0} \rightarrow k = \frac{\cos^2 \beta}{r} = \frac{\sin^2 \alpha}{r}$$ **Eq.3.25**

Twist $$\kappa_0 = \frac{\sin \beta_0 \cos \beta_0}{r_0} = \frac{\sin \alpha_0 \cos \alpha_0}{r_0} \rightarrow \kappa = \frac{\sin \beta \cos \beta}{r} = \frac{\sin \alpha \cos \alpha}{r}$$ **Eq.3.26**

where r_0, r are the radii of the helix, α_0 and α are the braiding angles; β_0 and β are the pitch angles.

In the free-body diagram depicted in Figure 3-7, the components of forces and moments are shown (Wang and Ravi-Chandar 2004). If a moment M' and a force F' are acting simultaneously on one spring, the bending and twisting moments are given by:

$$m_b = M' \sin \alpha - rF' \cos \alpha$$ **Eq.3.27**

$$m_t = M' \cos \alpha + rF' \sin \alpha$$ **Eq.3.28**

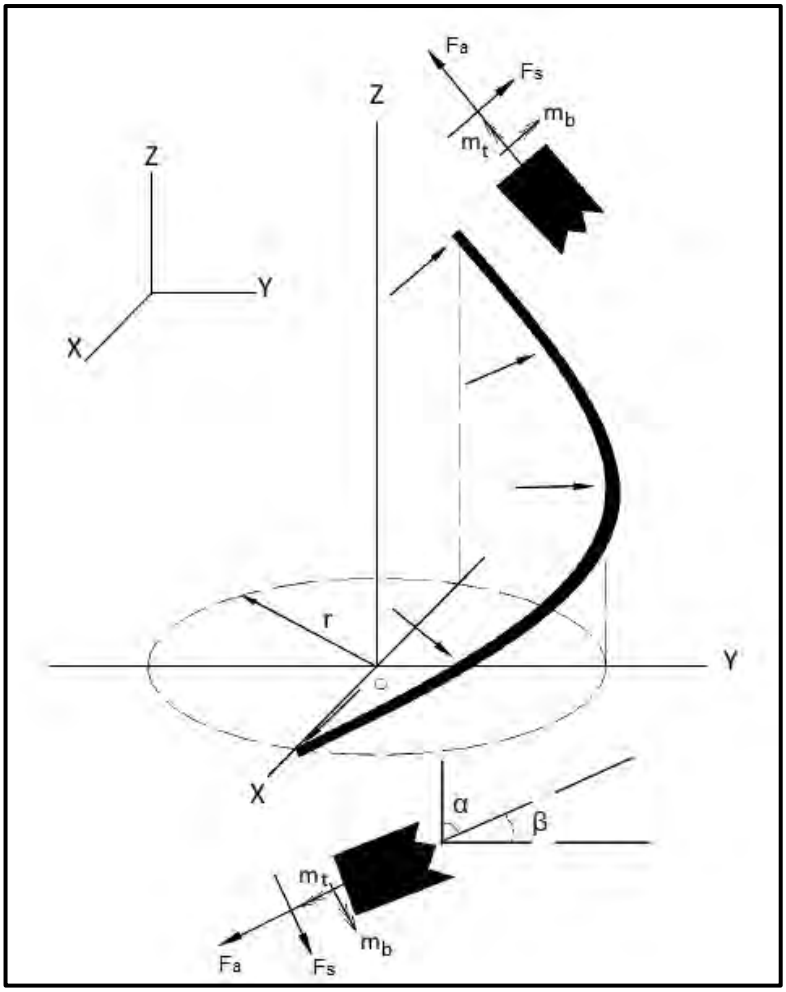

Figure 3-7: Free-body diagram on one-half turn of one wire in the stent (adapted from Wang and Ravi-Chandar 2004a), where r, α, β, m_t, m_b, F_a and F_s are the radius of the helix, braiding angle, pitch angle, twisting and bending moments, axial and shear force.

The change in the spring's curvature is given by the bending moment m_b divided by the flexural rigidity *EI.*

$$\Delta k = k - k_0 = \frac{m_b}{EI} \qquad \textbf{Eq.3.29}$$

$$\rightarrow m_b = EI\Delta k = EI\left(\frac{\sin^2\alpha}{r} - \frac{\sin^2\alpha_0}{r_0}\right) \qquad \textbf{Eq.3.30}$$

The change in the twist is given by the torsion moment divided by the torsional rigidity GI_p.

$$\Delta\kappa = \kappa - \kappa_0 = \frac{m_t}{GI_P} \qquad \textbf{Eq.3.31}$$

$$\rightarrow m_t = GI_P\Delta\kappa = GI_P\left(\frac{\sin\alpha\cos\alpha}{r} - \frac{\sin\alpha_0\cos\alpha_0}{r_0}\right) \qquad \textbf{Eq.3.32}$$

To solve the simultaneous equations (3.27) and (3.28), next step is to multiply (3.27) by cosα, then to multiply (3.28) by sinα, subtract second equation from the first one and substitute (3.30) and (3.32).

$$GI_P\left(\frac{\sin\alpha\cos\alpha}{r} - \frac{\sin\alpha_0\cos\alpha_0}{r_0}\right)\sin\alpha - EI\left(\frac{\sin^2\alpha}{r} - \frac{\sin^2\alpha_0}{r_0}\right)\cos\alpha$$
$$= M'\sin\alpha\cos\alpha + rF'\sin^2\alpha - M'\sin\alpha\cos\alpha + rF'\cos^2\alpha = rF'$$

Therefore, the force and moment (for a single helix) necessary to accomplish the deformation of the stent according to Wahl's spring theory are given by:

$$F' = \frac{GI_P\sin\alpha}{r}\left(\frac{\sin\alpha\cos\alpha}{r} - \frac{\sin\alpha_0\cos\alpha_0}{r_0}\right) - \frac{EI\cos\alpha}{r}\left(\frac{\sin^2\alpha}{r} - \frac{\sin^2\alpha_0}{r_0}\right) \qquad \textbf{Eq.3.33}$$

$$M' = GI_P\cos\alpha\left(\frac{\sin\alpha\cos\alpha}{r} - \frac{\sin\alpha_0\cos\alpha_0}{r_0}\right) + EI\sin\alpha\left(\frac{\sin^2\alpha}{r} - \frac{\sin^2\alpha_0}{r_0}\right) \qquad \textbf{Eq.3.34}$$

If the trigonometrical identities (3.35) for the complementary angles α and β are substituted:

$$\sin\alpha = \sin\left(\frac{\pi}{2} - \beta\right) = \cos\beta$$
$$\cos\alpha = \cos\left(\frac{\pi}{2} - \beta\right) = \sin\beta \qquad \textbf{Eq.3.35}$$

Wang and Ravi-Chandar (2004a) and De Beule (2008) equations are obtained:

$$F' = GI_p \frac{\cos\beta}{r}\left(\frac{\sin\beta\cos\beta}{r} - \frac{\sin\beta_0\cos\beta_0}{r_0}\right) - EI\frac{\sin\beta}{r}\left(\frac{\cos^2\beta}{r} - \frac{\cos^2\beta_0}{r_0}\right) \quad \textbf{Eq.3.36}$$

$$M' = GI_p \sin\beta\left(\frac{\sin\beta\cos\beta}{r} - \frac{\sin\beta_0\cos\beta_0}{r_0}\right) + EI\cos\beta\left(\frac{\cos^2\beta}{r} - \frac{\cos^2\beta_0}{r_0}\right) \quad \textbf{Eq.3.37}$$

where E is the modulus of elasticity, G is the shear modulus, I is the second moment of the cross sectional area and I_p is the second polar moment of the cross sectional area.

$$I_p = 2I = \frac{\pi d^4}{32} \quad \textbf{Eq.3.38}$$

where d is the wire diameter.

F is the total load given by equation $F = nF'$ as the loading force applied to the n wires in the structure.

K_1, K_2, K_3 constants given by:

$$K_1 = \frac{\sin 2\beta_0}{D_0} \qquad K_2 = \frac{2\cos^2\beta_0}{D_0} \qquad K_3 = \frac{D_0}{\cos\beta_0} \quad \textbf{Eq.3.39}$$

From Equation 3.7, 3.35 and 3.39 diameter D can be written as a function of K_3:

$$D = K_3\cos\beta \quad \textbf{Eq.3.40}$$

and by substituting it in Equation 3.33, the equation obtained is:

$$F = nF' = 2n\left[\frac{GI_p}{K_3}\left(\frac{2\sin\beta}{K_3} - K_1\right) - \frac{EI\tan\beta}{K_3}\left(\frac{2\cos\beta}{K_3} - K_2\right)\right] \quad \textbf{Eq.3.41}$$

The expression for the axial load F working on the stent from Equation 3.41 is in agreement with the work by De Beule (2008) which presented it as a corrected version of Jedwab and Clerc (1993) (Equation 3.42).

$$F_{Jedwab} = 2n\left[\frac{GI_p\cos\beta}{K_3}\left(\frac{2\sin\beta}{K_3} - K_1\right) - \frac{EI\tan\beta}{K_3}\left(\frac{2\cos\beta}{K_3} - K_2\right)\right] \quad \textbf{Eq.3.42}$$

Considering C_1, C_2, C_3 constants in terms of the braiding angle:

$$C_1 = \frac{\sin 2\alpha_0}{D_0} \qquad C_2 = \frac{2\sin^2\alpha_0}{D_0} \qquad C_3 = \frac{D_0}{\sin\alpha_0} \quad \textbf{Eq.3.43}$$

From Equation 3.7 and 3.43 the diameter D can be written as a function of C_3:

$$D = C_3 \sin\alpha \qquad \textbf{Eq.3.44}$$

and by substituting it in Equation 3.33 the axial load F expression, written in terms of the braiding angle can be obtained:

$$F = 2n\left[\frac{GI_P}{C_3}\left(\frac{2\cos\alpha}{C_3} - C_1\right) - \frac{EI}{C_3\tan\alpha}\left(\frac{2\sin\alpha}{C_3} - C_2\right)\right] \qquad \textbf{Eq.3.45}$$

3.1.5.2 Longitudinal Stiffness K_L calculation

$$K_L = \frac{dF}{dL} = \frac{dF}{d(L_0+\delta)} = \frac{dF}{d\alpha}\cdot\frac{d\alpha}{d\delta} \qquad \textbf{Eq.3.46}$$

Differentiating the elongation in terms of braiding angle (Equation 3.12):

$$K_L = \frac{2n}{\pi C_3 t\sin\alpha}\left[\frac{GI_P}{C_3}\left(\frac{2\sin\alpha}{C_3}\right) - \frac{EI}{C_3}\left(\frac{2\sin\alpha}{C_3} - C_2\csc^2\alpha\right)\right] \qquad \textbf{Eq.3.47}$$

This result is in agreement with Jedwab's expression in terms of the pitch angle β:

$$K_{L_{Jedwab}} = \frac{2n}{\pi K_3 t\cos\beta}\left[\frac{GI_P}{K_3}\left(\frac{2\cos\beta}{K_3}\right) - \frac{EI}{K_3}\left(\frac{2\cos\beta}{K_3} - K_2\sec^2\beta\right)\right] \qquad \textbf{Eq.3.48}$$

3.1.5.3 Radial Pressure Stiffness calculation

Work results when the axial load F acts upon the stent causing displacement δ, therefore the incremental work is given by:

$$dW = Fd\delta \qquad \textbf{Eq.3.49}$$

Same displacement can also be produced by the action of a radial pressure P applied to the outer surface of the stent πDL, which would result in a radius change.

$$dW = P\pi DLdr = P\pi DL\frac{dD}{2} \qquad \textbf{Eq.3.50}$$

From Equation 3.49 and 3.50, the radial pressure as a function of axial load is given by:

$$P = \frac{2F}{\pi DL} \cdot \frac{d\delta}{dD} = \frac{2F}{\pi DL} \cdot \frac{d\delta}{d\alpha} \cdot \frac{d\alpha}{dD} \quad \textbf{Eq.3.51}$$

Next step is differentiating Equation 3.44 to obtain:

$$\frac{dD}{d\alpha} = C_3 \cos\alpha \quad \textbf{Eq.3.52}$$

Using Equations 3.43, 3.51 and 3.52 the equation for the radial pressure becomes:

$$P = -\frac{2Ft_h}{DL\cot\alpha} \quad \textbf{Eq.3.53}$$

The radial pressure stiffness K_P can be calculated as:

$$K_P = \frac{dP}{dD} = \frac{dP}{d\alpha} \cdot \frac{d\alpha}{dD} \quad \textbf{Eq.3.54}$$

$$\frac{dP}{d\alpha} = -2t_h \left(\frac{F}{DL\cot\alpha}\right)' = -2t \frac{DL\cot\alpha\, F' - F(DL\cot\alpha)'}{(DL\cot\alpha)^2} \quad \textbf{Eq.3.55}$$

Next step is to differentiate in terms of α using the quotient rule and chain rule, knowing that F, tanα, D and L are explicit functions of α, therefore:

$$K_P = \frac{2t_h}{C_3\cos\alpha\,(DL\cot\alpha)^2}\left\{2nDL\cot\alpha\left[\frac{GI_P}{C_3}\left(\frac{2\sin\alpha}{C_3}\right) - \frac{EI}{C_3}\left(\frac{2\sin\alpha}{C_3} - C_2\csc^2\alpha\right)\right] - F\left[C_3\cos\alpha(\pi tD - L\cot\alpha) + \frac{DL}{\sin^2\alpha}\right]\right\} \quad \textbf{Eq.3.56}$$

This result is in agreement with Jedwab's expression in terms of the pitch angle β:

$$K_{P_{Jedwab}} = \frac{2t_h}{K_3\cos\beta\,(DL\tan\beta)^2}\left\{2nDL\tan\beta\left[\frac{GI_P}{K_3}\left(\frac{2\cos\beta}{K_3}\right) - \frac{EI}{K_3}\left(\frac{2\cos\beta}{K_3} - \frac{K_2}{\cos^2\beta}\right)\right] - F\left[\frac{DL}{\cos^2\beta} + K_3\sin\beta(\pi tD - L\tan\beta)\right]\right\} \quad \textbf{Eq.3.57}$$

3.1.5.4 Equivalent stress calculation

The common method of comparison between the analytical model and the FEA predictions is to look at von Mises stress (Khennane 2013; Abaqus Inc 2014). The bending stress σ and shear stress τ can be combined according to Tresca maximum shear strength criterion, therefore the equivalent shear stress τ_e, is given by:

$$\tau_e = \frac{1}{2}\sqrt{\sigma^2 + 4\tau^2} \quad \textbf{Eq.3.58}$$

From Wahl's spring theory for a spring with ends fixed against rotation and knowing the bending moment m_b and twisting moment m_t, the bending stress and shear stress can be calculated.

The bending stress due to the twisting moment m_b (Equation 3.30) is given by:

$$\sigma = \frac{32m_b}{\pi d^3} = \frac{64EI}{\pi d^3}\left(\frac{\sin^2\alpha}{D} - \frac{\sin^2\alpha_0}{D_0}\right) \quad \textbf{Eq.3.59}$$

The shear stress due to the twisting moment m_t (Equation 3.32) is given by this moment divided by the torsional section modulus for the spring:

$$\tau = \frac{16m_t}{\pi d^3} = \frac{16GI_P}{\pi d^3}\left(\frac{\sin 2\alpha}{D} - \frac{\sin 2\alpha_0}{D_0}\right) \quad \textbf{Eq.3.60}$$

The equivalent stress derived from von Mises criterion is given by:

$$\sigma_e = \sqrt{\sigma^2 + 3\tau^2} \quad \textbf{Eq.3.61}$$

3.2 Fabrication of SX Braided Stents

3.2.1 Fabrication Process

The fabrication process for the braided prototypes is described below:

1. A pipe with a diameter of 20mm (rigid Nylon when braiding the polymeric prototypes or metallic when braiding the Nitinol prototypes) was chosen for the construction of the mandrel. A criss-cross pattern reflecting the braiding angle, length and inner circumference needed to be achieved in the braid was drawn onto a sheet of paper and stuck onto the pipe.
2. Holes were created at the corners of the criss-cross pattern at each end of the pipe piece (Figure 3-8 a, b). Metallic pins with a diameter of 1 mm were inserted into the holes.
3. The length of the filament required for fabricating the stent is calculated using Equation 3.6. The final length contains an additional 10% to allow for handling and overlapping. Starting from the middle of a helix, the braid is

formed by overlapping the filament in a pattern 1 over 1 under and around the pins at the edges to form the crowns (Figure 3-8c).

4. Filament excess is cut when the braid is complete and the shape of the structure is heat set with treatment setting as follows: 10 minutes at 50°C for the polymeric stent and 10 minutes at 450°C for the Nitinol stent.
5. Pins are removed after the ageing treatment and the braid is slid off the mandrel (Figure 3-8d).

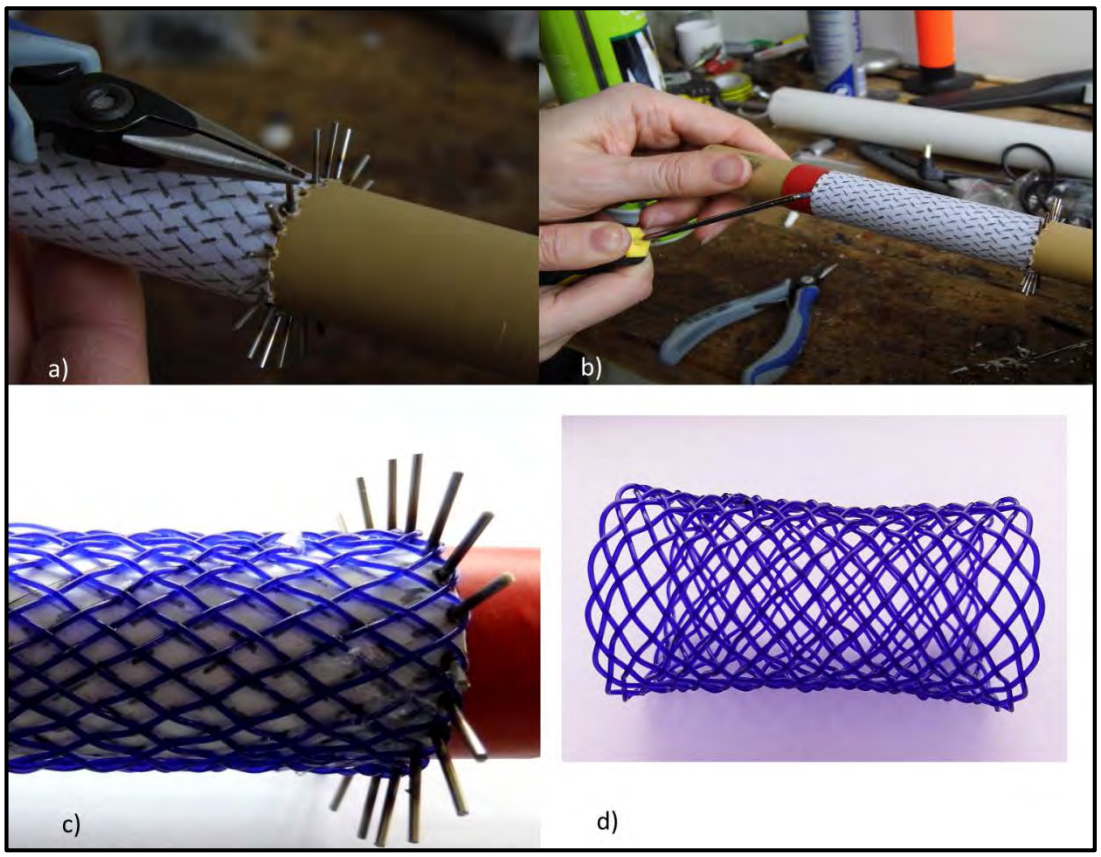

Figure 3-8: Stent braiding fabrication process. a) Cylindrical mandrel closeup b) Creating holes in the mandrel to accommodate the pins for crown formation c) Braided stent closeup showing crown formation around the pins d) Braided stent after removal from the mandrel.

3.2.2 Polymeric Braided Stent

Stent prototypes were braided from Polydioxanone (PDO) biodegradable suture. The monofilament branded Surgicryl and manufactured by SMI AG (Belgium) has a diameter of 0.62mm. The prototypes (Figure 3-9) were fabricated from a single piece of filament in a diamond pattern, where each individual wire passes over and under a single wire which rotates in opposite direction. They were braided on a cylindrical

mandrel in a seamless design which enables crown forming at the extremities of the stent.

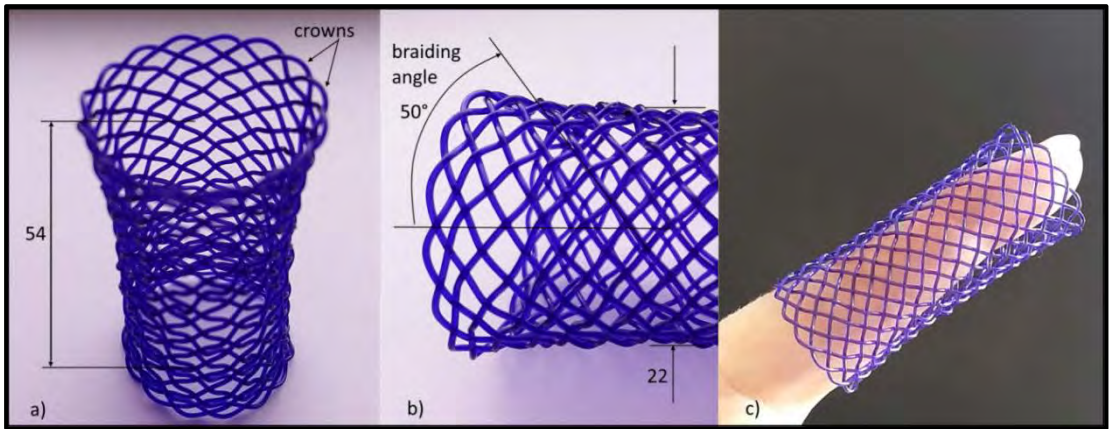

Figure 3-9: PDO hand braided stents with 15 crowns, fabricated from a single piece of filament with diameter 0.62 mm in a diamond pattern. a) Braided stent in upright position, with a length of 54 mm and showing the crown formation at ends b) Braided stent resting flat, with an outer diameter of 22 mm and a braiding angle of 50° c) Stent placed on the index finger to give an indication of the dimensions.

The geometrical parameters of the braid are presented in Table 5. The stent specification did not attempt to emulate a commercially available design; however, the choice of the physical characteristics would make it suitable for the airway or gastrointestinal tract application (e.g. Polyflex Airway (Boston Scientific) with 50 mm length, 22 mm outer diameter).

Table 5: Geometrical parameters of the polymeric braided stent.

Diameter	22 mm
Length	54 mm
No. crowns	15
Braiding angle	50°
Filament diameter	0.62 mm

3.2.3 Nitinol Braided Stent

Stent prototypes were also braided from medical grade Nitinol single wire with the austenite finish temperature A_f of 10 °C and diameter of 0.32 mm. Prototype dimensions resemble the specification for a colonic stent (e.g. WallFlex Colonic Stent marketed by Boston Scientific). The stents depicted in Figure 3-10 were

fabricated in a diamond pattern under the geometrical specification provided in Table 6. The prototypes were heat set in order to remove the internal stresses introduced during sharp bending of the wire at the crowns. The heat treatment leads to a change in the transformation temperature range (Pelton *et al.* 2000), therefore a thermal analysis is required to identify these values and it is presented in Chapter 4, section 4.2.1.

Table 6: Geometrical parameters of the Nitinol braided stent.

Diameter	22 mm
Length	54 mm
No. crowns	15
Braiding angle	50°
Filament diameter	0.32 mm

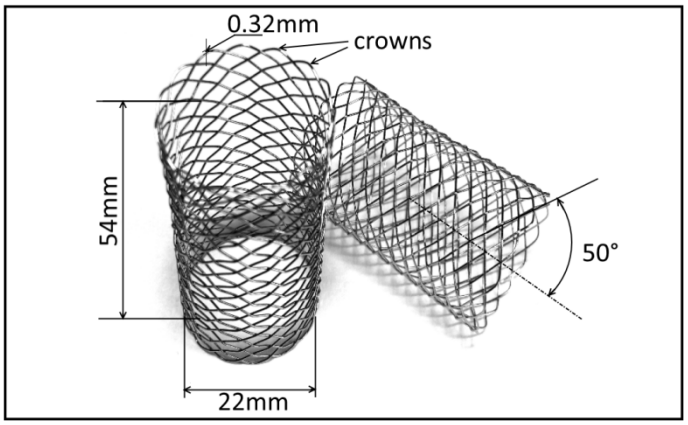

Figure 3-10: Nitinol hand braided stent prototypes fabricated in a diamond pattern.

Chapter 4 Experimental Techniques

For the purpose of material characterisation, a set of experiments are designed and performed. In this chapter, the experimental techniques required for the development of the FE material models are described. The polymeric material is subjected to a uniaxial tensile test and a uniaxial creep tensile test, in order to capture its mechanical properties. The Nitinol wire is subjected to a uniaxial tensile test to assess its superelastic behaviour. A thermal analysis (Discrete Scanning Calorimetry) is also performed, to identify the transformation temperatures of the material. To acquire the radial force, crimping tests are performed on the polymeric and metallic prototypes. The stent's radial force is measured on an experimental setup comprising of a compression device RCM-H60 manufactured by MPT Europe connected to a Zwick Single Column uniaxial tensile testing machine. A detailed description of the technique used to capture raw data required for the calculation of radial force is given.

4.1 Polydioxanone Material Testing

Polydioxanone is a biodegradable polymer, completely reabsorbing in 6 months due to hydrolysis under the action of bodily fluids (Kumbar *et al.* 2014). It is colourless and flexible, exhibiting a low glass transition temperature $T_g \leq 20$ ℃ and a melting temperature of 106 ℃ (MatWeb 2017a). The main applications are extruded filament

used as a surgical suture or as braided stents in cardiovascular applications, bioabsorbable implants in orthopaedics, plastic surgery and tissue engineering. As a polymer, PDO exhibits a time dependent behaviour, where stress and strain induced when a load is applied are a function of time. PDO is also temperature sensitive.

PDO is a semicrystaline polymer (55% crystallinity) characterised by a similar amount of crystalline and amorphous domains. At temperatures well below T_g, the polymer is glassy, brittle with tightly packed molecules. When loaded at these temperatures, the secondary bonds stretch and upon removal of the load, the elastic deformation is recovered, thus, in the glassy region, the polymer behaves like a linear elastic material, exhibiting almost a constant elastic modulus. In the T_g range, the polymer state changes from glassy into leathery, viscoelastic. The elastic modulus decreases very much with the increase in the temperature by over three orders of magnitude. The phenomenon is due to the thermal expansion of the polymer which increases the separation between the molecular chains and reduces the bonding between them. The material becomes more flexible and upon unloading the elastic deformation is recovered in time. With the increase in temperature, the polymer state changes into a rubbery behaviour. When loaded, the primary bonds stretch, molecular chains straighten out, but the entanglements of the molecular chains act as cross-links and prevent sliding. Upon unloading, the deformation is reversible and the structure goes back into disorder. However, the material doesn't exhibit extensive reversible deformations; therefore it does not exhibit a true-elastomeric behaviour. Increasing the temperature even more changes the state to a viscous flow, in which the molecular chains slide and covalent bonds melt.

Two tests were undertaken to determine the mechanical properties of the polymer: a short-term tensile test and a creep tensile test. The short-term uniaxial tensile test is required to determine the instantaneous elastic modulus of PDO. The creep test is used to determine the viscoelastic, time dependent behaviour of PDO under constant loading.

4.1.1 Uniaxial Tensile Test

The tensile strength measurement was performed using a Tinius Olsen Benchtop Tester H25KS. A 1kN load cell was used. The test specimens were prepared by

cutting lengths of 500mm filament. The diameter of the monofilament was measured at three points on the specimen and an average value was calculated. The specimen was wound twice and held between two serrated roller grips (Figure 4-1). The length of filament between the axial lines of the rollers was 100mm. The specimen was pulled at a constant crosshead speed of 10mm/min (Peirlinck 2013) until fracture of the monofilament occurred. The peak load was recorded as tensile strength. The tests were conducted at temperature of 18 °C ± 2 °C. The test procedure was programmed in QMAT 5.3 S-Series Software and the raw data was plotted in a load versus extension format.

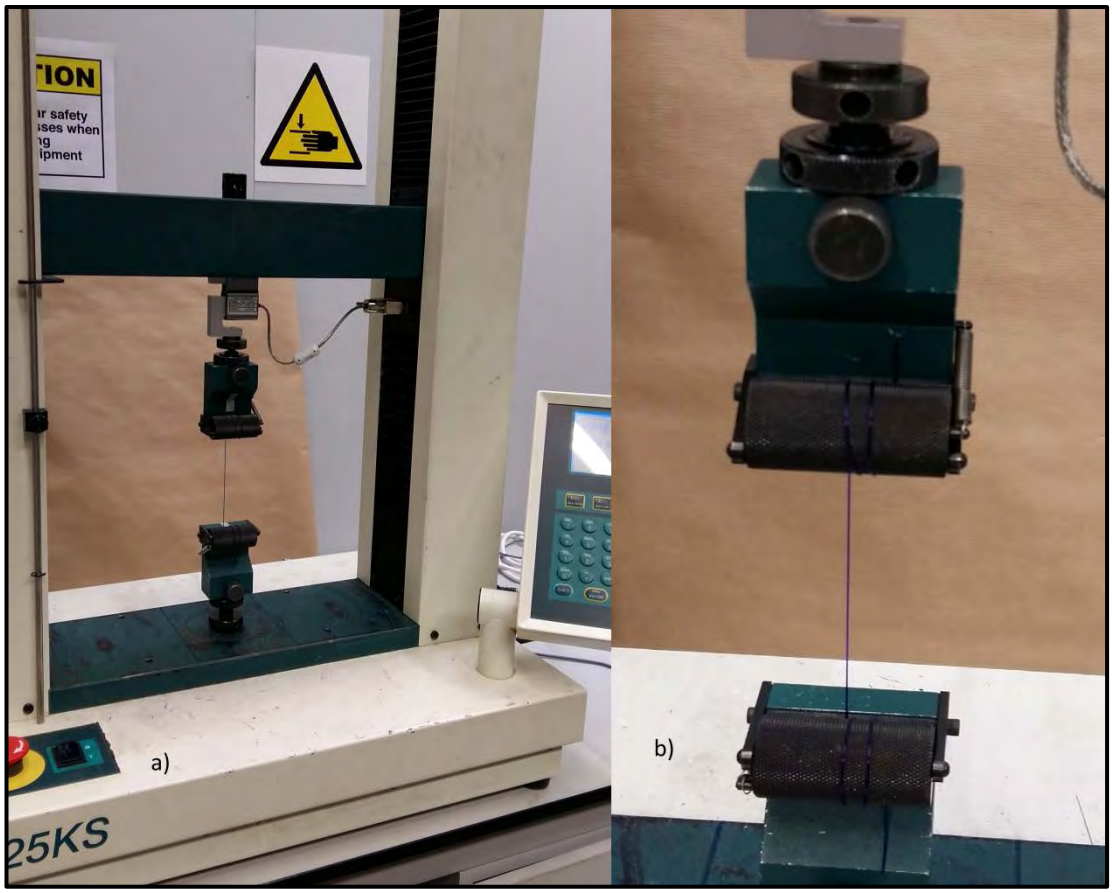

Figure 4-1: Uniaxial tensile test of the PDO monofilament conducted at the temperature of 18 °C ± 2 °C and a strain rate of 10% per minute. a) Setup using Tinius Olsen Benchtop Tester H25KS b) Detail of the serrated roller grips used for holding the test specimens. The specimen was wound twice and held between the serrated roller grips prior to pulling.

4.1.2 Tensile Creep Test

The tensile creep test is a long-term tensile test in which the material is subjected to a step constant load. Rupture may occur when the structure is exposed over an

extended period of time to continuous stress below the yield level, which magnifies the importance of understanding how the material properties change over time and the influence of ambient factors.

The elongation of the specimen was measured using a measuring tape mounted on an in-house built pendulum fixture, with the specimen anchored at one end and a weight hanging at the other end. Masses of 500g, 1000g, 2000g, 4000g, 7000g and 8000g were used. The length of the specimen was 500mm. The tests were conducted over 10-20h at temperature of 20 °C ± 2 °C and a relative humidity of 50% ± 5%. The loads and extensions were converted into engineering stress and strain.

4.2 Nitinol Material Testing

Two experiments were undertaken to determine the mechanical properties of the Nitinol material: a thermal analysis and a uniaxial tensile test. The thermal analysis is used to determine the new transformation temperature range (TTR) following the ageing treatment that the stent was subjected to. The short-term uniaxial tensile test is required to determine the material constants required in calibrating the FE material models.

4.2.1 Thermal Analysis

The transformation temperatures were determined using a Discrete Scanning Calorimeter (DSC) analysis. A DSC analysis is usually performed on stents during the manufacturing process as a quality check. It must be ensured that the device exhibits the superelastic effect at body temperature, so that when deployed in the target lumen, the stent self-expand to the diameter that was set during the ageing treatment. Therefore, the pass/fail criteria is based on the value of A_f, which must be below 37 °C. In this study, a DSC was performed to identify the four transformation temperatures for two purposes:

1. To help with deciding the test temperature for the uniaxial tensile test and radial crimping test of the braided stent;

2. To identify the temperature range for martensite and austenite formation respectively, which are needed in computing the stress/temperature gradients of the material.

The DSC is a technique which measures the energy absorbed or released by the specimen as it is heated or cooled, practically monitoring the phase transitions. The temperature scan was performed using a Perkin-Elmer Pyris 1 DSC with intracooler and was used to investigate the temperature dependent processes of Nitinol material phase transformations. The temperature range was -60 °C to +200 °C and was achieved using a linear temperature ramp with a rate of 20 °C/min. The wire specimens were approximately 3 mg.

4.2.2 Uniaxial Tensile Test

The uniaxial tensile testing experiment was performed on a Tinius Olsen Tester H25KS using a 1kN load cell as shown in Figure 4-2. The test was conducted on three wire specimens of 150 mm in length and 0.32 mm in diameter at 22 °C temperature.

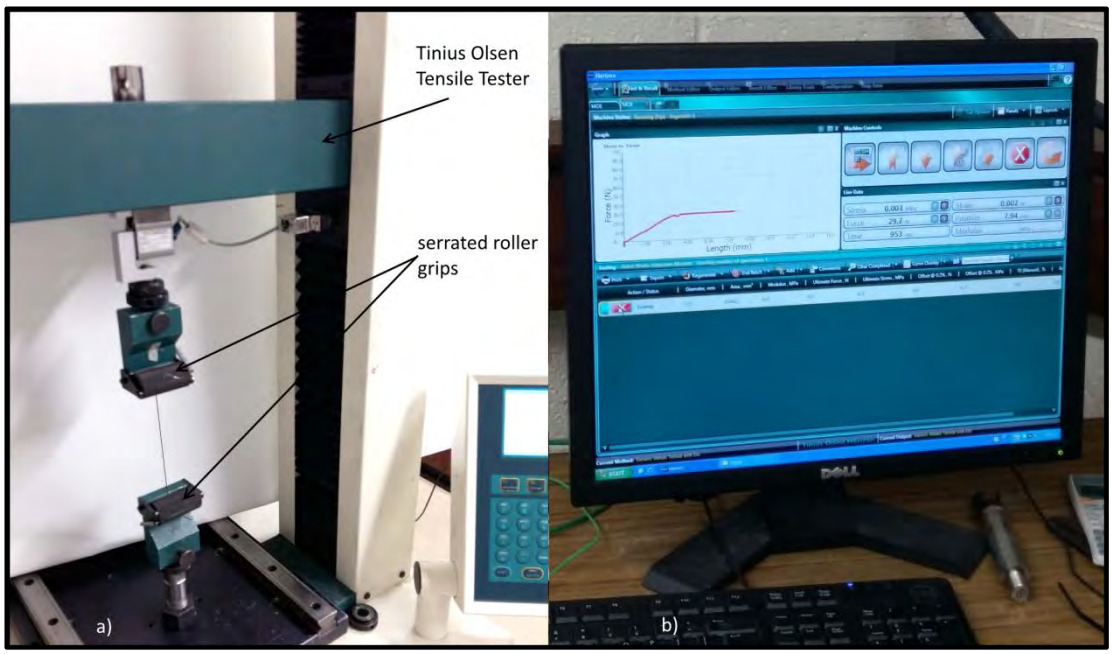

Figure 4-2: Uniaxial tensile test of the Nitinol wire conducted at the temperature of 22 °C. a) Setup using Tinius Olsen Benchtop Tester H25KS showing the serrated roller grips holding the wire specimen b) Test data (force versus crosshead position) was captured using Horizon software.

The specimens were held between two serrated roller grips and subjected to a load/unload cycle (loaded up to 6% strain, unloaded to zero strain at a crosshead speed of 0.2 mm/min) and then were pulled to failure (at a crosshead speed of 0.4 mm/min). Crosshead motion was used to calculate strain.

4.3 Stent Crimping Test

In the absence of a standardised crimping testing procedure, researchers and stent manufacturers have developed custom made rigs and procedures to enable measuring the stent radial forces. Dyet *et al.* (2000) assessed the radial strength for a selection of metallic BX and SX stents using a point load compression test. The force required to reduce the stent diameter by 50% was determined. The equipment used was a digital balance, a range of calibrated weights and a micrometer. Wang and Ravi-Chandar (2004) developed a test method for the characterisation of the mechanical response of a SX metallic stent subjected to internal and external pressure. The SX braided stent was subjected to an external pressure which was applied using a polyethylene bag. Isayama *et al.* (2009) were the first to use a radial force testing machine. The equipment RX 500 manufactured by Machine Solutions US, had a crimper head with 12 crimping segments and used to measure radial force: radial reactive force during crimping and chronic outward force during unloading. A radial compression measurement system manufactured by MPT Europe was used by Peirlinck in 2013 to measure radial force of a PDO braided stent during a degradation study.

In this study, a similar machine manufactured by MPT Europe was used to determine the radial force during crimping and unloading. The stent crimping experiment was performed to quantify the radial forces required to reduce the diameter of the stent from 22 mm to 14 mm. Radial forces that stent exhibited during the uncrimping step were also recorded.

The experimental setup for measuring the stent's radial force is depicted in Figure 4-3 and it consists of a compression device RCM-H60 (MPT Europe) connected to a Zwick Single Column uniaxial tensile testing machine. The compression device consists of a crimping head with 8 segments which close and open radially.

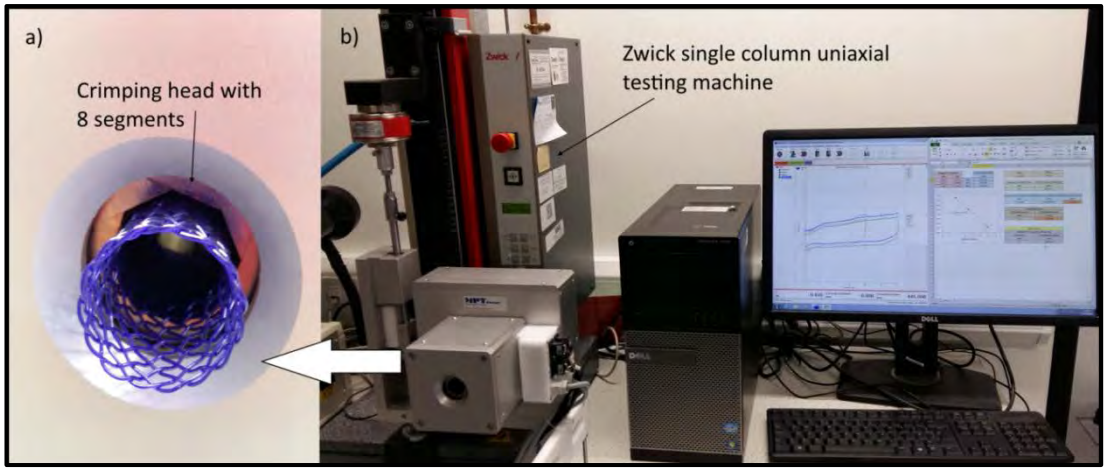

Figure 4-3: Radial Force Tester device RCM-H60 (MPT Europe) used to perform the crimping operation. a) Close-up of the crimping head with the 8 segments which can close and open radially b) Setup of the radial force tester including a Zwick Single Column uniaxial tensile testing machine and a computer system for acquiring test data.

A calibrated load cell of 100N was used to measure the forces during loading and unloading of the stents from their outer diameter of 22 mm to 14 mm at a crimping speed of 0.1 mm/s. Test temperature was 20 °C for the polymeric stent and 22 °C for the Nitinol stent.

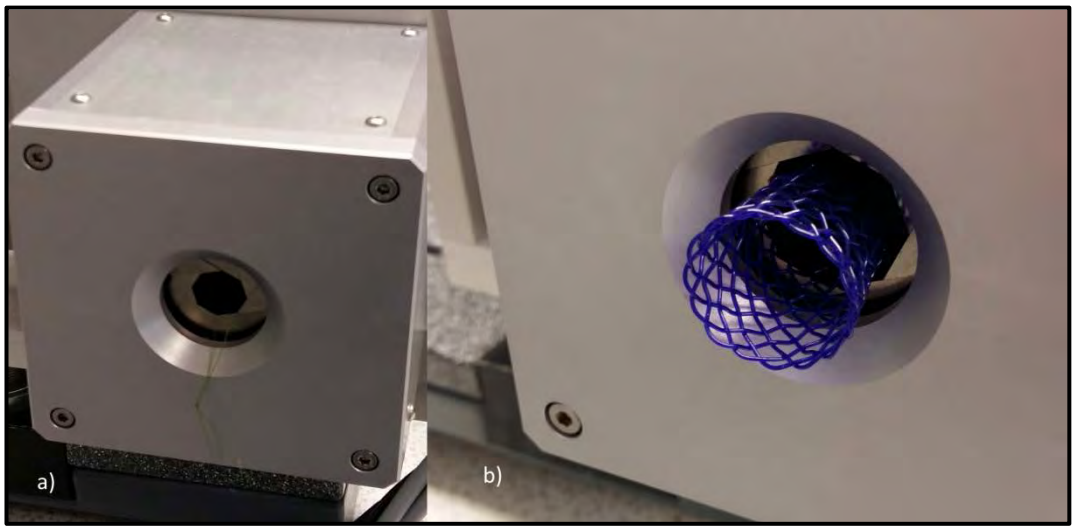

Figure 4-4: a) Compression device RCM-H60 (MPT Europe) b) Closeup of the radial force tester with stent introduced inside the opeing of the crimping head.

A diameter calibration was performed at room temperature prior to the test to establish the curve relating the axial movement of the crosshead to the diameter of the crimping head. The calibration consists in finding the diameter of the crimper at three different displacements of the crimper head. Room temperature was chosen for

the experiment being the temperature at which the crimping procedure of the stents is performed in the manufacturing setting.

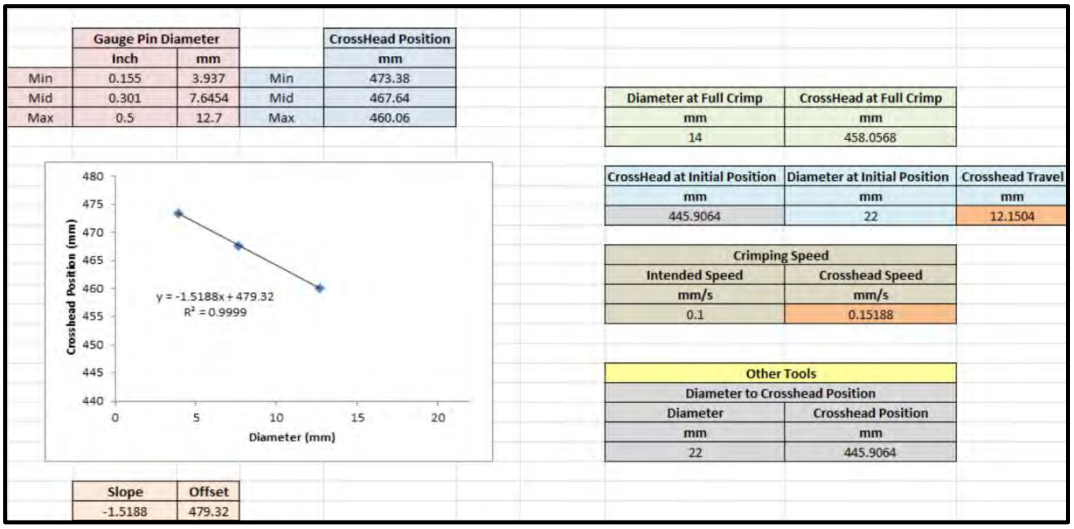

Figure 4-5: Calibration of the crimper head analytics. Crosshead position vs. diameter is plotted and slope is used in determining the crosshead positions required in the stent crimping experiment.

The values of the three diameters were entered in a spreadsheet and the curve representing the crosshead position versus crimper diameter was established as shown in Figure 4-5. The slope of this curve was subsequently used in the deduction of the crosshead's initial and final position that would represent the reduction of the stent diameter from 22 mm to 14 mm.

4.3.1 Stent Crimping Procedure

- Stent prototypes were fitted with a loop of thread at one end to enable ease of removal from inside of the crimping head.
- The stent is introduced into the crimper head with the initial diameter of 22 mm.
- The device crimps the stent to a diameter of 14 mm, then it returns to the start-up position.
- The device performs a cyclic test with 3 load-unload cycles.

A "friction force test" is also performed to determine the radial force required to change the diameter of the crimper to the same specification, in the absence of the stent. This test allows for evaluation of the friction force within the crimping head,

which is subsequently subtracted from the radial force measured during the test with a stent.

Three PDO braided stent prototypes and three Nitinol braided stent prototypes fabricated in-house were subjected to the crimping experiment.

4.3.2 Radial Force Calculation

The results of the second cycle are used for the determination of the force-diameter curve. The raw test output is the force measured at the load cell (F_{load}) and the crosshead position. The crosshead position is converted into crimping head diameter (D_{head}) using the calibration data obtained prior to the crimping test. The force at the load cell is converted into radial force (RF) according to the following equation (MPT Europe 2014):

$$RF = \frac{F_{load} * L_{lever} * a}{\sqrt{27^2 - \left(\frac{D_{head}}{2}\right)^2}} \quad \textbf{Eq.4.1}$$

where L_{lever} = 135 mm is the length of the lever arm connecting the load cell to the crimping head and a is the crimping machine constant a = 3/5. The radial force measured without the stent (FF) which accounts for the frictional effect in the setup, must be extracted from RF.

4.4 Experimental Results – Polydioxanone

4.4.1 Uniaxial Tensile Test Results

The purpose of conducting the uniaxial tensile test was to determine the instantaneous elastic modulus of PDO material. The loads/extension data captured was converted into engineering stress and strain data (Figure 4-6). Young's modulus was deducted graphically, as the slope of the straight line drawn on the linear elastic region of the stress-strain curve. The results of the test are depicted in Table 7.

The mean value of 720MPa for Young's modulus was used in the development of the material model. This result is comparable with the value of 690MPa, which represents Peirlinck's (2013) elastic modulus published result for the tensile test performed at 37 °C on the PDO filament. The difference is justified by different test

conditions, in particular the lower temperature at which the current testing was performed. Strength and stiffness decrease with increasing temperature (Wineman and Rajagopal 2000). Therefore, the close agreement proves that the experiment led to a reliable result, even though was not performed according to a mechanical testing standard.

Table 7: Mechanical properties of PDO monofilament presented as the mean value $\pm$ one standard deviation from the mean.

	Young's Modulus E (MPa)	Tensile Strength σ (MPa)	Elongation at Break (%)
Mean $\pm$ *SD*	**720 ± 37.5**	**321 ± 21.2**	**47.9 ± 7.0**

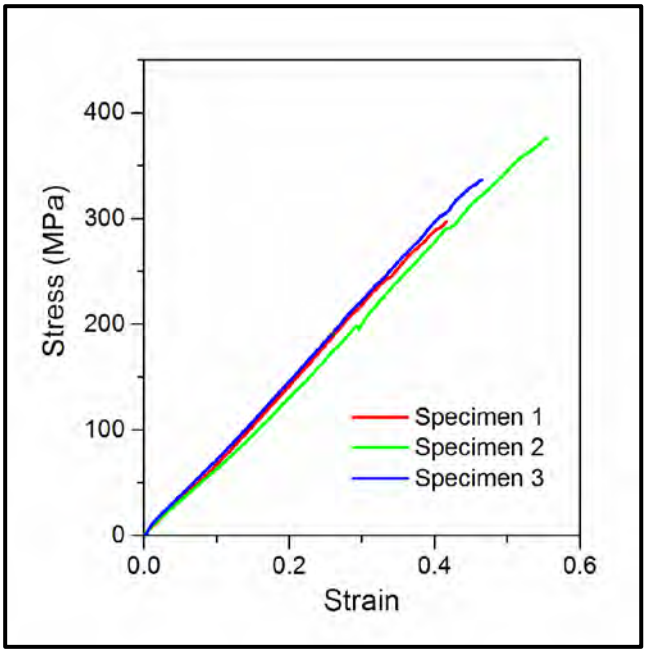

Figure 4-6: Engineering stress-strain curves resulted from the tension pull test to failure.

4.4.2 Tensile Creep Test Results

Viscoelastic creep data is presented by plotting the strain as a function of time. As shown in Figure 4-7, the deformation of PDO under long-term static constant tensile stress is directly proportional to the applied stress. PDO is assumed that it exhibits linear viscoelastic property and therefore, the creep compliance is independent of stress. Figure 4-8 depicts the adjusted radial forces of the polymeric stent, based on the radial forces and friction forces calculated using Equation 4.1.

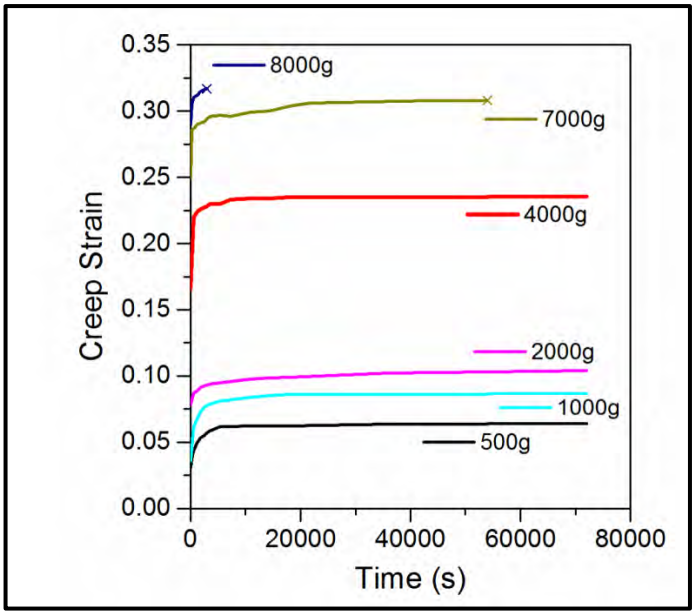

Figure 4-7: Creep strain vs. time following tensile creep experiment on Polydioxanone monofilament. Rupture occurred for the specimens tested at 7000g and 8000g.

4.4.3 Braided Stent Radial Force

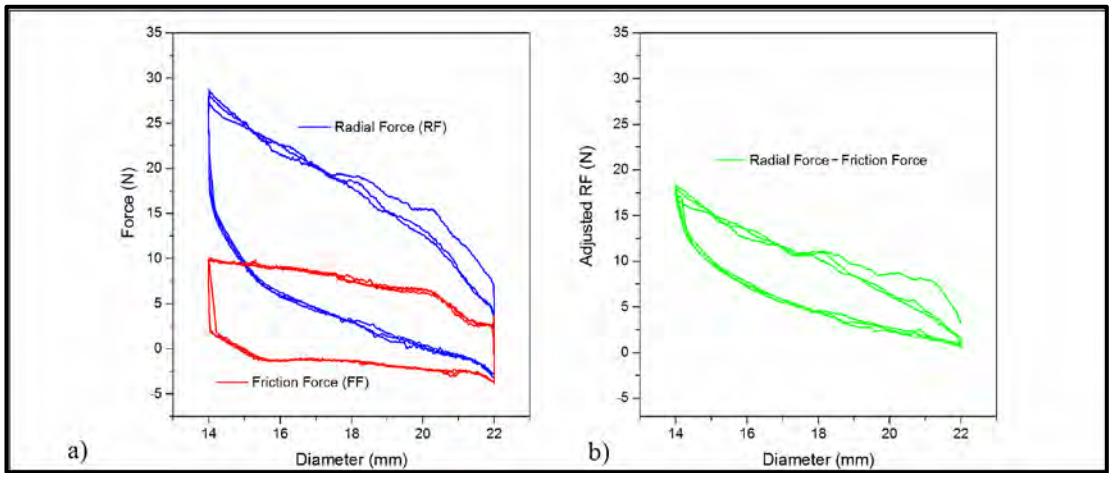

Figure 4-8: Computed values of radial force versus stent diameter for the polymeric stent. a) Radial force (*RF)* and friction force (*FF)* calculated using Eq. 4-1 and represented graphically as a function of stent diameter b) The adjusted radial force represents the radial force of the stent after subtracting the friction force within the crimping head.

4.5 Experimental Results – Nitinol

4.5.1 Thermal Analysis

The results of the Differential Scanning Calorimetry (DSC) analysis of the Nitinol wire annealed at 450 °C are shown in Figure 4-9. The range of the transformation temperatures was determined using this technique. Both, heating and cooling steps

revealed a two-phase transformation (Martensite → R-phase→ Austenite) and (Austenite → R-phase → Martensite).

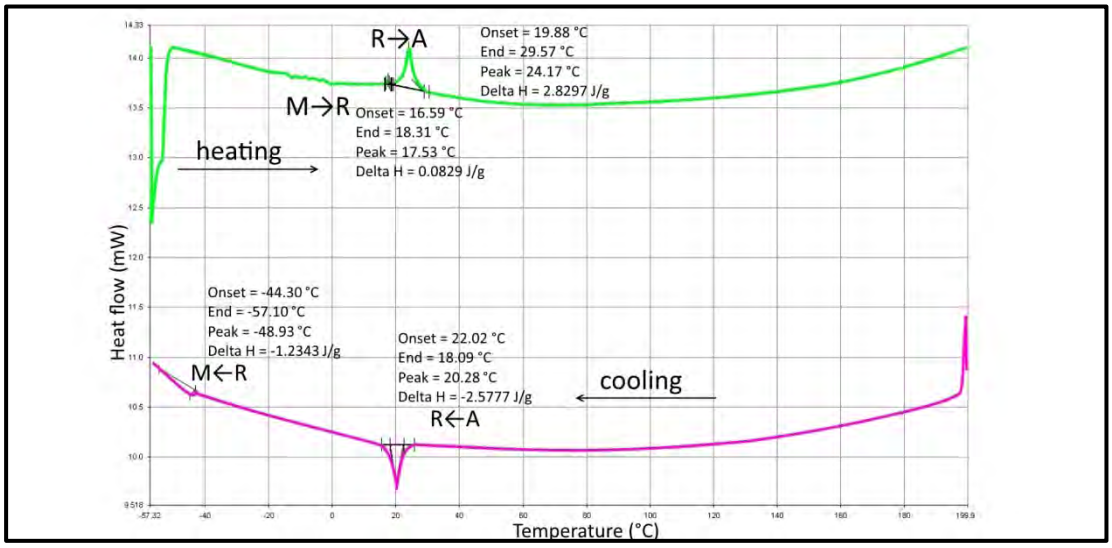

Figure 4-9: DSC for Nitinol wire aged at 450°C for 10min. Both heating and cooling steps revealed a two-phase transformation (Martensite → R-phase → Austenite) and (Austenite → R-phase → Martensite).

Martensite (M) to the intermediary rhomboedral phase called R-phase and then to austenite (A) transformation temperatures were captured during the heating step. Upon heating, the R-phase transformation temperature started at 16.59 °C and was finished at 18.31 °C, followed by austenite transformation starting at 19.88 °C (A_s) and finishing at 29.57 °C (A_f). In the cooling step, the transformation from austenite into the R-phase began at approximately 20 °C and was complete at 18 °C and then into martensite, transformation which began at -44.3 °C (M_s) and was finished at -57.10 °C (M_f). These transformation temperatures are later to be used in the calculation of the stress/temperature gradients required in calibrating the superelastic-plastic model for Nitinol (section 8.2.1). The DSC thermal analysis also enabled the calculation of the latent heat of transformation ΔH during heating and cooling. The enthalpies for each transformation were 0.0829J/g, 2.8297J/g, -2.5777J/g and -1.2343J/g for the R-phase during heating, austenite, R-phase during cooling and martensite respectively.

4.5.2 Uniaxial Tensile Test

The purpose of the uniaxial tensile test was to evaluate the material constants required in calibrating the FE material models. The loads and extensions were

converted into engineering stress and strain. The tensile test was performed at room temperature T_0 of 22 °C, which was between A_s and A_f, therefore it was expected to see the material behaving superelastically during the test. The tensile curve depicted in Figure 4-10 shows the stress–strain hysteresis loop, proving the superelastic behaviour of the Nitinol material.

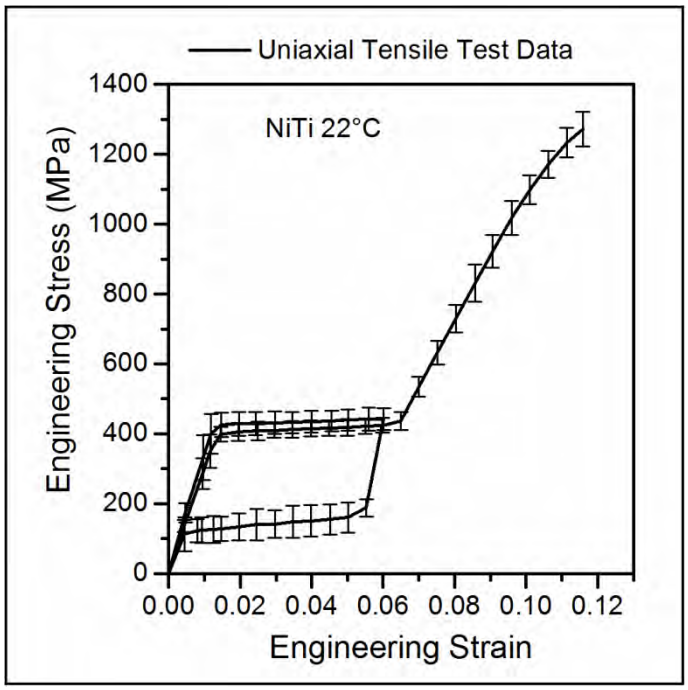

Figure 4-10: Engineering stress versus engineering strain plot for the Nitinol wire tested at room temperature. The material undertook linear elastic deformation until a critical stress was reached. The austenite transformed into martensite due to stress applied on the upper plateau up to a strain of 6%. On unloading, the volume fraction of martensite started to decrease along the lower plateau and at full unload, it returned elastically to zero strain. Error bars represent a single standard deviation from the mean (n=3).

The volume fraction of martensite increased along the upper plateau until 6% strain was achieved. Upon unloading, when the stress applied reached a value of ~ 170MPa, the volume fraction of martensite started to decrease along the lower plateau and at full unload, it returned elastically to zero strain. The material failed when pulled at ~11.5% strain and the mean ultimate tensile strength (UTS) was 1272.44 ± 49.71MPa. These results are close to the values provided by MatWeb (2016) for high-strength superelastic Nitinol alloy.

4.5.3 Braided Stent Radial Force

The radial force of the stent was evaluated experimentally during the radial compression test. The test also required to evaluate the fiction force residing in the crimping head. The results of the second cycle were used for the determination of the force-diameter curve. The force at the load cell with stent setup was converted into radial force (RF). The radial force measured without the stent (FF) accounting for the frictional effect in the setup was extracted from RF and lead to the evaluation of the adjusted radial force (ARF). Figure 4-11 depicts the adjusted radial forces of the Nitinol stent. Data distribution is represented by showing the mean values of the data, while the variability of data acquired from the three tested prototypes is indicated by the error bars representing a single standard deviation from the mean.

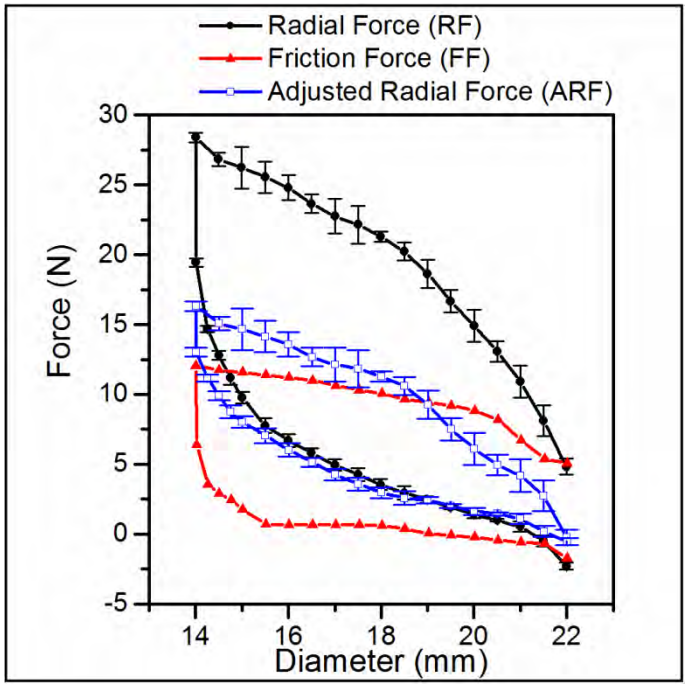

Figure 4-11: Nitinol stent radial force versus stent diameter evaluated experimentally during the radial compression test. The adjusted radial force (*ARF*) represents the radial force (*RF*) of the stent after subtracting the friction force (*FF*) within the crimping head. Error bars represent a single standard deviation from the mean (n=3).

Chapter 5
Finite Element Analysis

An accurate FE model is required to reliably predict the mechanical behaviour of braided stents when subjected to crimping. Commercial FE software packages e.g. Adina, Ansys, Abaqus, Comsol, Nastran have been employed in stent FEA and in most cases, due to its complexity, a geometrical model was created in advance on 3D CAD software, such as SolidWorks. Popular between researchers in the academia due to the wide material modelling capability, Abaqus is the commercial FEA software package used in this project because it enables the implementation of time-domain viscoelasticity by deriving the creep compliance function and stress relaxation function directly from experimental data.

5.1 Mechanical Constitutive Models in Abaqus

In this thesis, the stress analysis problem to be solved is the process of crimping/uncrimping of a braided stent fabricated from a number of materials such as: PDO, Nitinol and Phynox. For all these materials, Abaqus offers a range of constitutive equations to describe the material's behaviour. This section presents theoretical aspects of the following material models: linear elastic model, superelastic model and linear viscoelastic model.

5.1.1 Linear Elasticity

PDO, Nitinol and Phynox can be modelled as isotropic, rate independent, perfect elastic materials, with not temperature dependency. Linear elasticity is a simple

model which may suffice in circumstances when the stent is not subjected to severe loading. In this case, the mechanical response is purely elastic and the total strain ε contains only a recoverable, elastic part ε_{el} (Equation 5.1).

$$\varepsilon = \varepsilon_{el} \quad \textbf{Eq.5.1}$$

The total stress σ is defined as:

$$\sigma = D_{el}\varepsilon_{el} \quad \textbf{Eq.5.2}$$

where D_{el} is the fourth-order elasticity tensor.

For an isotropic material, the only mechanical properties required to define elasticity are the Young's modulus E and the Poisson's ratio ν.

5.1.2 Superelasticity

The crimping process may lead to plastic deformation particularly in the crowns of the stent, which could prevent full recovery of the stent after deployment. Therefore, a material model to predict a possible plastic deformation is required, to be able to account for its effects during the stent design process.

In Abaqus ver.6.14, the Nitinol superelastic-plastic model is implemented as a built-in user material and it is based on the superelastic constitutive model developed by Auricchio and Taylor (Auricchio and Taylor 1997; Auricchio *et al.* 1997). In their model, the strain ε is decomposed into a linear elastic component and a stress induced transformation component. The material is considered isotropic and only two phase transformations are included – conversion from austenite to martensite and from martensite to austenite. The superelastic-plastic model was developed as an extension to the superelastic version, by adding a plastic component (Equation 5.3) (Rebelo *et al.* 2003).

Depending on the analysis type, the model requires a number of material constants, some of which can are picked from the stress-strain curve following a uniaxial tensile test. A generic uniaxial behaviour of Nitinol and the material constants picked on the curve can be depicted in Figure 5-1. The analysis in the current study was performed in Abaqus/Standard, for which $15 + N_A$ constants are used in case of the superelastic implementation, or $16 + N_A + 2N_P$ constants are required in case of the superelastic-

plastic model; where N_A is the number of annealing to be performed and N_P is the stress-strain pairs required to define the yield curve.

The material constants are obtained by calibrating its behaviour based on test data acquired from a uniaxial tensile testing experiment. The parameters are temperature dependent and include elastic moduli in austenite and martensite phases, stresses which refer to the start and the end of the phase transformation during loading, unloading in tensile and compression.

$$\varepsilon = \varepsilon_{el} + \varepsilon_{tr} + \varepsilon_{pl} \qquad \textbf{Eq.5.3}$$

where ε_{el} is the linear elastic component of the strain, ε_{tr} is the transformation component and ε_{pl} is the plastic strain.

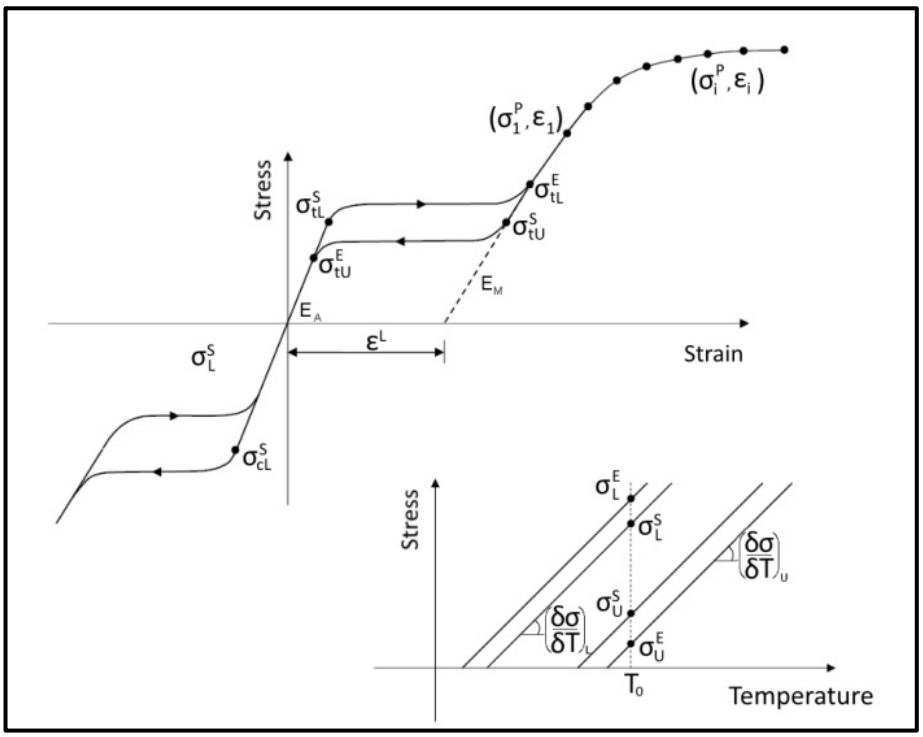

Figure 5-1: Generic uniaxial behaviour of Nitinol with some of the material constants used in the Abaqus superelastic-plastic model depicted on the stress-strain curve: T_0 reference temperature, ε^L transformation strain, E_A and E_M austenite and martensite elastic modulus, start and end of the stresses on the loading and unloading path in tensile and compression, $\sigma_i^P, \varepsilon_i$ stress and strain pairs of plastic points and stress-temperature gradients $\left(\frac{\delta\sigma}{\delta T}\right)$ on the loading and unloading paths (adapted from Abaqus 2004).

5.1.3 Linear Viscoelasticity

Linear viscoelastic material models can be conceptually built using a combination of mechanical elements such as elastic springs and viscous dash points, the higher complexity, the better fit with the actual mechanical behaviour. In this section, it is emphasised the development of a material model without using these elements. Instead, Abaqus' method was used, which makes use of the hereditary integrals (Abaqus Inc 2014). The creep compliance function or stress relaxation function required for describing the viscoelastic behaviour is derived based on the experimental data gathered.

If the specimen is considered under a state of tension in which an infinite number of loads of an infinitesimal magnitude is applied, the constitutive equation for a linear viscoelastic material is given by the hereditary integral:

$$\varepsilon(t) = \sigma_0 D(t) + \int_0^t D(t-s)\dot{\sigma}(s)ds \qquad \textbf{Eq.5.4}$$

where ε(t) is the time-dependent strain and D(t) is the tensile creep compliance.

From Equation 5.4, the corresponding hereditary integral in terms of the stress relaxation modulus can also be derived:

$$\sigma(t) = \varepsilon_0 E(t) + \int_0^t E(t-s)\dot{\varepsilon}(s)ds \qquad \textbf{Eq.5.5}$$

where σ(t) is the time-dependent tensile stress and $E(t)$ is the time-dependent tensile modulus.

If instead of a tensile test, a shear test is performed, the hereditary integral (Eq 5.4) in terms of shear creep compliance J is given by equation:

$$\tau(t) = \tau_0 J(t) + \int_0^t J(t-s)\dot{\tau}(s)ds \qquad \textbf{Eq.5.6}$$

Written in terms of the shear modulus, Equation 5.5 becomes:

$$\tau(t) = \gamma_0 G(t) + \int_0^t G(t-s)\dot{\gamma}(s)ds \qquad \textbf{Eq.5.7}$$

where $\tau(t)$ is the time-dependent shear stress and $G(t)$ is the time-dependent shear relaxation modulus.

The shear relaxation modulus $G(t)$ from Equation 5.7 can be written as a Prony series:

$$G(t) = G_\infty + \sum_{i=1}^{N} G_i e^{(-t/\psi_i)} \qquad \textbf{Eq.5.8}$$

where G_∞ is the long-term shear modulus and ψ_i is the relaxation time. By substituting $t = 0$, the initial moment the shear relaxation modulus is given by:

$$G(t=0) = G_0 = G_\infty + \sum_{i=1}^{N} G_i \qquad \textbf{Eq.5.9}$$

From Equation 5.8 and 5.9, the Prony series can be rewriten in the following form:

$$G(t) = G_0 - \sum_{i=1}^{N} G_i\left[1 - e^{(-t/\psi_i)}\right] \qquad \textbf{Eq.5.10}$$

Abaqus uses a normalised shear relaxation modulus $g(t)$, which can be obtain by dividing the shear relaxation modulus $G(t)$ by the instantaneous shear modulus G_0:

$$g(t) = 1 - \sum_{i=1}^{N} g_i\left[1 - e^{(-t/\psi_i)}\right] \qquad \textbf{Eq.5.11}$$

where N(number of terms in the series), g_i (normalised shear relaxation modulus at term i) and ψ_i (relaxation time at term i) are material constants.

Abaqus deducts the creep or relaxation parameters by computing the terms in the Prony series from a given set of normalised shear relaxation moduli or shear creep compliance data.

Three steps are required for creating and calibrating the linear viscoelastic material model in Abaqus:

1. First step is defining the elastic behaviour part of the material definition: in the Abaqus material editor, select "Elastic" from the elasticity behaviours under the "Mechanical" menu and input the value for the instantaneous elastic modulus determined.
2. The second step is adding the "Viscoelastic" behaviour in time domain by including the creep test data. Abaqus requires input of data from a shear creep test, and/or volumetric test. Since the creep experiment performed was a tensile creep test, a conversion of data from tensile to shear is required. Generally, shear modulus G for a homogenous isotropic material written in terms of elastic modulus E and Poisson ration ν is given by:

$$G = \frac{E}{2(1+\nu)} \qquad \textbf{Eq.5.12}$$

Using a similar relationship between compliances instead of moduli (Alger 1996) and considering PDO an isotropic material with a Poisson's ratio $\nu = 0.45$ (Peirlinck 2013), Equation 5.12 can be reformulated taking into account the polymer's time dependency (Equation 5.13). Similarly, in the case of Nitinol isotropic material with a Poisson's ratio $\nu = 0.33$ (De Beule 2008).

PDO $$J(t) = 2.9\frac{\varepsilon(t)}{\sigma_0} \qquad \textbf{Eq.5.13}$$

Nitinol $$J(t) = 2.66\frac{\varepsilon(t)}{\sigma_0}$$

Equation 5.13 was subsequently used to compute the shear creep compliance based on the raw tensile creep data, and the normalised data for each time reading was input to Abaqus material interface.

3. The last step is to “Evaluate” the material model. This functionality is a convenient way that Abaqus offers in order to view the predicted behaviour for the viscoelastic material. Abaqus performs standard tests on the material model defined. A nonlinear least-squares fit of the creep data to a Prony series is executed to determine the coefficients and the relaxation periods. A maximum order of 2 is used for fitting the Prony series. The test results are presented as shear creep compliance and stress relaxation versus time plots. Prony series terms representing the material parameters for the viscoelastic response are slotted into Equation 5.11 to obtain the time-dependent normalised shear relaxation modulus curve.

5.2 Braided Stent Model

The number of studies focusing on braided SX stents is limited, probably due to the fact that classical CAD software packages do not provide a particular methodology to deal with the complexity of 3D braided structures.

Researchers from Ghent University in Belgium have developed an application called pyFormex and the Biomechanical Engineering research cluster in Ghent University was the first to use it for generating 3D models for the braided wire stent (Conti 2007; De Beule 2008; Mortier 2010; Peirlinck 2013). pyFormex is an open-source software capable of creating large sets of coordinates based on mathematical transformations gathered inside a Python script. Its initial purpose was for generating complex 3D structures with geometry obtained from mathematical equations, typically covering wireframe type structures (Verhegghe 2013).

Kim *et al.* (2008, 2010) created the geometrical models for the wires stents with the help of a pre-processor program in C# programming language by considering the motion of the wire carrier during the braiding process.

Zhao *et al.* (2012) used Abaqus to create the braided stent model. Zhao *et al.* (2013)and Ni *et al.* (2014) generated the braid geometry in Ansys. The algorithm was coded in Ansys Parameter Design Language. A spiral curve was determined first and the entire model was achieved by copying and reflecting the spiral curve in a

cylindrical coordinate system, where Z-axis is set in the axial direction, X-axis in the radial direction and Y-axis is set in the circumferential direction.

In the current research, a combination of pyFormex and Abaqus ver. 6.14 was used to generate the geometry and the discretisation of the braided stent, while the element type selection, material modelling, simulation and postprocessing was entirely done in Abaqus ver. 6.14. Figure 5-2 depicts the methodology used in the braided stent FEA.

pyFormex is available as an open-source project and it can be used and modified under GNU General Public Licence (GPL). The software is built upon Formex algebra and requires setting up a Linux environment. A Python script for building the 3D geometry for a basic open ended cylindrical braided stent is available in pyFormex.

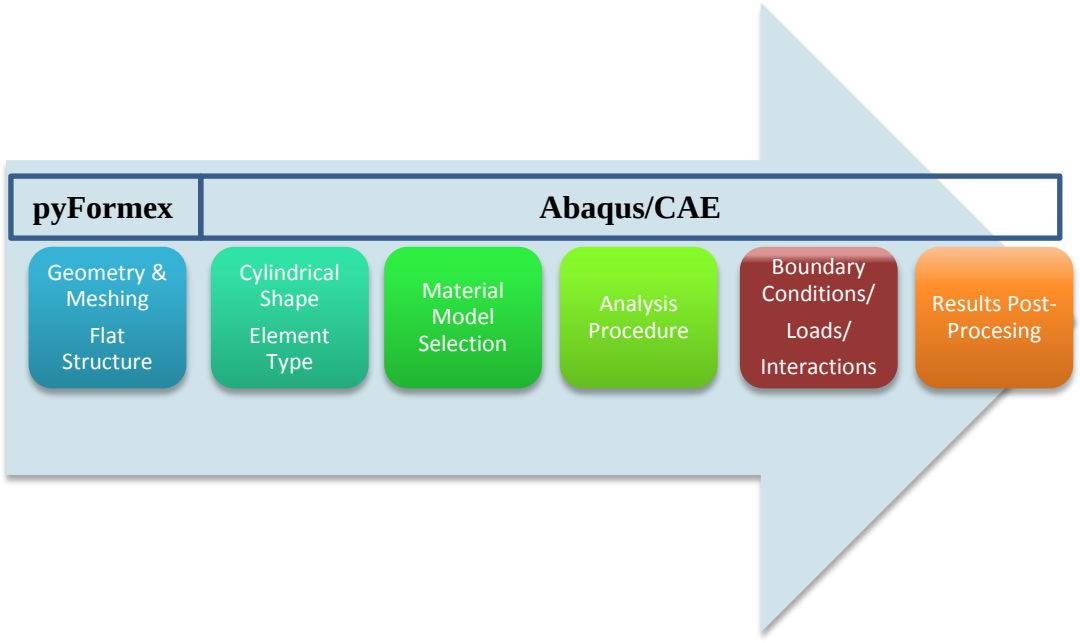

Figure 5-2: SX Braided stent modelling workflow.

Development of the 3D braided stent geometry with crowns

1. The first step in the development of the 3D geometry consisted in using pyFormex to create a flat braided meshed structure (Section 5.2.1). The geometry, containing the coordinates of all nodes and discretised elements was exported as an .inp file.

2. Next, the .inp file was imported in Abaqus. The distance between adjacent wires in the radial direction was deducted and a new part was built to resemble the crown. A set of 15 crowns was assembled and merged to the braid part at both ends of the flat structure.
3. The assembly was rolled into a cylindrical shape using Abaqus plugin called wrapMesh and the adjacent nodes on the helical curved edges were merged to create a unit structure.

5.2.1 Development of the Flat Braided Structure in pyFormex

"BraidedStent.py" script was developed based on the "WireStent.py" demo file. Some of the main important parts of the Python script are explained in this chapter, while the full script can be viewed in Appendix 2.

The geometry of the braid is defined by the following parameters required in the DoubleHelixStent Class constructor: length of the stent, diameter of the stent, wire diameter, pitch and number of wires.

```
42 class DoubleHelixStent(object):
43     """Constructs a double helix braided stent.
...
48     The geometry is defined by the following parameters:
49       L  : approximate length of the stent
50       De : external diameter of the stent
51       D  : average stent diameter
52       d  : wire diameter
53       be : pitch angle (degrees)
54       p  : pitch
55       nx : number of wires in one spiral set
56       ny : number of modules in axial direction
57       ds : extra distance between the wires
59       dz : maximal distance of wire centre to average cylinder
60       nb : number of elements in a strut, default 4
```

Other variables, such as the number of elements in the wire required in discretisation, connector elements at the position where two wires cross each other, distance between wires if required, are created and assigned values.

The main steps required in creating the .inp file for the flat braided structure are:

1. Create a base module from two crossing wires based on the stent geometry parameters input in the constructor of the DoubleHelixStent Class. This step starts with creating a wire as a straight strut and then creating a bump in the middle of the strut.

```
69      def
__init__(self,De,L,d,nx,be,ds=0.0,nb=4,connectors=True):
70          """Create the Braided Stent."""
71          D = De - 2*d - ds
72          r = 0.5*D
73          dz = 0.5*(ds+d)
74          p = pi*D*tand(be)
75          nx = int(nx)
76          ny = int(round(nx*L/p))
77          # a single bumped strut, oriented along the x-axis
78          bump_z=lambda x: 1.-(x/nb)**2
79          base =
Formex('l:1').replic(nb,1.0).bump1(2,[0.,0.,dz],bump_z,0)
```

The process continues with creating a second strut by mirroring the first one. The second strut needs to be reflected, rotated and translated such that it is positioned crisscross in comparison to the first strut (Figure 5-3a).

```
80          # scale back to size 1.
81          base = base.scale([1./nb,1./nb,1.])
82
83          # create bended strut (stent ends)
84          BS = base.mirror(0).translate(0,-1.).setProp(4)
85          BS += BS.rotate(180.,2).reflect(2)
86          BS = BS.translate(1,-
sqrt(2.)).cylindrical([1,0,2],[1.,90./4,0.5]).rotate(90.,2).tra
nslate(0,2.)
87
88          # NE and SE directed struts
89          NE = base.shear(1,0,1.)
90          SE = base.reflect(2).shear(1,0,-1.)
91          NE.setProp(1)
92          SE.setProp(3)
93          # a unit cell of crossing struts
94          cell1 = (NE+SE).rosette(2,180)
95          # add a connector between first points of NE and SE
96          if connectors:
97              cell1 += Formex([[NE[0][0],SE[0][0]]],2)
```

2. The second step consists in creating the extended base module which involve creating a second base module by mirroring the first one and connecting the two modules in order to obtain the 1 under 1 over pattern of the braid (Figure 5-3b).

```
98          # create its mirror
99          cell2 = cell1.reflect(2).translate([2.,2.,0.])
100         base = cell1 + cell2
101
102         # reposition to base to origin [0,0]
103         base = base.translate(-base.bbox()[0])
```

3. The third step is creating the flat pattern at the dimensions required for the finished braid (Figure 5-3c).

```
105         # Create the full pattern by replication
106         dx,dy = base.bbox()[1][:2]
107         F = base.replic2(nx,ny,dx,dy)
```

4. Next step is meshing the structure. 4 elements were considered for each wire-based building block and a connector element to model the contact between two crossing wires.

```
127         M = self.F.toMesh()
```

5. Last step consists in exporting the mesh into an inp file by using pyFormex plugin fe_abq.

```
164     from plugins.fe_abq import exportMesh
165     M = H.getFormex().toMesh()
166     exportMesh('FlatStent.inp', M, eltype='B31')
```

The major advantage in using pyFormex for creating braid geometry is its capability of generating a multitude of variations from within a single Python file, by using different parameters values in the constructor.

The geometrical model of the braided stent was subsequently imported in Abaqus. The distance between adjacent wires in the radial direction was deducted and a new part was built to resemble the crown. The crown was meshed using 4 elements. A set of 15 crowns were assembled and merged to the braid part at both ends of the flat structure.

The assembly was rolled into a cylindrical shape using Abaqus plugin called wrapMesh and the adjacent nodes on the helical curved edges were merged to create a unit structure.

Hall and Kasper (2006) have investigated the computational efficiency of various choices of element dimensions and formulations used in the discretization of stents, such as C3D8 (8-node linear hexahedral solid elements), S4 (4-node linear quadrilateral shell elements) and B31 (2-node linear beam in space, shear-flexible).

They concluded that employing beam elements in conjunction with contact surfaces leads to an accuracy of the results similar to the predictions when employing solid continuum elements, with the great advantage that in terms of computational efficiency, it is the most efficient methodology.

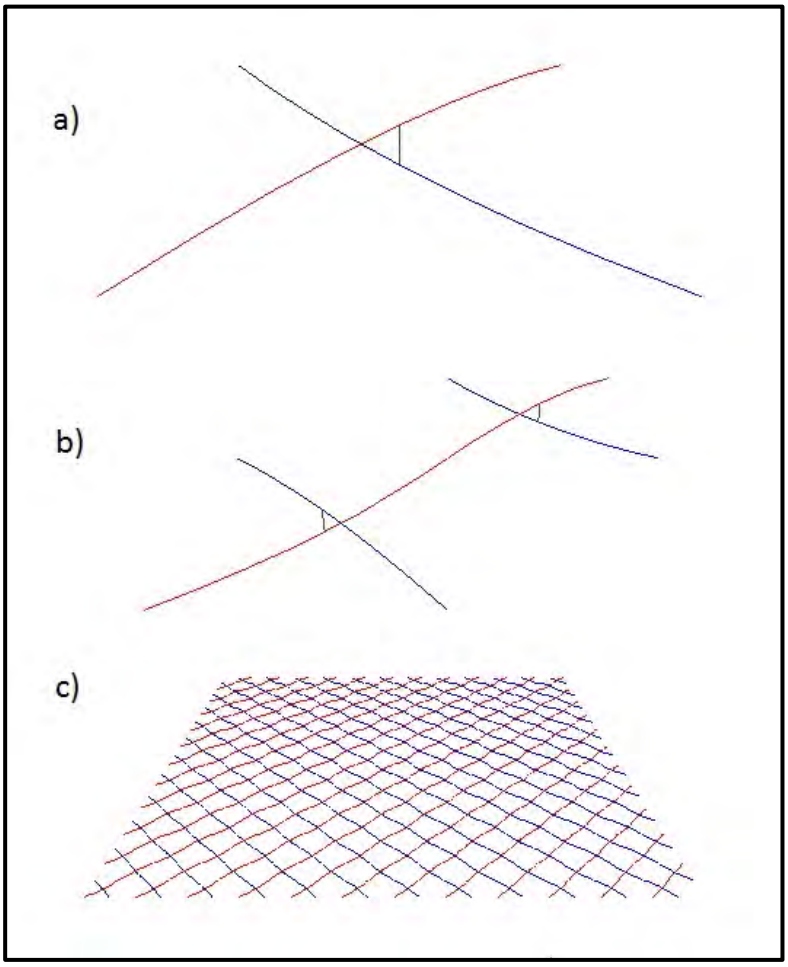

Figure 5-3: 3 steps are required for building the flat braided structure in pyFormex. a) The base module is created from two crossing wires b) An extended module is created by mirroring the base module and connecting the two modules c) The flat pattern is built at the dimensions required for the finished braid.

With the purpose of creating an accurate and efficient tool for predicting the mechanical behaviour of the braided stent subjected to crimping, the strategy adopted in this study was to use B31 elements in the discretization of the braided stent. The beam elements are applicable when modelling a wire structure because the dimension of the cross section is much smaller when comparing to the axial direction. The wire was modelled as a beam with a solid circular cross-section determined by the round profile of the wire. B31 elements, also called Timoshenko

beams use advance beam theories also accounting for transverse shear deformations. B32 quadratic beam elements are used in parallel with B31 elements in the discretization of the stent's wire in Chapter 6 and Chapter 8, to analyse the impact to the FE predictions when using linear versus quadratic interpolation functions.

Following a mesh sensitivity analysis, Peirlinck (2013) concluded that a number of 2 or 4 elements in a strut assigned to the nb parameter in the constructor of the DoubleHelixStent Class leads to acceptable results, where the strut is between two consecutive wire intersections. In this thesis, the number of elements in a strut was set to 4.

5.2.2 Polymeric Stent Model

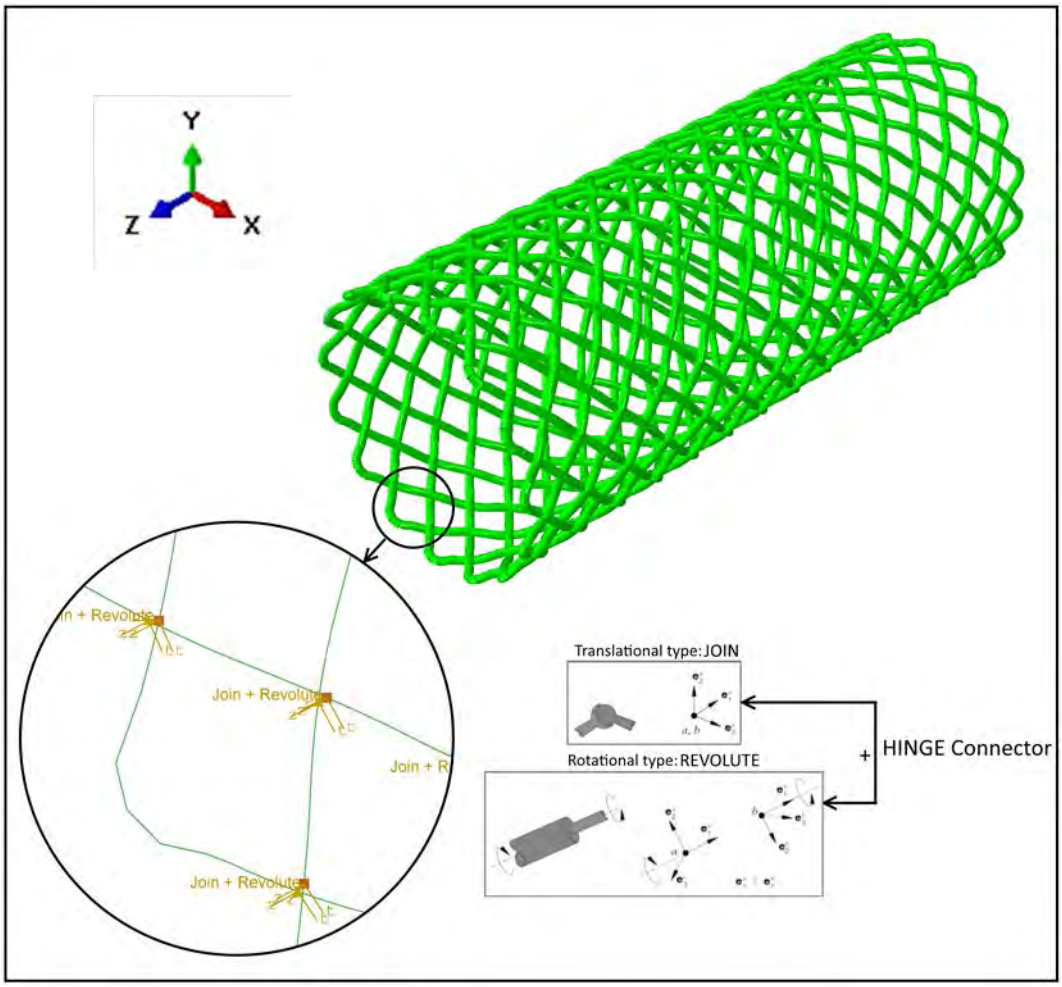

Figure 5-4: Polymeric braided stent geometrical model developed in pyFormex. Connector elements Join + Revolute can be observed in the closeup.

The polymeric stent geometry is defined by length 54 mm, diameter 22 mm, wire diameter 0.62 mm, number crowns 15 and pitch angle 40° (Figure 5-4).

6900 2-node linear beam elements B31 were used for meshing the polymer wire and 420 HINGE connectors. The HINGE connector element was chosen to model the contact between two crossing wires, constraining the sliding movement of both nodes on the crossing wires while rotational degrees of freedom are free. This configuration enables the change in the pitch angle during crimping. The HINGE connector is created from two basic connections: a translation connection called JOIN, which joins the position of the two opposing nodes at the wires intersection and a rotational basic connector called REVOLUTE, which enables a revolute connection between their rotational degrees of freedom.

5.2.3 Metallic Stent Model

The Nitinol stent prototypes were fabricated under the same geometrical specification as the polymeric ones, therefore the geometrical model of the Nitinol/Phynox stent was based on the polymeric version, the main difference being the choice of connector elements and the wire diameter. The mechanical relationship between the two opposing points at the intersections between the wires was modelled using connector elements CONN3D2 - HINGE type. This type of connector joins the positions of the two opposing nodes and provides a revolute connection between them. The wire intersections located at the extremities of the stent were modelled using CONN3D2 - SLIDE-PLANE type, to allow sliding and repositioning of the crowns to conform to the reduced diameter of the crimper. A node set was created from the outer nodes of the stent to use in modelling the contact. A second node set was created for a node situated in the middle of the stent to fixate the stent during the crimping simulation.

5.3 Crimper Model

In the existing SX FEA literature, two main strategies in modelling the crimping tool are employed: first strategy is modelling the tool as individual rigid plates positioned radially around the stent to resemble the segments of the crimping head (McGrath *et al.* 2016); second strategy is modelling the tool as a tubular rigid part with a circular cross-section or a convex, regular polygonal cross-section (De Beule 2008; Ma *et al.* 2012; Peirlinck 2013). Alternatively, a simplified cylindrical model can also be employed to perform the radial compression.

5.3.1 8 Plates Crimper (8PC)

The tool is modelled as 8 rigid plates placed in an octagonal formation distributed circumferentially around the stent geometry, each plate being meshed with 20 discrete rigid elements R3D4 (Figure 5-5).

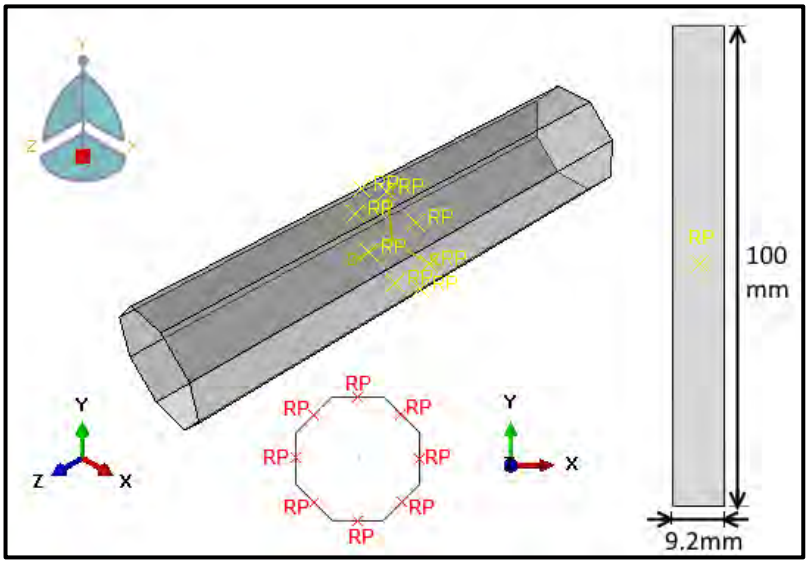

Figure 5-5: 8 Plates Crimper created by positioning 8 individual rectangular shape rigid plates in an octagonal formation around the stent. RP represent reference points positioned in the centre of symmetry of each plate.

5.3.2 Octagonal Crimper

The tool is modelled as a tubular 3D deformable shell with an octagonal section (Figure 5-6). The part is seeded so that each face of the octagon has one element and the reduced-integration surface element type (SFM3D4R) is assigned.

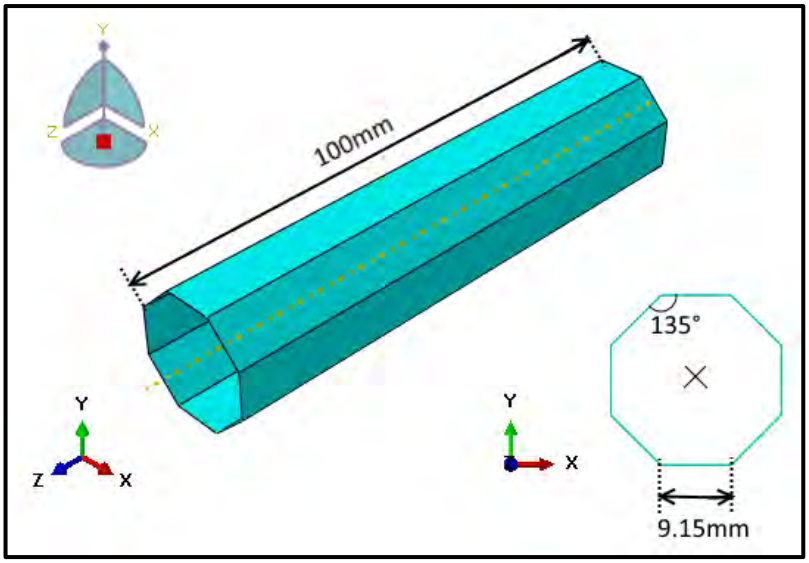

Figure 5-6: Octagonal Crimper presented in the isometric and front views. The model geometry was created as a 3D deformable shell with a regular octagon section.

5.3.3 Cylindrical Crimper

The crimper geometry is modelled as a 3D deformable cylindrical shell and meshed using 4-node quadrilateral surface elements with reduced integration (SFM3D4R). The part was seeded with global element size of 0.1 mm, while only one element was used along its length. The inner surface of the crimper is specified to enable the contact modelling.

5.4 Contact Modelling

The initial modelling strategy was to implement a general contact interaction. This method has the advantage that it is easy to define even for complex topologies and can be defined automatically for both rigid and deformable bodies. General contact algorithm was successfully implemented in the stent-8PC model, with interaction defined between selected surfaces: the circumferential surface of the wires and the inner surface of the plates.

The method was not accessible in the stent-OC model due to the choice of underlying elements, therefore a surface-to-surface contact was chosen, with interaction defined between the inner face of the octagon as master surface and a node set formed by the outer nodes of the stent as slave. The finite sliding formulation was chosen for both crimper models because of its robustness and the ability to continuously update the interaction points in relation to the master surface. The disadvantage in using this method was that creating the subset of nodes is a tedious, lengthy process. In terms of friction formulation, the strategy was to use the penalty method because of better solver performance and improved convergence rates. The disadvantage was that a small amount of penetration occurred and the penalty stiffness had to be adjusted rather than using the default Abaqus setting.

In case of the cylindrical crimper, a frictionless surface-to-surface contact was defined between the inner face of the crimping tube and the node set formed by the outer nodes of the stent.

5.5 Stent Crimping Simulation

The stent crimping simulation is a challenging non-linear quasi-static problem involving complex contact conditions. Due to the difficulties in achieving convergence when using the implicit scheme, Abaqus/Explicit is being favoured as a solver in the existing SX FEA literature. Generally, Abaqus/Standard leads to more accurate solutions when solving quasi-static problems, because it involves modelling the process in its natural time period. Therefore, in this research, the strategy is to use the implicit analysis (Abaqus/Standard) and identify the successful combinations of solver controls and contact formulations that would lead to accurate solutions without an impact on the solution cost.

In the SX FEA literature, the crimping/uncrimping simulation is always done in a single analysis step using smooth amplitude in order to apply the load or to achieve the boundary condition of radial displacement. In this research, a 1-step and 2-step analyses were implemented and tested in order to identify the framework leading to the most accurate FE implementation.

A displacement driven simulation strategy is considered and radial forces are derived from the reaction forces opposing the imposed radial displacements. The stent deforms by imposing a specified displacement Boundary Condition (BC) to the crimper model. A displacement BC is imposed on the crimper model to restrict rotation and axial movement. A displacement BC is applied to the node in the middle of the stent model to avoid rotation and axial movement in this region.

Chapter 6, 7 and 8 describe in detail the simulation strategy for the particular cases that are presented.

Chapter 6
Looped Ends versus Open Ends Braided Stent

The present chapter has two major purposes: firstly, to investigate whether the analytical model for assessing the mechanical behaviour of an open ends metallic braided stent described in Chapter 3 is applicable to the looped ends stent design and secondly, to compare the response of the two stent designs subjected to radial compression. FEA is used to evaluate the performance of the two braided stents emulating well established designs: WALLSTENT and WallFlex. WALLSTENT model is initially validated analytically. A radial crimping simulation is performed and the radial forces and stresses induced are evaluated for the two stent designs.

6.1 Introduction

The term stent, as currently used in the medical devices industry, was introduced with the advent of Wallstent, an open ends, braided self-expanding metallic prosthesis invented in the 1980's (Rousseau *et al.* 1987; Wallsten 1987; Wallsten and Imbert 1991). The design quickly became a massive success and its applicability spread from its initial use as a coronary stent to treating peripheral arterial disease and gastrointestinal tract disorders.

30 years later, the initial design is still the benchmark, with current applications in both vascular and nonvascular interventions. However, in the gastrointestinal tract

applications, the design evolved. Some of the improvements are: the addition of a polymeric coating to prevent tumour ingrowth, the use of other alloys to improve flexibility and visibility during the testing procedure and ultimately the geometry evolved by replacing the open ends style with a looped and flared ends version in the attempt to reduce the risk of tissue trauma and prevent stent migration.

6.2 Fabrication

Braided stents are small diameter tubular structures consisting of two sets of interlacing, spiralling strands, one set clockwise and the other anti-clockwise direction, both lying on the bias relative to the longitudinal axis of the braid. They can be manufactured on custom-made braiding machines, Boston Scientific's WALLSTENT and WallFlex being some examples.

WALLSTENT is fabricated by interlacing a set of wires in a continuous tube geometry from which the individual stents are cut to specification, leaving the ends of the wires exposed, therefore the "open ends" name of the design. WallFlex also features a multi-wire design, however, on both ends of the stent there are closed loops (at one end the wires being bonded with the help of laser fusing technology) which gives the design the name "looped ends". Braided stents can also be fabricated manually using a single piece of wire. The seamless design enables crown forming at the extremities of the stent and can be produced on cylindrical or stepped mandrels. Examples are Cook's Evolution Nitinol stent and Ella CS's SX-Ella Esophageal BD PDO stent. The braided stents are produced in the expanded dimensions, followed by electropolishing in order to remove the oxides formed during the manufacturing process (De Scheerder *et al.* 1998). Braided stents provide excellent coverage and flexibility; however, they shorten substantially after expansion.

The trend in stent design is minimal thickness of the struts, therefore, when the thickness of the wire or struts cannot be increased to facilitate visibility, the radiopacity issue is addressed by attaching radiopaque markers made from materials with higher atomic weight (e.g. tantalum, gold, platinum) at both ends of the stent, which is the case of WALLSTENT. Another way is to use an alloy with a higher visibility and in case of some of the WallFlex stents, the use of Platinol (a Nitinol wire with a Platinum core), delivering enhanced full-length radiopacity. Certain

conditions where there is a discontinuity in the lumen, such as a rupture or fistula, remain a problem in interventional therapy. A solution to this problem is to apply a polymer material such as silicone to the stent surface as a coating. The addition of the coating reduces tissue hyperplasia and the risk of thrombosis and enables stent removal if repositioning or a temporary placement is required. SX braided stents designed for esophageal, biliary and colonic applications are available partially and fully covered. An example is: 'WallFlex Billiary' (Boston Scientific), where the stent is covered with a silicone coating.

6.3 FEA of Braided Stents

This section presents a concise 10 year review of the state-of-the-art investigations in the mechanical behaviour of braided stents using numerical methods with a focus on the development of the FE material models and the geometry of the stent.

In 2007, Zahora et al. were the first to investigate FE modelling of a braided stent and simulated axial deformation in Comsol (Záhora *et al.* 2007). A simplified model of the Nitinol braided structure was created, where the wires were modelled as a set of non-interacting spirals. An elastic model was chosen for the Nitinol material and the stress distribution was investigated for two geometrical models – an "unwelded" version, where the wires overlap and a "welded" version, where the wire intersections are welded. Conti created the first interlaced braided stent model with open ends and simulated stent deployment in an artery (Conti 2007). pyFormex, which is a Python based scripting language used for the generation of complex 3D geometries by means of mathematical equations, was used in modelling the geometry and meshing, while Abaqus was used in the analysis. Conti validated the braided stent model using an analytical model developed by Jedwab and Clerk and validated experimentally (Jedwab and Clerc 1993).

Building on Conti's work, De Beule analysed the "Urolume" open ends braided stent behaviour during axial elongation and radial compression (De Beule *et al.* 2007; De Beule 2008). The FE models were validated using the analytical model and experimental results reported by Jedwab and Clerc (Jedwab and Clerc 1993) and Wang and Ravi-Chandar (Wang and Ravi-Chandar 2004). The material model implemented for Nitinol covered only its superelastic behaviour and was developed

using a User Defined Material Model subroutine (UMAT), while for Elgiloy and stainless steel stents, a linear elastic model was used. The numerical simulations of free expansion provided a good representation of the deformability for the Nitinol and Elgiloy stents, however, the behaviour of the stent was compromised by the effect of plastic deformation in the case of the stainless steel stent.

Kim et al. developed an experimentally validated model to simulate the mechanical performance of SX Nitinol braided stents during compression and bending, based on sample stents created on a braiding machine built in the laboratory (Kim *et al.* 2008). Geometrical models for the open ends wire stents were created with the help of a pre-processor program in C# programming language by considering the motion of the wire carrier during the braiding process. Kim et al. modelled the Nitinol material as a VUMAT in Abaqus/Explicit, covering its super-elastic effect.

In 2009, De Beule et al. presented a virtual stent design platform combining pyFormex and Abaqus, applicable to both BX and SX stents (De Beule, Mortier, *et al.* 2009). A strategy for design optimisation of SX braided stents was also presented (De Beule, Van Cauter, *et al.* 2009).

Kim et al. investigated the feasibility of developing SX braided stents using shape memory polyurethane fibre in 2010. The material model included its thermal-induced shape memory behaviour and was used it in conjunction with a braided stent model to analyse the deployment process (Kim *et al.* 2010)**.** Two different designs were modelled – open ends and welded ends and the effect of this design feature on the compression behaviour was investigated. It was concluded that the welding of the fibre ends increases the stiffness and structural stability of the braided stents, in particular for short stents.

In 2011, Auricchio et al. used FEA to evaluate the performance of three SX stent designs (including an open ends braided stent), in a patient-specific CA model based on computed angiography tomography (CTA) images. Three measures of the stenting impact on the vessel were considered: the stress induced to the vessel wall, the lumen gain and the vessel straightening.

In 2012, Zhao et al. evaluated the effect of fabrication technique on mechanical behaviour of stents by conducting FEA on two types of wire stents: an open ends

braided stent and a wire stent where the intersections are welded (Zhao *et al.* 2012). The geometrical models of the stents were created with Abaqus/Explicit and a user defined material model for Nitinol was developed (VUMAT subroutine) to outline the stress induced transformation between austenite and martensite. Crimping into a sheath followed by deployment into a stenotic artery was simulated. Higher stiffness was attributed to the welded stent with higher stress imparted to the vessel wall, in comparison to the open ends braided stent.

Zhao et al. conducted FEA on two looped ends braided esophageal stents: cup-spherical and straight-shaped (Zhao *et al.* 2013) in 2013. Stress and axial elongation of the stents were compared while changing parameters such as number of wires, wire diameter and length. The stents were modelled using APDL (ANSYS Parameter Design Language) and were meshed using 3D beam elements. A Nitinol material model covering its superelastic behaviour was used. Peirlinck performed FEA of polymeric braided stents in 2013. His work consisted of developing a numerical framework to simulate the deployment and expansion of biodegradable looped ends esophageal stents (Peirlinck 2013). The geometrical model of the stent was developed in pyFormex, while the analysis was done in Abaqus/Explicit, where a linear elastic material model was used and a steric interaction and friction between the wires was implemented. A degradation study for the biodegradable 'SX-Ella' stent was developed an incorporated in the FE model. The deployment of the polymeric braided stent within an esophagus was simulated and the results provided knowledge on the stent's ability to open a tortuous esophageal lumen.

In 2014, Frost et al. performed an experimental and theoretical investigation of the mechanical response for a looped ends braided stent in order to estimate fatigue properties of the stent during cyclic compression loading (Frost *et al.* 2014). Abaqus/Standard was used in FE computations. Frost et al. employed a rate-independent constitutive model for Nitinol, where R-phase transition was addressed (Sedlák *et al.* 2012). The looped ends were confirmed to be the critical areas with respect to fatigue life performance. FE simulation provided a reliable estimate for the outer pressure-stent diameter relation. Ni et al. investigated the effect of geometrical parameters of a braided stent on its mechanical properties (Ni *et al.* 2014). Radial stiffness, axial elongation and bending deflection were studied when design

parameters such as the number of looped ends, wire diameter and the pitch of wire were changed.

Yuan et al. used FEA to evaluate the mechanical properties of Polypropylene braided stents with a silicone coating and flared ends in 2016 (Yuan *et al.* 2016). Abaqus was used in the stent analysis and the stent compression experiment used to acquire the radial force was simulated as a displacement driven deformation performed by a rigid cube placed in the middle of the stent.

6.4 Methodology

The aim of this section is to use FEA to evaluate the mechanical behaviour of the two SX braided stents – the open ends versus the looped ends designs. The FE models are validated with the analytical model presented in Chapter 3. This theoretical model was built upon an experimentally validated model developed by Jedwab and Clerc (1993).

The methodology consists of:

1. Generating the two braided stent models;
2. Performing radial compression simulation on the open ends stent model and validating the FE model using the analytical model presented in Section 3.1;
3. Performing radial compression simulation on the looped ends stent model and comparing the simulation results of the two models to evaluate their mechanical performance.

6.4.1 Analytical Model

Section 3.1 presented the computation of all the parameters of the braid geometry and its mechanical properties. Table 8 presents the formulae required for computing the geometry of the braid.

Table 8: Analytical model for computing the geometry of an open ends braid.

BRAID GEOMETRY	OPEN ENDS BRAID FORMULAE	
EXTERNAL DIAMETER D_e	$D_e = D + 2d$	Eq. 6.1
AVERAGE DIAMETER D	$D = D_0 \frac{\sin \alpha}{\sin \alpha_0}$	Eq. 6.2

INITIAL HELICAL PITCH p_0	$p_0 = \frac{\pi D_0}{\tan \alpha_0}$	Eq. 6.3
NUMBER OF TURNS t_h	$t_h = \frac{L_0}{p_0} = \frac{L}{p}$	Eq. 6.4
INITIAL BRAIDING ANGLE α_0	$\alpha_0 = \tan^{-1}\left(\frac{\pi D_0}{p_0}\right)$	Eq. 6.5
BRAIDING ANGLE α	$\alpha = \tan^{-1}\left(\frac{\pi D}{p}\right)$	Eq. 6.6
INITIAL BRAID LENGTH L_0	$L_0 = \pi D_0 t_h \cot \alpha_0$	Eq. 6.7
BRAID LENGTH L	$L = \pi D t_h \cot \alpha = L_0 \frac{\cos \alpha}{\cos \alpha_0}$	Eq. 6.8
LENGTH OF WIRE IN HELIX L_{helix}	$L_{helix} = \frac{\pi D}{\sin \alpha} = \frac{\pi D_0}{\sin \alpha_0}$	Eq. 6.9
AXIAL ELONGATION δ	$\delta = t_h L_{helix}(\cos \alpha - \cos \alpha_0)$	Eq. 6.10
LENGTH OF WIRE IN STENT L_w	$L_w = n t_h L_{helix}$	Eq. 6.11
COVER FACTOR C	$C = 1 - \left[1 - \frac{nd}{L_{helix} \sin 2\alpha}\right]^2$	Eq. 6.12
JAMMED ANGLE α_j	$\alpha_j = \frac{1}{2}\sin^{-1}\left(\frac{nd \sin \alpha_0}{\pi D_0}\right)$	Eq. 6.13
JAMMED DIAMETER D_j	$D_j = \frac{nd}{2\pi \cos \alpha_j}$	Eq. 6.14

The mechanical properties presented in Table 9 are deducted based on the assumption that the wire strands are a set of idealised open-coiled helical springs with ends fixed against rotation (Wahl 1944) subjected to large elastic deformations. In case of a uniaxial loading, the force required to change the braiding angle from its initial value to a value α is given by Equation 6.20. The same angle can also be achieved by compressing the stent radially where the radial force is given by Equation 6.21. The equivalent stress derived from von Mises criterion is given by Equation 6.28 (Dieter 1961).

Table 9: Analytical model for computing mechanical properties of an open ends braid.

BRAID MECHANICAL PROPERTIES	OPEN ENDS BRAID FORMULAE	
CONSTANT C1	$C_1 = \frac{\sin 2\alpha_0}{D_0}$	Eq. 6.15

CONSTANT C2	$$C_2 = \frac{2\sin^2\alpha_0}{D_0}$$	Eq. 6.16
CONSTANT C3	$$C_3 = \frac{D_0}{\sin\alpha_0}$$	Eq. 6.17
SECOND MOMENT I	$$I_p = \frac{\pi d^4}{64}$$	Eq. 6.18
SECOND POLAR MOMENT I_P	$$I_p = \frac{\pi d^4}{32}$$	Eq. 6.19
AXIAL LOAD F	$$F = 2n\left[\frac{GI_P}{C_3}\left(\frac{2\cos\alpha}{C_3} - C_1\right) - \frac{EI}{C_3\tan\alpha}\left(\frac{2\sin\alpha}{C_3} - C_2\right)\right]$$	Eq. 6.20
RADIAL FORCE RF	$$RF = 2\pi F t_h \tan\alpha$$	Eq. 6.21
RADIAL PRESSURE P	$$P = \frac{2Ft_h\tan\alpha}{DL}$$	Eq. 6.22
LONGITUDINAL STIFFNESS K_L	$$K_L = \frac{2n}{\pi C_3 t_h \sin\alpha}\left[\frac{GI_P}{C_3}\left(\frac{2\sin\alpha}{C_3}\right) - \frac{EI}{C_3}\left(\frac{2\sin\alpha}{C_3} - C_2\csc^2\alpha\right)\right]$$	Eq. 6.23
RADIAL PRESSURE STIFFNESS K_P	$$K_P = \frac{2t_h}{C_3\cos\alpha\,(DL\cot\alpha)^2}\left\{2nDL\cot\alpha\left[\frac{GI_P}{C_3}\left(\frac{2\sin\alpha}{C_3}\right) - \frac{EI}{C_3}\left(\frac{2\sin\alpha}{C_3} - C_2\csc^2\alpha\right)\right] - F\left[C_3\cos\alpha(\pi tD - L\cot\alpha) + \frac{DL}{\sin^2\alpha}\right]\right\}$$	Eq. 6.24
BENDING STRESS σ	$$\sigma = \frac{64EI}{\pi d^3}\left(\frac{\sin^2\alpha}{D} - \frac{\sin^2\alpha_0}{D_0}\right)$$	Eq. 6.25
SHEAR STRESS τ	$$\tau = \frac{16GI_P}{\pi d^3}\left(\frac{\sin 2\alpha}{D} - \frac{\sin 2\alpha_0}{D_0}\right)$$	Eq. 6.26
EQUIVALENT SHEAR STRESS (TRESCA) τ_e	$$\tau_e = \frac{1}{2}\sqrt{\sigma^2 + 4\tau^2}$$	Eq. 6.27
EQUIVALENT STRESS (MISES) σ_e	$$\sigma_e = \sqrt{\sigma^2 + 3\tau^2}$$	Eq. 6.28

6.4.2 FE Modelling

Material Models

Phynox was considered, as the material used for fabricating the two designs. Phynox was modelled as an elastic material with the mechanical properties: Young's modulus 203.4GPa, Poisson's ratio of 0.32, yield strength of 1900MPa and ultimate

tensile strength of 2200MPa (Table 21 in Appendix 1.2). WallFlex stents are manufactured from Nitinol, therefore a material model for Nitinol (austenite Young's modulus 35.9GPa, Poisson's ratio of 0.33 and yield strength of 489MPa (De Beule 2008) is also considered. A pure elastic material model was created for Nitinol and its effectiveness in capturing the mechanical behaviour during radial compression was analysed.

Geometrical Models

Two braided stent designs resembling two commercially available devices marketed by Boston Scientific, US: WALLSTENT and WallFlex are investigated in this chapter. WALLSTENT design features open ends, while the WallFlex presents loops at the extremities.

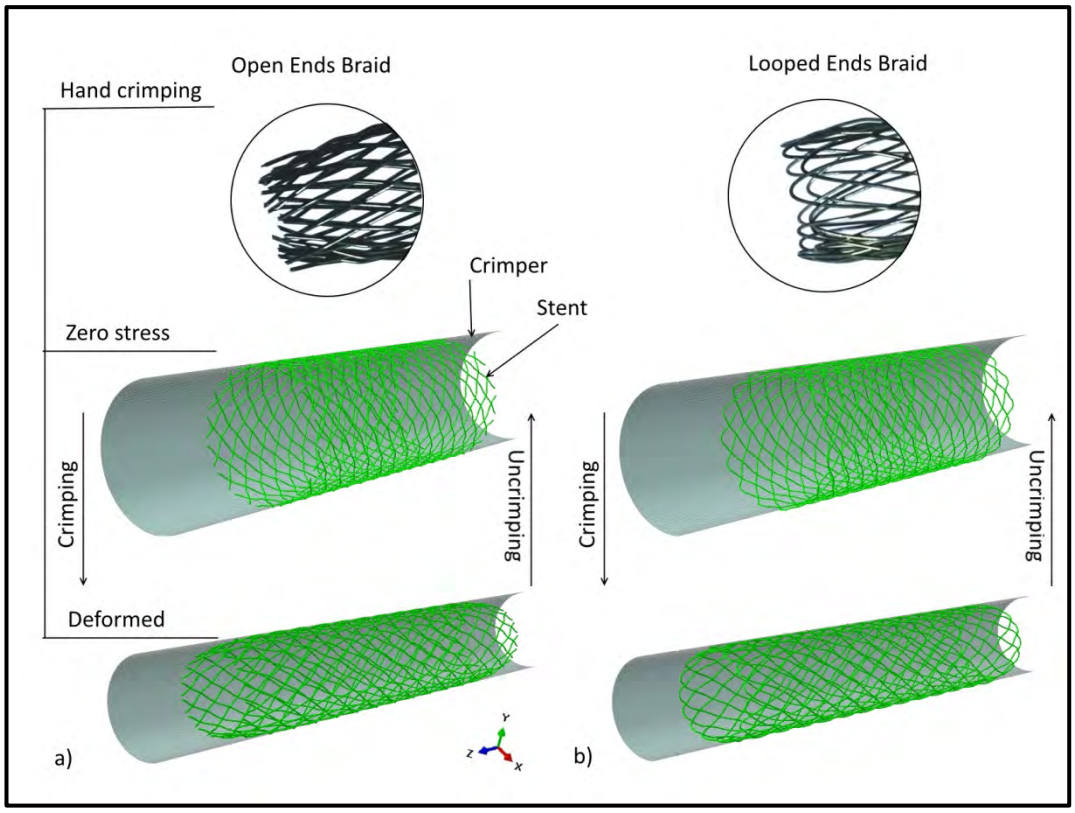

Figure 6-1: Hand crimping and simulation of the radial compression showing model in the initial configuration, zero stress at 22 mm diameter and in the deformed configuration at 10 mm diameter. a) open ends braid design b) looped ends braid design.

Both designs feature a straight shape and have the same geometrical configuration. The braid base model is created and discretized in pyFormex. The method used is presented in Chapter 5, particularly in Section 5.2.1 and Section 5.2.3. In terms of

finite element formulation strategy, the default choice throughout the thesis is B31 elements, as recommended by Hall and Kasper (2006). In this chapter, the simulation predictions when using B31 linear beam elements are compared with the solution featuring B32 beam elements with quadratic interpolation.

The two stent models in the unloaded, zero-stress state can be depicted in Figure 6-1. Their geometrical parameters are presented in Table 10 and resemble a Tracheobronchial WALLSTENT and a Colonic WallFlex stent. A number of node sets are defined for both models: a stent node subset created from the outer nodes to use in the contact formulation, a left hand and a right hand node to enable stent length computation, a node in the middle of the stent to centrally fixate the stent during the crimping simulation and 8 nodes in the middle section, for which to extract the von Mises stresses. The crimper was modelleld as a 3D deformable cylindrical shell as described in Section 5.3.3. The FE models discretization is presented in Table 10.

Table 10: Braided stent and crimper geometry characteristics of the FE models. Each stent design was modelled using two material models Phynox and Nitinol and was discretized using B31 and B32 elements.

BRAIDED STENT MODEL	OPEN ENDS STENT	LOOPED ENDS STENT	CRIMPER
INITIAL EXTERNAL DIAMETER D_{e0} (mm)	22	22	22.1
WIRE DIAMETER d (mm)	0.22	0.22	-
NUMBER OF WIRES n	30	30	-
INITIAL BRAIDING ANGLE α_0 (º)	50	50	-
INITIAL LENGTH L_0 (mm)	53.56	54	100
MATERIAL	Phynox/Nitinol	Phynox/Nitinol	-
ELEMENT TYPE	B31/B32	B31/B32	SFM3D4R
NUMBER NODES	6810/13590	6840/13680	278
NUMBER ELEMENTS	6780	6840	139
CONNECTOR TYPE (NUMBER)	HINGE (420)	HINGE (360) & SLIDE-PLANE (60)	-

Stent Crimping Simulation

The bases of the crimping simulation strategy were covered in Section 6.5. In this particular case, the simulation consists in a single loading & unloading step, where the radial displacement in cylindrical coordinates is applied using a smooth amplitude over the total time of the simulation (160 s) in order to modify the stent diameter from its initial diameter of 22 mm to the crimped diameter of 10 mm, which resembles the diameter of the catheter required in deployment, and back to 22 mm. As specified in Section 5.4, in terms of contact modelling, a frictionless surface-to-surface contact is defined between the inner face of the crimping tube and the node set formed by the outer nodes of the stent.

When performing an ad hoc crimping test up to a diameter of 10 mm (Figure 6-1), one can observe that in the case of the open ends design, the extremities of the stent tend to collapse. In contrast, the shape of the stent's extremities is preserved in the looped ends design, while the loops slide against each other. To account for this behaviour, the HINGE connectors situated at the ends of the stent with looped ends design are replaced with SLIDE-PLANE connector elements.

Postprocessing

The impact of stent model and material choice was analysed by focusing on the variation of stent length as a function of diameter. The plotted stent length was computed by adding the absolute values of the displacements of the left hand and a right hand node sets defined for the stent model to the initial length. The radial forces on the unloading path (chronic outward forces or expansion forces) versus the stent diameter were examined, to reflect the compression experiment performed by Jedwab and Clerc. Finally, the von Mises stresses were computed as the average of the stresses extracted in the 8 nodes picked in the middle section of the stent, and the equivalent Misses stress versus diameter diagram was plotted. The peak von Mises stresses due to local stress concentrations are also presented.

6.5 Results

Figure 6-1 illustrates the stent and crimper assembly at initial and crimped stage during a typical radial compression simulation in comparison with the response of the stent during hand crimping. According to Equation 6.8, the length of the stent is

influenced only by the braiding angle. The validation of the FE model for the open ends braid design is depicted in Figure 6-2 and consists of 2 aspects:

- geometrical validation by comparing the stent length versus diameter calculated using Equations 6.1-6.8 with the numerical predictions;
- mechanical behaviour validation by comparing the computed radial force (Equations 6.15-6.21) versus stent diameter and equivalent stress according to von Mises criterion (Equations 6.25-6.28) with the numerical predictions.

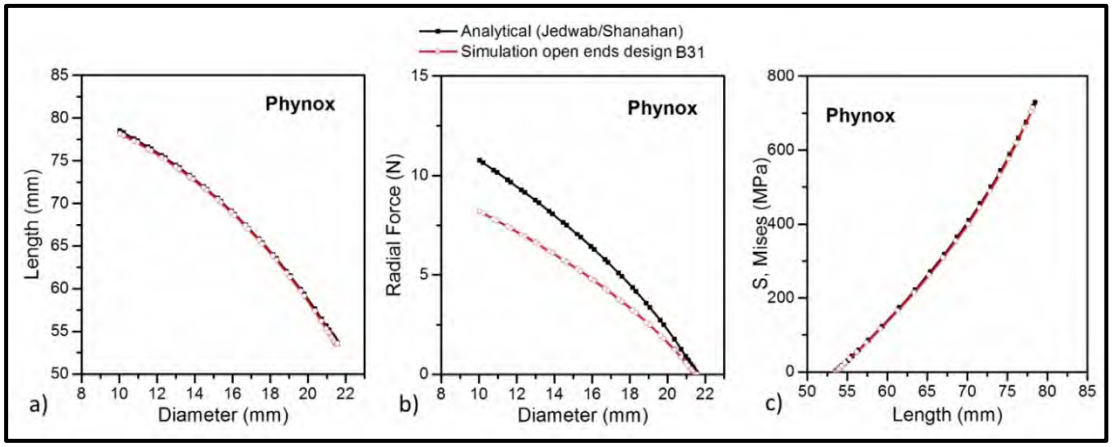

Figure 6-2: Validation of the FE Phynox-built open ends model against the analytical model. a) Stent length vs. diameter b) Radial force vs. diameter c) von Mises stress vs. stent length.

The length versus diameter curves (Figure 6-2a) show excellent agreement between the analytical and numerical solution with an R-squared value of 99.9%. The equivalent stresses in the beams curves situated in the mid-section of the stent (Figure 6-2c) also show an excellent agreement between analytical model and simulation with an R-squared value of 99.9% for the open ends design and 99.7% for the looped ends design.

The radial force versus diameter curves show that an increase in the diameter is reflected by a decrease in the radial force exerted on the crimping tool. There is a close agreement between theory and FE predictions; however, the predictions are below the theoretical values, which may be explained by the fact that the extremities of the stent collapse during the compression, therefore not contributing to the overall figure of the radial force, behaviour which seems to agree with the ad hoc crimping experiment.

Figure 6-3 presents a comparison between behaviour of the two designs from analytical and numerical point of view based on material choice: Phynox and Nitinol and FE type B31 and B32 used in discretizing the wire. von Mises stress predictions presented in this figure, represent the mean of von Mises stresses extracted from 8 nodes positioned in the mid-section of the stent.

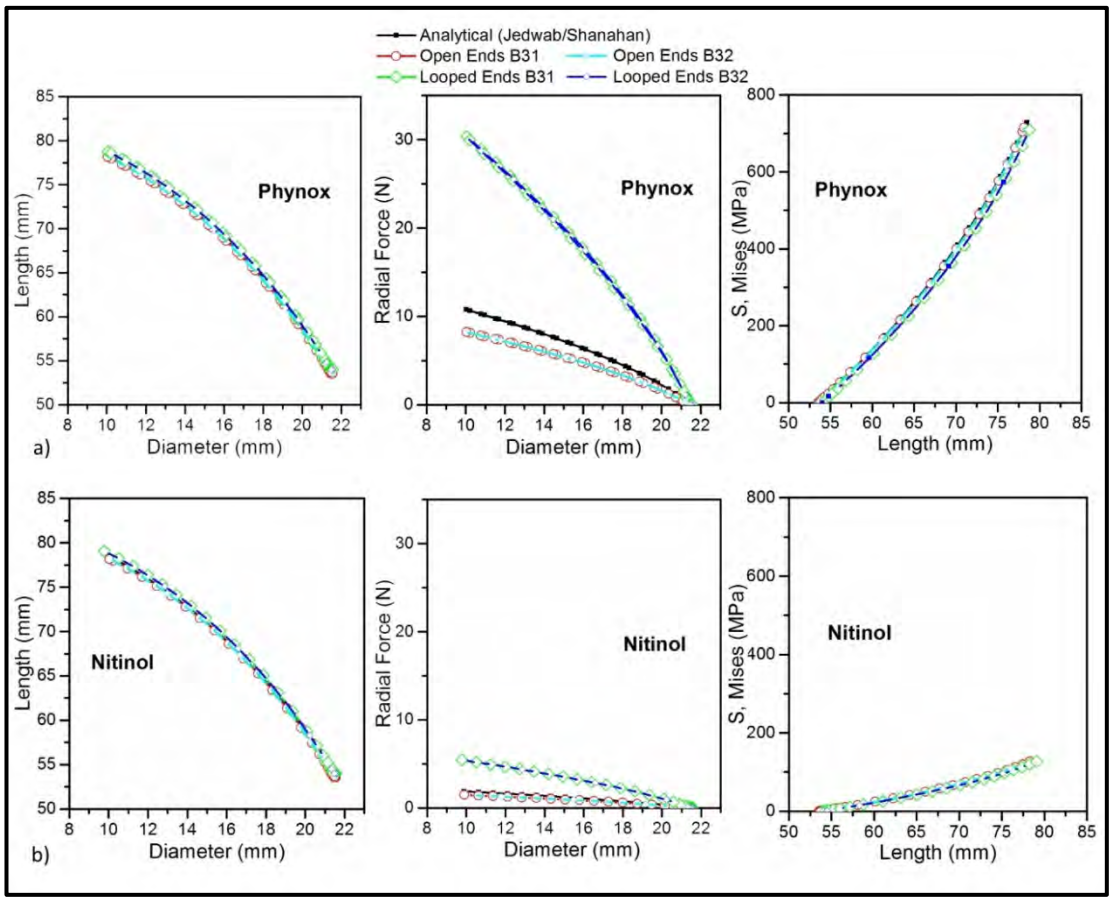

Figure 6-3: Stent length vs. diameter, radial force vs. diameter and von Mises stress in the mid-section vs. stent length. A comparison between the analytical and simulation results for the two braided stent designs, open ends and looped ends braid, based on the material choice and FE element type: B31 and B32. a) Predictions for the Phynox-made stent b) Predictions for Nitinol-made stent.

An excellent agreement with R-squared value of 99.9% between the theoretical variation of the stent length in terms of diameter and the numerical predictions for both stent designs irrespective of the type of material may be noted in Figure 6-3. The theoretical value of the equivalent stress is also in very close agreement with the predicted FE values calculated by averaging the von Mises stresses at 8 nodes situated in the mid-section of the stent for both stent designs and both materials, with R-squared value of 99.9%. The difference in the predictions of the stent's length and

radial forces when using the B31 and B32 elements is minimal, below 1%. The same response can be observed in the case of the von Mises stresses predictions in the mid-section of the stent, suggesting no particular benefit in using quadratic beam elements in this region of the stent. However, the prediction of the stresses in the looped ends is clearly influenced by the element choice.

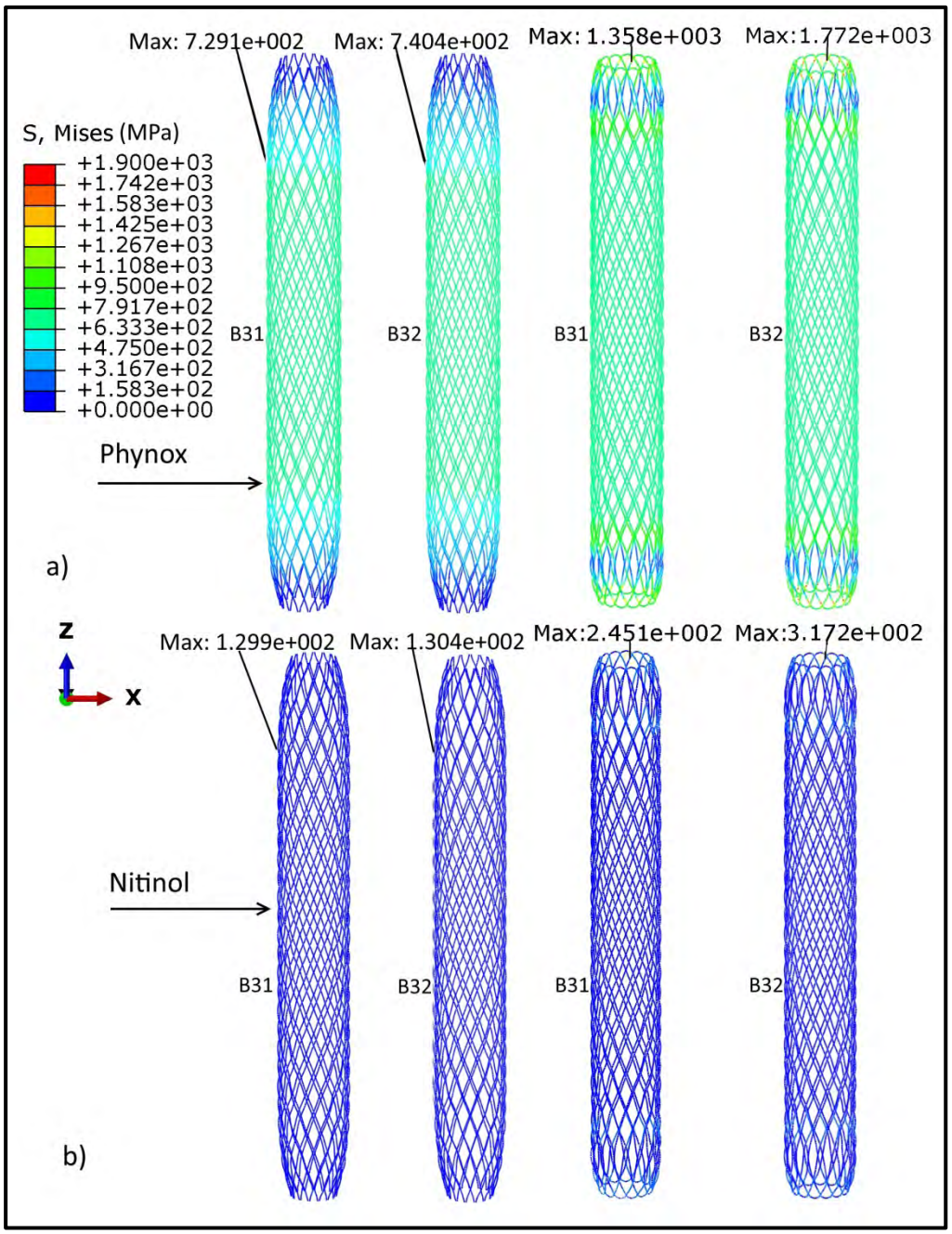

Figure 6-4: Contour plots of von Mises stress peak distributions for the two braided stent designs, based on the material choice: Phynox and Nitinol and FE type: B31 and B32. a) Open ends design in Phynox material b) Looped ends design in Phynox material c) Open ends design in Nitinol d) Looped ends design in Nitinol.

The von Mises stress peak distributions in the stent beams in the fully crimped state for both stent designs and each of the material models used are depicted in Figure 6-4. The detailed view of Figure 6-4 depicts the stress concentration at the extremities of the stent in the loops area, with highest value recorded for the Phynox stent (Figure 6-4b). The values of the von Mises stress measured in the mid-section of the stent in the fully crimped state, as well as the peak values are reported in Table 11.

Table 11: Comparison between the analytical and numerical predictions of the von Mises stress extracted from nodes in the mid-section of the stent in the fully crimped state and peak values when using B31 elements. The stress values predicted when using B32 elements are presented in brackets.

MATERIAL	YIELD STRESS (MPa)	VON MISES STRESS ANALYTIC (MPa)	VON MISES STRESS SIMULATION (MPa)	
			OPEN ENDS BRAID	LOOPED ENDS BRAID
PHYNOX	2200	729	Mid stent 715(722)	Mid stent 709(711)
			Peak 729(740)	Peak 1358(1772)
NITINOL	489	127	Mid stent 127(127)	Mid stent 127(126)
			Peak 130(130)	Peak 245(317)

6.6 Discussion

The general observation in relation to the implication of using the B31 and B32 elements is an increase in the accuracy of the stresses when using B32 element formulation, phenomenon which was expected according to Abaqus documentation (Abaqus Inc 2014). The increase in the stress values is around 1% in the case of the open ends braid design peak and mid-section, and in the case of the looped ends braid design in mid-section. However, the effect of the loading in the design featuring the looped ends is more complex than the effect of the crimping in the mid-section, involving bending, transverse shear and torsional shear stresses. Due to this increased complexity, the benefit of using B32 elements becomes more evident in the case of identifying the peak von Mises stresses for the looped ends braid, where it is

noticed a difference increase of 23% for both materials (Table 11). Due to the quadratic formulation of these elements, a more accurate prediction of the displacements of the nodes in the looped ends is possible when using B32 beam formulation in this case.

The analytical model cannot predict the peak stresses for the looped ends design. The magnitude of the stresses in the loops section shows a 46% increase in comparison to the theoretical stress when using B31 elements, while when using B32 elements the stresses show an increase of 58%. Furthermore, the analytical model cannot predict the radial forces of the looped ends stent (Figure 6.3 Radial Force vs. Diameter). It may be noted that in the case of the open ends design, the extremities of the stent do not contribute to the magnitude of the expansion forces. In contrast, in the case of the looped ends design, the magnitude of the radial forces is determined by the reaction forces in the loops, the extremities being much stiffer than the mid-section of the stent.

6.7 Conclusion

The numerical predictions of the stress (Table 11) imply similar functionality of the two designs when considering the mid-section of the device. However, the extremities, in particular the looped ends induce 3.7 times higher radial forces than the open ends version. In conclusion, the analytical model is not entirely applicable to the looped ends design. The analytical model applied to the looped ends design is able to predict the change in length for a prescribed change in diameter. The equivalent stresses can also be predicted in the mid-section of the stent, with a very small influence of the element type. However, the peak stresses in the looped ends and the magnitude of the radial forces can only be predicted by the FE model. The results suggest that B32 element formulation is suitable in the looped ends design, giving a higher accuracy of the solution. The study highlights the effects of design to the mechanical behaviour of the braided stent. FEA in the case of the looped ends design combined with the Phynox material model highlighted a very high level for the radial forces, which leads to excluding this combination as a potential stent design for colonic stenting applications without the need to actually go through the process of fabricating and testing real prototypes. The human colon has a number of twists and turns, therefore stents suitable for the colonic stent applications need to be

flexible to allow ease of delivery to the target area. FEA showed that the Nitinol version of the looped ends design has lower stiffness, therefore confirming the existence of this combination on the current market for colonic stent applications.

Yet, some limitations of the work exist and may be addressed in further studies: both models have neglected the effect of friction between the stent and the crimping tool, which may influence the magnitude of the stresses and radial forces; to fully validate the FE model and the predicted mechanical behaviour, a radial compression test would be required.

The key-design objectives for a self-expanding braided stent may be: (1) to minimise the risk of restenosis by preventing lumen trauma which induces thrombosis and proliferation of cells. This is done by ensuring a reduced radial expansion force and by using a coating; (2) to provide adequate scaffolding in order to maintain lumen patency. This is done by ensuring optimum radial resistive force.

However, especially for stents targeting stenosis and leaks of the gastrointestinal tract, other objectives such as (3) minimising stent migration and (4) the ability to access high tortuosity and angulation without fracturing, are also highly important. Nevertheless, when developing a stent design, the former objectives (1&2) are in competition with the latter ones (3&4), such that improvement of one property would result in trade-off of the others.

This study shows the great potential of FEA in the stent design analysis. FEA provides a way to create a multitude of stent models and analyse their mechanical behaviour during loading resembling in-vivo conditions, in a fast and efficient manner in comparison to traditional build and break approach to stent design.

Chapter 7
Viscoelastic PDO Braided Stent

The mechanical properties of the viscoelastic monofilament used in the fabrication of the braided stents were presented in Chapter 4, Section 4.1. The monofilament was subjected to uniaxial tensile and extensional creep testing with the purpose of predicting the material's time dependent characteristics. This chapter presents in detail the development of the PDO FE model and the stent crimping simulation. Abaqus ver. 6.14 is used to develop the linear viscoelastic constitutive material model for PDO, where the creep compliance function and stress relaxation function were derived from experimental data. The material model is validated by performing simulation of radial compression for a braided stent and a comparison between the experimentally evaluated radial forces of the braided stent and the finite element prediction is presented in this chapter.

7.1 Introduction

The vast majority of the stents are metallic and reside permanently inside the lumen, or until they are removed through surgical intervention. In an attempt to address the problem of restenosis, drug eluting stents (DES) were developed in the early 2000. DES have demonstrated superiority in the short term, with lower rates of restenosis in comparison to the bare metal stents, however, in the long term, there are concerns regarding stent thrombosis (Ben-Dor *et al.* 2011).

To eliminate the need for a surgical procedure when the stent is needed only temporarily and to potentially overcome some of the stents' drawbacks related to restenosis, several medical devices companies have developed biodegradable stents. Some of the materials used for this purpose are magnesium alloys and biodegradable polymers such as Polydioxanone (PDO), Polylactic acid (PLA) and Poly-L-lactic acid (PLLA).

Radial stiffness is one of the most important mechanical characteristics of stents (Duerig and Pelton 2002; Stoeckel *et al.* 2003). Although radial forces can be evaluated experimentally (Duda *et al.* 2000; Nuutinen *et al.* 2003; Liu 2006; Isayama *et al.* 2009), the tests are difficult to implement and costly. Validated FE braided stent models were developed by De Beule *et al.* (2007; 2008), Kim *et al.* (2008), Zhao *et al.* (2012), Ma *et al.* (2012) and Frost *et al.* (2014), in an attempt to analyse their mechanical behaviour. Generally, Abaqus/Explicit was used in the analysis of the stent behaviour during axial elongation, radial compression, bending, fatigue, crimping and deployment. Metallic stents made out of stainless-steel, Phynox and Nitinol were modelled (e.g. Nitinol material modelled as a User Material, covering its superelastic effect, Phynox and stainless-steel modelled as linear elastic materials, assuming the small strain regime). The only FEA of polymeric braided stents was performed by Peirlinck in 2013 (Peirlinck 2013).

7.2 Methodology

The objective of this section is to use FEA to evaluate the time-dependent viscoelastic response of a braided stent subjected to crimping. The general steps required in developing the linear viscoelastic material model in Abaqus were presented in Chapter 5, Section 5.1.

The methodology consists of:

1. Creating & calibrating the linear viscoelastic material model;
2. Creating the braided stent and crimper geometrical models;
3. Validating the FE model by comparing the results of a tensile creep simulation with the experimental data presented in Section 4.1.2 and Section 4.4.2;

4. Performing radial compression simulation and compare the predictions with the results acquired from the crimping experiment presented in Section 4.3 and Section 4.4.3.

7.2.1 FE Modelling

Linear Viscoelastic Material Model for PDO

In the Abaqus material editor, "Elastic" behaviour was selected from the elasticity behaviours under the "Mechanical" menu and the value for the instantaneous elastic modulus 720MPa determined at Section 4.4.1, was input. Poisson's ratio of PDO was assumed to be 0.45 (Peirlinck 2013). The "Viscoelastic" behaviour in time domain was added by including the creep test data. By using the "Evaluate" functionality, the Prony series coefficients (Table 12) are calculated and the material model calibration is complete. Shear creep compliance versus time plot depicted in Figure 7-1a, contains the Abaqus predicted curve and the curve for the experimental data included in the material specification. Vertical error bars show variability of the data and represent a single standard deviation from the mean. Creep data is converted internally into stress relaxation data and the normalised response plots are depicted in Figure 7-1b. Conversion of creep data is reported in Table 23 of the Appendix 3.1.

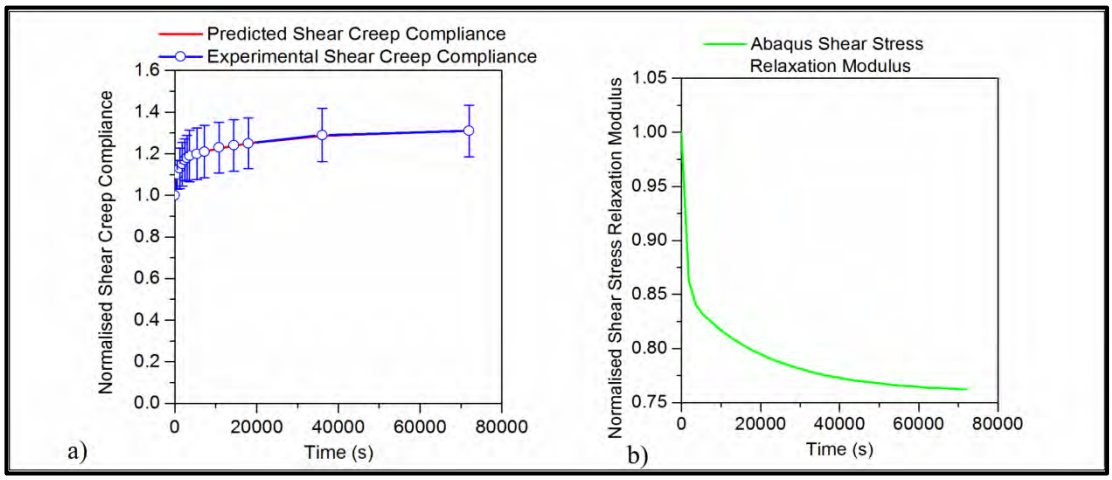

Figure 7-1: Development of the Abaqus material model using creep experiment on PDO polymer monofilament and "Evaluate" function. a) FE prediction of shear creep compliance compared with experimental data after conversion into shear creep. Error bars represent a single standard deviation from the mean (n=3) b) Predicted shear stress relaxation modulus extracted from Abaqus model.

Table 12: Viscoelasticity defined in the time domain for a linear, isotropic material. Prony series coefficients defined in Equation 5.8, where i is series term, g_i is the normalised shear stress relaxation modulus at series term i and τ_i is the relaxation time at series term i.

i	g_i	ψ_i
1	0.14681	849.30
2	9.36239E-02	20395.0

Validation of the Material Model

The material model validation was performed by comparing the predictions of a tensile creep simulation with the experimental data reported at Section 4.4.2. In the tensile creep simulation, the quasi-static response of a piece of PDO monofilament to a concentrated force was analysed.

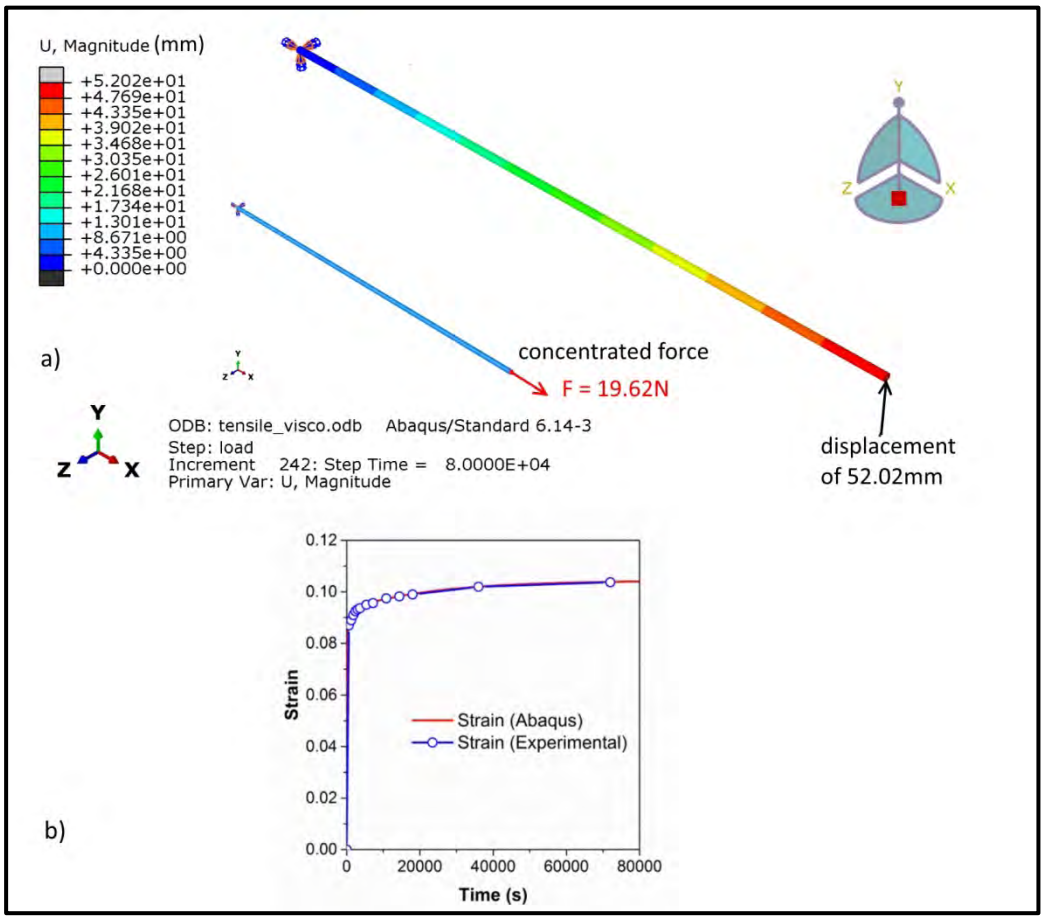

Figure 7-2: Validation of the developed Abaqus model using a tensile creep experiment on PDO polymer monofilament. a) A displacement of 52.02 mm for the node at the extremity of the specimen is predicted following a constant loading applied, while the other end is fully restrained b) Comparison between the creep strain obtained experimentally and the Abaqus prediction.

A 3D deformable wire part was created, for which a section with a circular profile and the PDO material model were assigned. The part was meshed using B31, a 2-node linear beam in space element, which accounts for large axial strains as well as transverse shear strains. The model was analysed in Abaqus/Standard using a "Visco" step. A load of 19.62N was applied at one end for a total of time of 80,000s, while the other end was fully constrained (Figure 7-2a). Displacement/Rotation boundary conditions were applied to one end of the monofilament in the initial step of the analysis to constrain all movement and rotation. A concentrated force of 19.62N was applied to the other end of the monofilament in the positive X direction and activated in the "Visco" step. Figure 7-2b depicts a comparison between strains from a subset of the experimental creep and from the computed values showing a perfect match. These results validate the material model and confirm the idea of choosing a "Visco" step for the analysis of 3D viscoelastic beams.

Geometrical Models

The braided stent model is created and discretized in pyFormex following the method presented in Chapter 5, particularly in Section 5.2.1 and Section 5.2.2. The crimping tool is modelled in two ways: 8 Plates Crimper (Section 5.3.1) and Octagonal Crimper (Section 5.3.2). The assembly in the unloaded and loaded state including displacements in the elastic formulation can be depicted in Figure 7-3. The contact modelling was described in Section 6.4 and with friction coefficients of 0.1 and 0.2 were used.

Stent Crimping Simulation

In this simulation the self-expanding PDO braided stent was subjected to crimping by a crimping tool, therefore the parts to be assembled are: the stent model and the crimper model.

The simulation strategy is to perform the stent deformation using both linear viscoelastic elastic and linear elastic models to assess whether or not the viscoelastic model offers improved predictions when compared with the elastic model predictions and with the experimental data from the crimping test. 1-step and 2-step analyses were used to identify the analysis leading to the most robust and cost effective solution. Four case scenarios were investigated as shown in Table 13. The stent itself

doesn't have a load applied directly. Instead, crimping was achieved by radial displacement applied to reference points situated on the rigid plates or the octagonal tubular shell respectively, in a local cylindrical coordinate system. To analyse the effect of material model choice on the radial force, a combination of various analysis steps and crimping conditions are considered. The material behaves purely elastically during the static steps whether or not its viscoelasticity is specified in the material model. In the quasi-static version, the Explicit/Implicit direct integration is used to activate the viscoelastic behaviour and a tolerance of 5e-6 is used to control the accuracy of the creep integration.

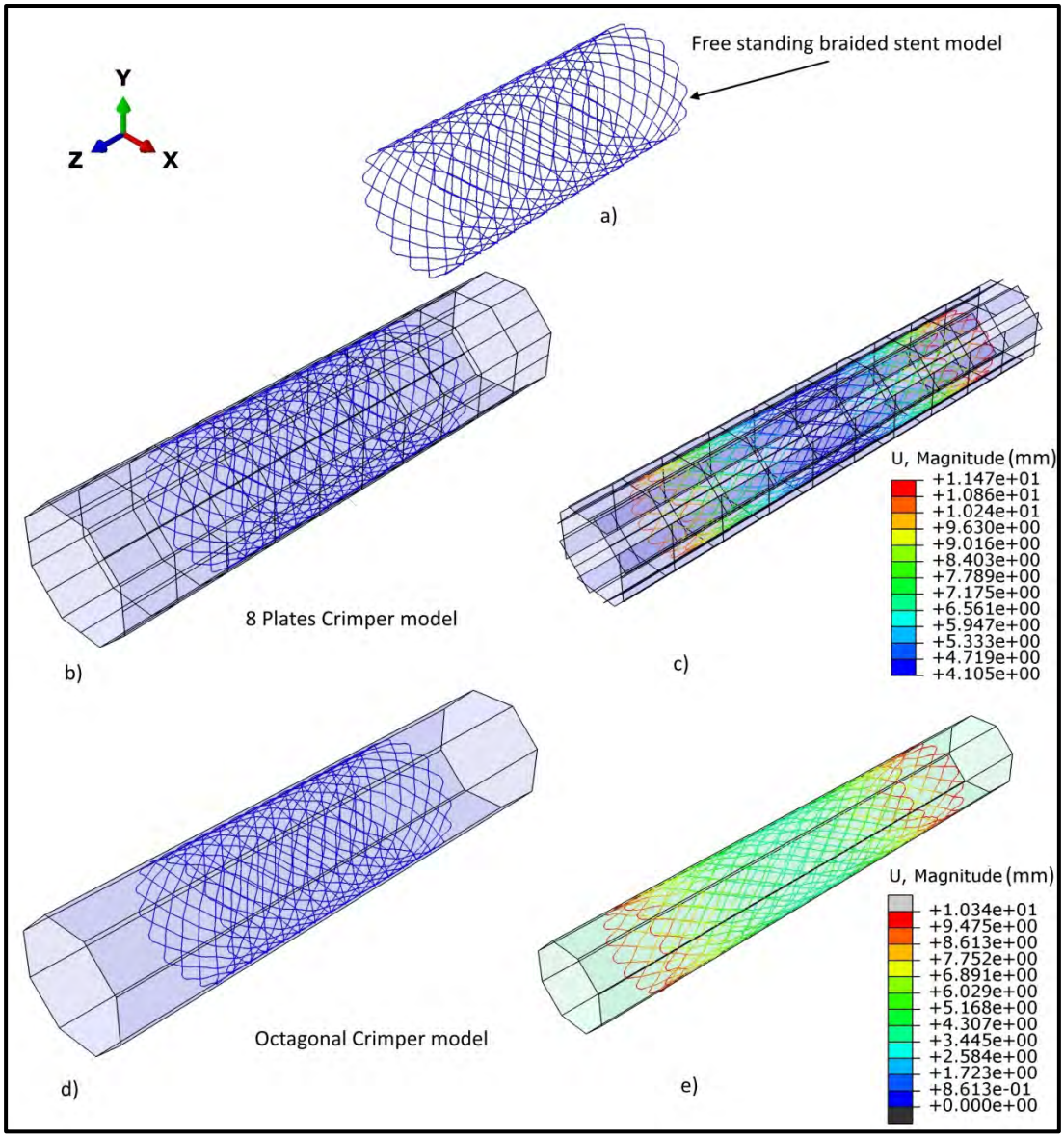

Figure 7-3: Braided stent crimping simulation. a) Braided stent model generated in pyFormex and imported into Abaqus b) Unloaded stent inside the 8 Plates Crimper c) Loaded stent inside the 8 Plates Crimper d) Unloaded stent inside the Octagonal Crimper e) Loaded stent inside the Octagonal Crimper.

Table 13: 4 case scenarios describing the loading procedure in crimping/uncrimping simulations.

	Case 1	***Case 2***
8 Plates Crimper	*1 step analysis* *a) elastic step SA b) visco step QSA* *Amplitude: tabular* *Boundary Conditions (BC):* 1. Fix the crimper: no rotation or axial movement allowed; BC assigned to the 8 reference points coinciding to the centre of the polygonal plates 2. Fix the stent: no rotation or axial movement allowed; BC assigned to a node in the middle of the stent 3. Crimp/Uncrimp: radial displacement from 22mm to 14mm and back to 22mm; BC assigned to each of the 8 reference points. Crimp = ascending leg of the tabular amplitude curve (0-80s); Uncrimp = descending leg of the curve (80-160s).	*2 step analysis* *a) elastic steps SA b) visco steps QSA* *Amplitude: ramp* *Boundary Conditions (BC):* 1. Fix the crimper: same as Case 1 2. Fix the stent: same as Case 1 3. Crimp/Uncrimp: BC assigned to each of the 8 reference points on the polygonal plates - Created in the first step: radial displacement to reduce diameter to 14mm over 80s (= crimping) - Modified in the second step: radial displacement changed to 0 to allow recovery back to 22mm over 80s (= uncrimping)
	Case 3	***Case 4***
Octagonal Crimper	*1 step analysis* *a) elastic step b) visco step* *Amplitude: tabular* *Boundary Conditions (BC): same as Case 1*	*2 step analysis* *a) elastic steps b) visco steps* *Amplitude: ramp* *Boundary Conditions (BC): same as Case 2*

7.3 Results

All scenarios described in Table 13 were successfully performed using the implicit solver, the CPU time varying in the range of 250-300s for the simulations using the octagonal crimper, to a range of 2000-3000s for the simulations using the 8 plates crimper. Two material models – linear elastic and linear viscoelastic were employed in each case scenario, therefore leading to a total of 8 stent crimping simulations.

Postprocessing for each job consisted in the calculation of the radial forces and radial displacements. Figure 7-4 depicts radial force curves with respect to analysis time showing the effect of material model choice on the radial force in various crimping conditions. The predicted values for the radial force versus stent diameter were compared with the experimental results (Figure 7-5).

7.4 Discussion

When comparing the stent radial force histories, it is observed that the shapes of the curves depicting the crimping behaviour versus time and the magnitude of the radial forces are similar, independent of the type of analysis used or the crimping tool model. As expected, a softer response is recorded in the case of using the quasi-static procedure. This behaviour is quite visible in Cases 1 & 2.

A much smoother transition from the fully crimped state at the tip of the curve (Figure 7-4a) to uncrimped state is observed in the case of the viscoelastic model. Also, when unloading in Figure 7-4b, a bounce of the structure is observed when using the elastic model, while the transition to the large diameter is smooth when using the visco-elastic model. However, in Case 3 & Case 4 which account for the stent crimped by an octagonal crimper, the difference is too small to create a visible impact.

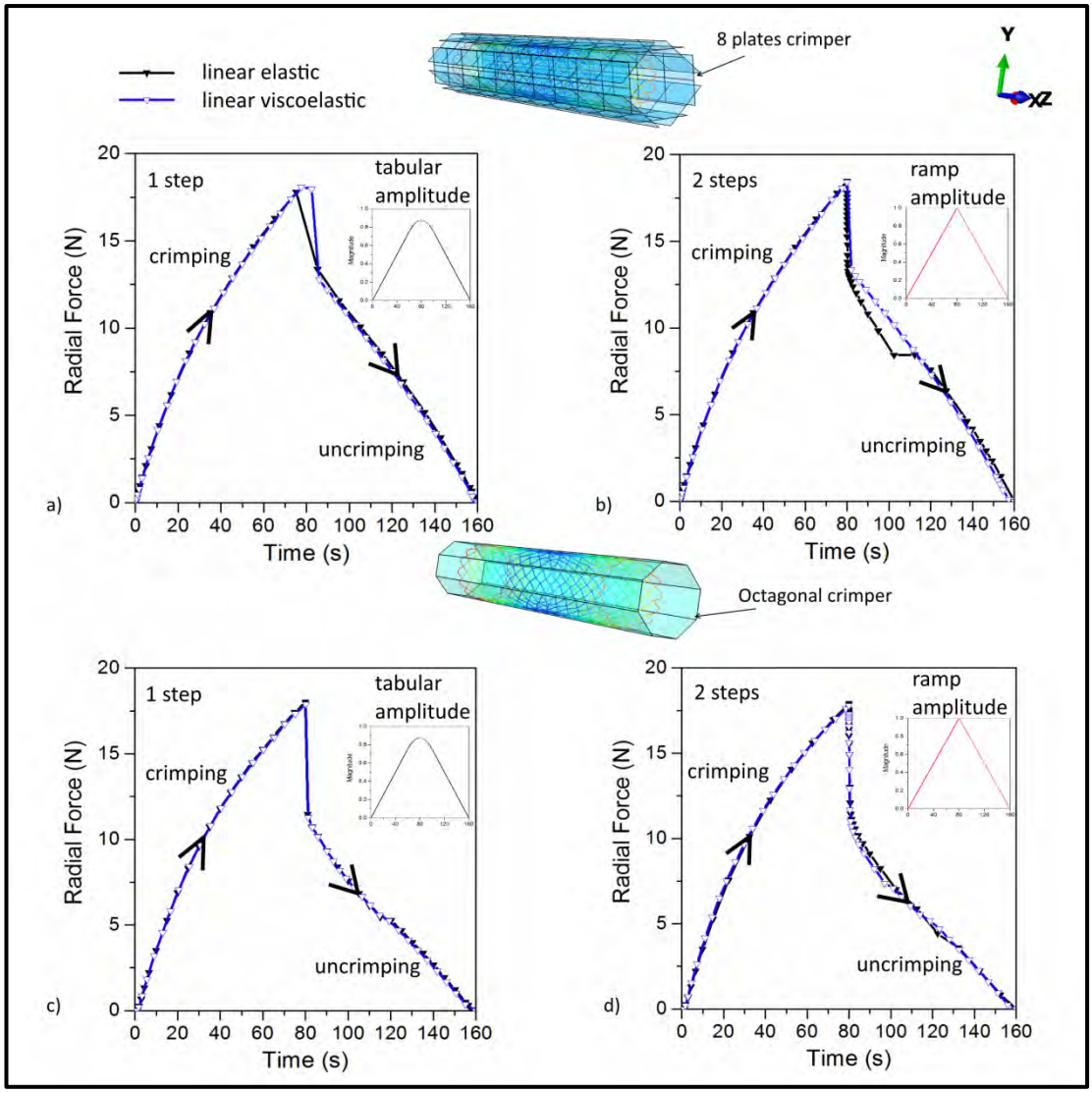

Figure 7-4: Effect of linear elastic and viscoelastic material models on Radial Force obtained with various steps and crimping conditions. a) Case 1: 1 step analysis of stent crimping simulation using an 8 plates crimper with displacement applied by tabular amplitude b) Case 2: 2 step analysis of stent crimping simulation using an 8 plates crimper with displacement applied by ramp amplitude c) Case 3: 1 step analysis of stent crimping simulation using an octagonal crimper with displacement applied by tabular amplitude d) Case 4: 2 step analysis of stent crimping simulation using an octagonal crimper with displacement applied by ramp amplitude.

Loading and unloading paths created a hysteresis loop which was observed in all scenarios (Figure 7-5). The experimental hysteresis loop depicted a lower magnitude and a linear dependency between the radial force and stent diameter on the crimping path in comparison to the magnitude of radial force and the convex shape of the path observed in all simulations. The unload path in Case 1 & 2 (Figure 7-5a,b) is slightly concave as opposed to the convex shape observed in the Case 3 & 4 (Figure 7-5c,d) and in the case of the test data.

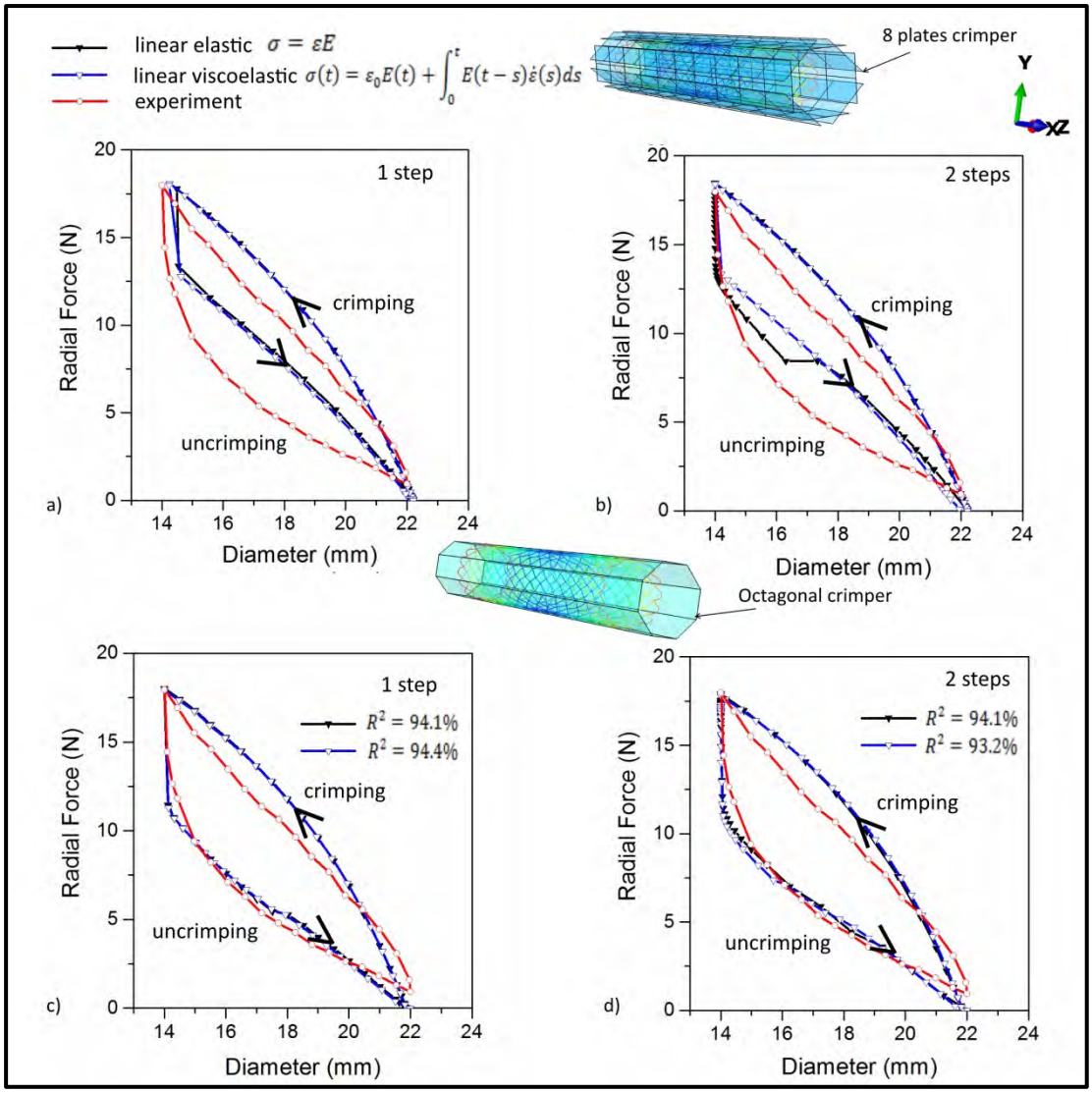

Fig. 7-5: Abaqus linear elastic vs. linear viscoelastic model predictions. a) Case 1: Simulation using an 8 plates crimper with displacement applied by tabular amplitude during 1 step crimp-uncrimp b) Case 2: Simulation using an 8 plates crimper with displacement applied by ramp amplitude during a 2 step analysis crimp-uncrimp c) Case 3: Simulation using an octagonal crimper with displacement applied by tabular amplitude during 1 step crimp-uncrimp d) Case 4: Simulation using an octagonal crimper with displacement applied by ramp amplitude during a 2 step analysis.

The magnitude of the radial force recorded during the experiment is again lower than the predicted values. These observations led to the conclusion that the stiffness of the stent model is higher than the stiffness of the stent prototypes. The difference in stiffness could be attributed to the type of connector element that was chosen to model the contact between two crossing wires. It was noted that one of the factors influencing the magnitude of the radial forces and the hysteretic behaviour of the braided stent was the friction force between the stent wires and the crimping tool. In

all case scenarios, the higher the friction, the greater the force required for the stent wires to slide inside the crimper, inducing higher radial forces in the loading phase. In the same time, the higher the friction, the hysteresis increased, leading to a higher energy loss. The simulation results showed best agreement with the experiment when using a friction coefficient of 0.1 in the stent-8PC model and 0.2 in the stent-OC model respectively. The general contact interaction between selected surface pairs used in the 8PC model had difficulty in accurately resolving this contact: a 0.2 friction coefficient led to too high radial forces in the loading phase, while a 0.1 value led to too little hysteresis when comparing with the experiment; eventually, 0.1 penalty led to the closest fit.

The OC model seemed to be superior to the 8PC model suggesting that the interaction based on node to surface discretization with a 0.2 friction coefficient used in this model was more suitable for modelling the polymeric braided stent-crimper contact. Trial jobs were run using smooth step, tabular and ramp amplitudes in combination with 1 and 2-step analysis and the final choice of the simulation scenarios was made based on the convergence outcome. The 1-step analysis combined the tabular loading amplitude seemed to lead to more accurate results than the 2-step analysis, outcome which could be attributed to the continuous transition at the tip of the loading where the stent approached and departed the minimum diameter.

Modelling the crimping tool in the two versions gave the opportunity in identifying the best fit case scenario. A regression analysis was carried out for Case 3 & 4 (Figure 7-5c,d) and R-squared values were computed for the linear elastic and linear viscoelastic material models. The best prediction, with an R-squared = 94.4%, was observed in Case 3 (Figure 7-5c), which consisted in a simulation based on 1 step analysis using a linear viscoelastic model for the stent material, an octagonal crimper and a displacement applied by tabular amplitude.

Ultimately, the fact that there was no visible advantage in using the viscoelastic material model, led to the conclusion that the crimping behaviour of braided stents was mainly dictated by the structure itself rather than the viscoelasticity of the material. Nevertheless, the viscoelastic material model may prove to be more accurate in other types of testing. The model could be applied to a SX Nitinol stent

and its fatigue behaviour could be assessed. It could also be used in orthopaedic applications where there is a need for shock absorption (e.g. spinal vertebrae spacer).

7.5 Conclusion

The objective of this chapter was to analyse the crimping behaviour of a viscoelastic polymeric braided stent using experimental and numerical methods. Three experiments were performed including two tensile tests for capturing the time-dependent behaviour of the viscoelastic monofilament and a radial force test on in-house fabricated braided stents.

To the best of the author's knowledge, a viscoelastic material model has never been used in conjunction with a braided stent. Previous work has generally used a purely elastic material model, a static step with smooth amplitude and Abaqus/Explicit analysis (Peirlinck 2013), the time-dependent nature of the polymer being ignored. By using the linear viscoelastic material model and Abaqus/Standard, it was demonstrated that it is possible to predict an accurate behaviour of the braided stent during the crimping and uncrimping. The simulation results showed a good agreement with the experiment and confirmed the effectiveness of using FEA research tool in the stent analysis.

Chapter 8
Viscoelastic Nitinol Braided Stent

Two Nitinol material models - a viscoelastic and a superelastic-plastic material model are compared for their effectiveness in capturing its complex behaviour during loading and unloading using nonlinear FEA in this chapter. The accuracy of the two models is verified by comparing the FE predictions of radial resistive forces and chronic outward forces of a Nitinol stent with empirical data. The superelastic-plastic model is implemented as a built-in user material with material constants obtained by calibrating its behaviour based on a uniaxial tension test performed in house. The Prony series parameters required for the viscoelastic material characterisation are obtained by fitting the model to experimental creep tensile data from the literature.

8.1 Introduction

Nitinol has been extensively utilised in the medical engineering world since late 1980's due to its amazing superelasticity, shape-memory effect, biocompatibility and fatigue resistance properties. Furthermore, similar to other biomaterials, Nitinol exhibits viscoelasticity.

Available numerical studies dedicated to SX Nitinol braided stents are focused on the superelastic property of the material (Conti 2007; De Beule *et al.* 2007, 2010; Záhora *et al.* 2007; Kim *et al.* 2008; Auricchio *et al.* 2011; Zhao *et al.* 2012, 2013; Frost *et*

al. 2014). Abaqus is generally employed in these studies and the Nitinol material model is created by implementing a user material subroutine (UMAT). Since 2005, Abaqus has built-in a Nitinol material model to simulate its superelastic behaviour at finite strains. The superelastic-plastic capability is available since 2010, the choice between the two being differentiated by the number of material constants used.

In the present work, a viscoelastic material model and a superelastic-plastic material model are created for Nitinol and FEA is used to analyse the mechanical behaviour of a SX braided stent subjected to radial compression in a loading and unloading cycle. The accuracy of the two models was verified by comparing the predictions of the radial compression simulation with empirical data acquired in a radial compression experiment.

8.2 Methodology

The methodology consisted in creating and calibrating two material models: viscoelastic and superelastic-plastic; generating the geometrical models for the braided stent and the crimping tool; performing the radial compression simulation and evaluating the accuracy of the material models by extracting the radial forces in terms of stent diameter and comparing the predictions with the empirical data acquired from the crimping test performed on Nitinol braided stent prototypes.

8.2.1 FE Modelling

Material Models

Superelastic-plastic Material Model

In order to calibrate the superelastic-plastic material model in Abaqus, a new Data Set was populated with the engineering strain-stress data acquired from the uniaxial tensile test (Section 4.5.2) and Abaqus' Nitinol superelastic-plastic plug-in was used to specify the Calibration Behaviour. The plug-in offers an interface for picking the five points of interest on the stress-strain plot from the Data Set previously created: start of transformation A → M during loading, end of transformation A → M during loading, a point in martensite, start of transformation M → A during unloading and

end of the transformation M → A during unloading. Four plastic points were also picked from the plot.

Other constants, such as test temperature, Poisson's ratio, start of transformation stress in compression and volumetric strain were also plugged in. The stress/temperature gradients in austenite and martensite phases were calculated based on the transformation temperatures revealed by the DSC analysis (Section 4.5.1). Table 14 presents the list of material constants used in the calibration of the material model. The plug-in offers the option to evaluate the material definition using a 3D one-element model subjected to uniaxial tensile test resembling the experiment procedure. The comparison between the predicted results and uniaxial test data is shown in Figure 8-1. A number of state variables are computed during the analysis, from which the volume fraction of martensite (SDV21) is of interest when investigating the influence of Nitinol's microstructural phase on its uniaxial response.

Table 14: Material constants used in the calibration of the superelastic-plastic model in Abaqus, including the stress-strain pairs for the four plastic points shown in Figure 8-1.

NO.	INPUT PARAMETER	DESCRIPTION	VALUES
1	E_A	Austenite elasticity (MPa)	33013
2	ν_A	Austenite Poisson's Ratio	0.33
3	E_M	Martensite elasticity (MPa)	18814
4	ν_M	Martensite Poisson's Ratio	0.33
5	ε^L	Transformation strain	0.0402
6	$(\delta\sigma/\delta T)_L$	$(\delta\sigma/\delta T)$ loading	6.4
7	σ_{tL}^S	Start of transformation loading	387
8	σ_{tL}^E	End of transformation loading	468
9	T_0	Reference Temperature	22
10	$(\delta\sigma/\delta T)_U$	$(\delta\sigma/\delta T)$ unloading	5
11	σ_{tU}^S	Start of transformation unloading	171
12	σ_{tU}^E	End of transformation unloading	122
13	σ_{cL}^S	Start of transformation loading (compression)	387

14	ε_V^L	Volumetric transformation strain	0
15	N_A	Numbers of annealing steps	0
16	N_{S1}	Step number for the annealing step	0
17	N_P	Number of pairs of plastic points	4
18-19	$\sigma_1^P, \varepsilon_1$	Stress Strain for point #1	1199.01 0.106248
20-21	$\sigma_2^P, \varepsilon_2$	Stress Strain for point #2	1232.39 0.108485
22-23	$\sigma_3^P, \varepsilon_3$	Stress Strain for point #3	1250.68 0.110348
24-25	$\sigma_4^P, \varepsilon_4$	Stress Strain for point #4	1266.61 0.11221

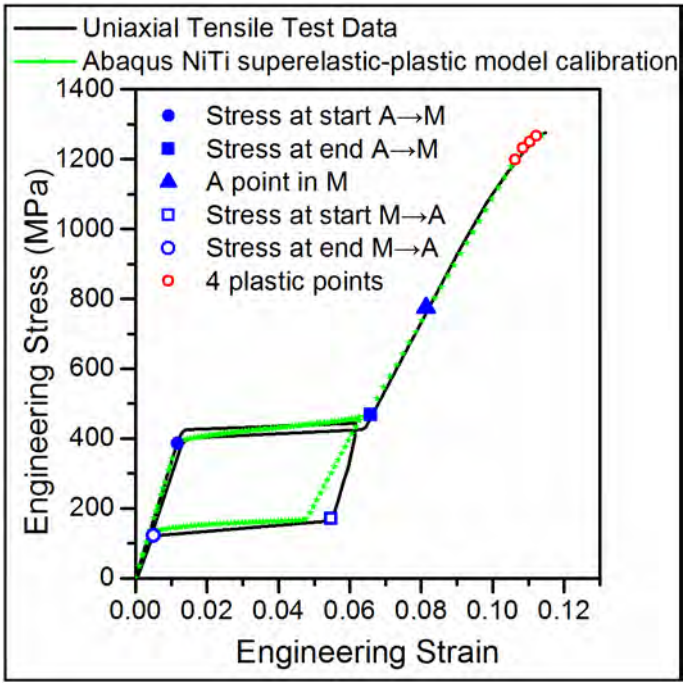

Figure 8-1: Calibration of the Nitinol superelastic-plastic material model. The stress-strain plot depicts the curve described by the calibrated material model in comparison with the test data curve. Four points are picked on the mechanical hysteresis, one point in the straight region of the curve above the 0.8% strain when material is in martensite phase and four points are picked in the plastic region before failure point.

Linear Viscoelastic Material Model

Self-expanding stents are delivered crimped into a catheter sheath of a small diameter. The crimping process may be influenced by the time-dependent viscoelastic nature of the material; therefore, for an accurate prediction of the stent's behaviour during crimping, a viscoelastic material model was implemented. The

steps used to define the linear viscoelastic material model were presented in Chapter 5, Section 5.1.

The elastic modulus on the loading step $E_A = 33013\ MPa$ and the Poisson's ratio $\nu_A = 0.33$ from Table 14 were used to define the instantaneous elastic behaviour part of the viscoelastic material definition. Equation 5.13 was used to compute the shear creep compliance based on the raw tensile creep data available in the literature (Raj and Noebe 2013) and the normalised data for each time reading was input into Abaqus material interface (Table 24 in Appendix 3.2). To calibrate the viscoelastic material model, Abaqus' "Evaluate" functionality which fits the creep test data to the Prony series was used. The Prony series terms representing the material parameters for the viscoelastic response were slotted into Equation 5.11 to obtain the time-dependent normalised shear relaxation modulus function (Equation 8.2). The curve fitting results are presented as creep compliance versus time and relaxation modulus versus time plots (Figure 8-2).

$$g(t) = 1 - \{0.0842276[1 - e^{(-t/26325)}]\} \qquad \textbf{Eq.8.1}$$

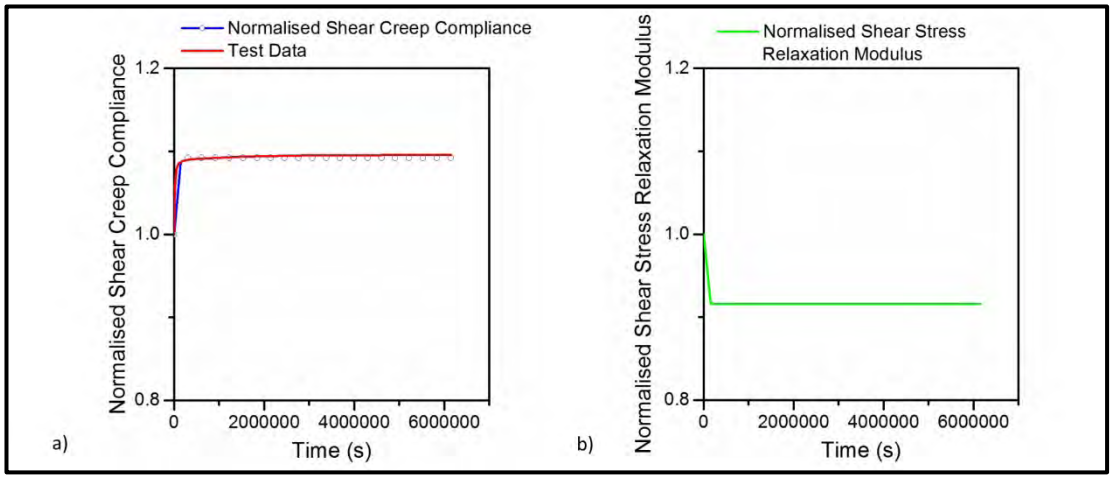

Figure 8-2: Calibration of the Abaqus viscoelastic material model using tensile creep test data on Nitinol wire and "Evaluate" function. a) FE normalised prediction of shear creep compliance compared with experimental data after conversion into shear creep b) Predicted normalised shear stress relaxation modulus extracted from Abaqus model.

Geometric Models

The braided stent model is created and discretized in pyFormex following the method presented in Chapter 5, Section 5.2.3. The crimping tool is modelled as an

Octagonal Crimper (Section 5.3.2). FE discretization of the stent model is presented in Table 15. The braided stent model is depicted in Figure 8-3 in the uncrimped and crimped configuration.

Table 15: Braided stent and crimping tool characteristics of the FE models.

	BRAIDED STENT	CRIMPING TOOL
ELEMENT TYPE	B31/B32	SFM3D4R
NUMBER NODES	6840/13680	278
NUMBER ELEMENTS	6840	139
CONNECTOR TYPE (NUMBER)	HINGE (360) & SLIDE-PLANE (60)	-

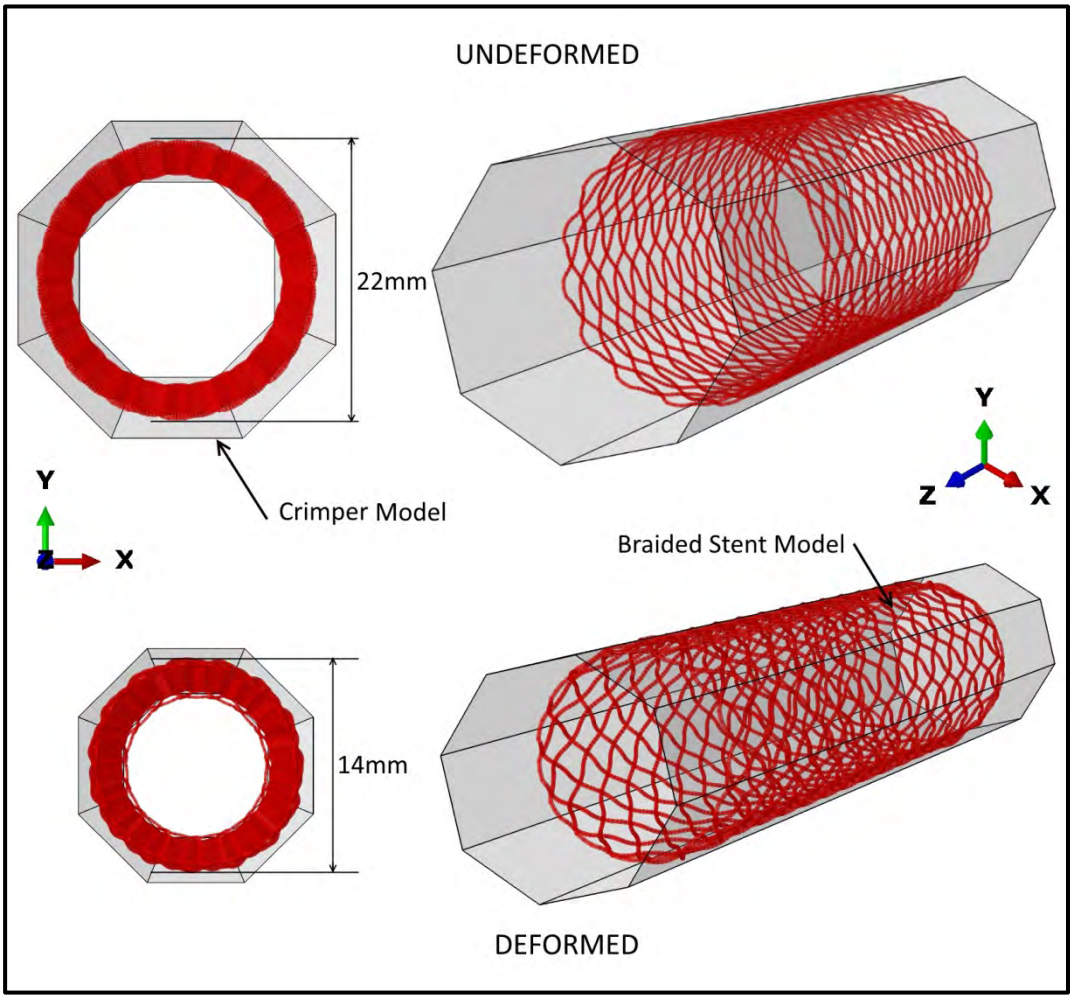

Figure 8-3: Braided stent and crimper FE models in undeformed and deformed configuration. The braided stent model was generated in pyFormex, while the crimper was modelled in Abaqus as a tubular deformable shell. Radial compression was performed by imposing a displacement boundary condition to the crimper.

The crimper geometry was modelled as a tubular deformable shell (Figure 8-3) with a length of 100 mm and an octagonal section with side of 9.15 mm (Section 5.3.2). The crimper's FE discretization is presented in Table 15. The inner surface of the crimper was specified to enable the contact modelling. A surface-to-surface type of contact was created with node to surface discretization defined between the outer node set and the inner surface of the crimper. A friction coefficient of 0.1 was assumed.

Radial Compression Simulation

The radial compression simulation was generated by imposing a displacement boundary condition to the crimper. Only one analysis step was implemented, with the load/unload cycle created through the use of a tabular amplitude. The radial forces - radial resistive forces and chronic outward forces were derived from the reaction forces opposing the radial displacements. Movement of the crimper in the axial direction was restricted by setting a displacement boundary condition on the crimper part, while the stent model was fixed centrally by imposing a displacement boundary condition on the node set created for this purpose. First half of the deformation history (0 – 80 sec) was concerned with crimping, process which led to a reduction of the crimper's internal diameter from 22 mm to 14 mm. The second half (81 – 160 sec), was concerned with the unloading, so that at the end of the simulation, the stent reverted to it nominal diameter of 22 mm. The stent-crimper assembly is shown in Figure 8-3. A radial compression simulation up to a diameter of 2 mm was also performed to analyse the fraction of martensite that was stress induced in the process. The percentage volume fraction of martensite was extracted from the node in the crown exhibiting maximum martensite transformation and was plotted against the stent's diameter.

8.3 Results

Figure 8-4a shows a comparison between the FE predictions of radial resistive forces and chronic outward forces of the Nitinol braided stent and the test data. The change in the stent's length in terms of diameter is shown in Figure 8-4b.

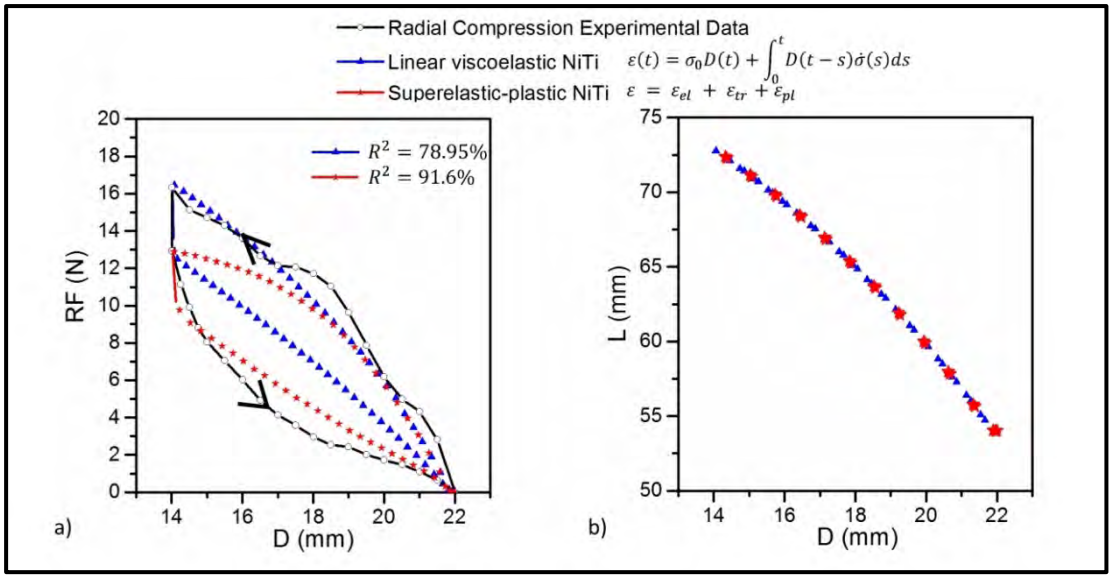

Figure 8-4: Validation of the Nitinol material models (FE model using B31 elements). a) FE predictions of the radial forces of the Nitinol braided stent in terms of diameter are compared against the radial compression test data b) Length vs. stent diameter during the crimping simulation.

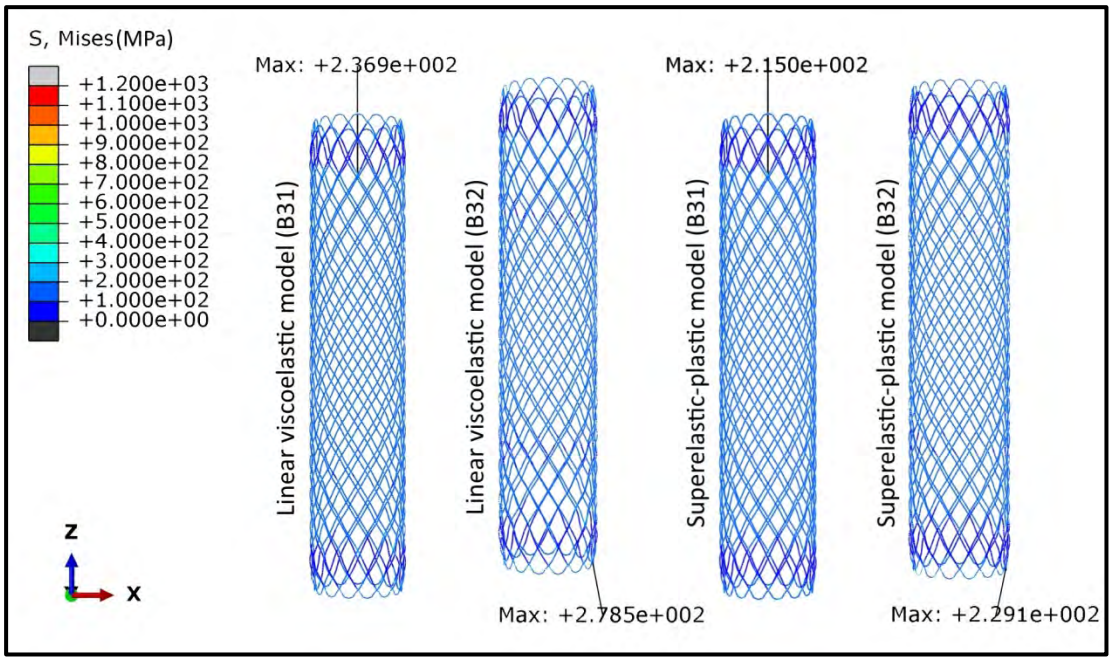

Figure 8-5: Contour plot of von Mises stress distribution for the stent FE model using the linear viscoelastic and the superelastic-plastic material models and B31, B32 elements.

Contour plots of von Mises stress distribution in the stent beams in the fully crimped state for both of the material models used can be depicted in Figure 8-5. A peak value of 236.9MPa was observed for the viscoelastic stent and a peak value of 215MPa was observed for the superelastic-plastic stent when using the B31 element

formulation. An increase of 15% in the magnitude of the peak stresses is observed when using the B32 element formulation coupled with the viscoelastic behaviour implementation, while only a 6% increase is observed in the case of the superelastic-plastic model.

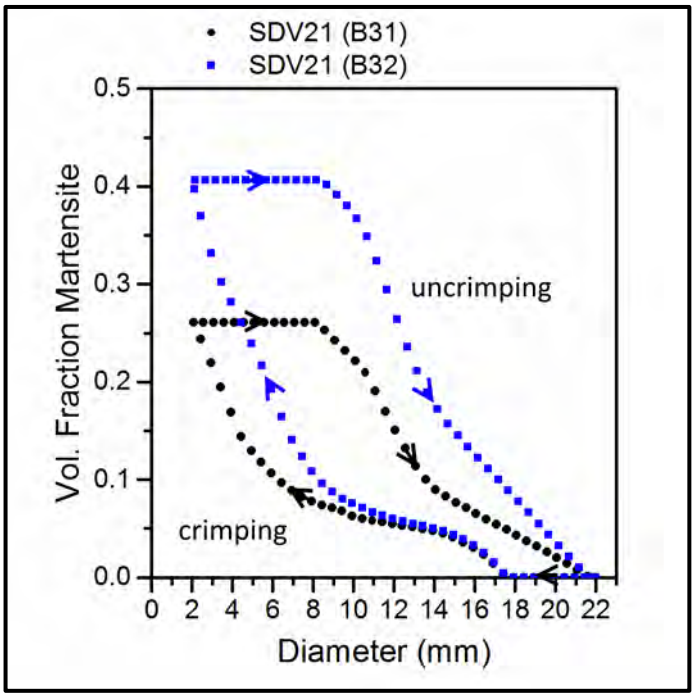

Figure 8-6: Fraction of martensite in the stent discretized with B31 and B32 elements respectively and subjected to crimping from a diameter of 22 mm to 2 mm. The volume fraction of martensite reaches 26% in the B31 formulation as oppose to 40% in the B32 element formulation.

Figure 8-6 depicts the volume fraction of martensite (SDV21) that is stress induced while the stent model discretized with B31 and B32 elements respectively is crimped from the initial diameter of 22 mm to a final diameter of 2 mm and uncrimped to the initial diameter. An upper and lower plateau of the martensite fraction is observed during the process.

8.4 Discussion

The R-squared values calculated to assess the goodness of fit for the two material models show a 78.95% variation for the viscoelastic model and a 91.6% variation for the superelastic-plastic model. Crimping and uncrimping paths create a hysteresis loop which is more pronounced in the experimental data curve. The viscoelastic model predicts the radial resistive forces more accurately than the superelastic-plastic

material model. However, the hysteresis loop is narrow. This observation leads to the conclusion that the stiffness of the viscoelastic stent model is higher than the stiffness of the stent prototypes. The superelastic-plastic model presents a wider hysteresis loop, closer to the experimental curve. The difference in stiffness may be attributed to the difference in the elastic moduli used in the material model characterisation. On the loading path, an elastic modulus of 33013MPa was used in both material models, leading to similar behaviour. However, on the unloading path, the superelastic-plastic model is more accurately calibrated than the viscoelastic model, by enabling an elastic modulus of 18814MPa, therefore, the model is less stiff leading to a lower chronic outward force closer to the experimental data. As seen in Figure 8-4b, the length of the stent as a function of diameter is independent of the material model used. This observation is in agreement with the analytical model for the braided stent described in Chapter 3, Section 3.1.

Peak stresses presented in Figure 8-5 are similar in magnitude. Using B32 element formulation leads to slightly higher peak values, occurrence which is in agreement with findings from the previous work in Chapter 6. Lowest stresses were observed at the second row of wire intersections, which can be attributed to the SLIDE-PLANE connectors used to model the wire intersections in this area. These connectors allow for slipping of the wires at the extremities of the stent model rather than rigidly fixing the nodes of the opposing, phenomenon which occurs where the HINGE connectors were used. The peak stresses were below the critical value required for A → M transformation and upon unloading, the plastic strain was zero and full recovery of the stent was predicted.

As seen in Figure 8-5, the martensite transformation started when stent was crimped below 18 mm in diameter and reached a maximum of 26% volume fraction when crimped at 2 mm diameter in the case of B31 element formulation. When using B32 elements, the martensite volume fraction showed a peak of 40%. It may be noted that the stresses during crimping never reach critical values that would lead to plastic deformation of the braided stent, therefore a superelastic material model would have been sufficient to predict the stent's behaviour. However, plastic deformation may occur when crimping a struts-based self-expanding stent formed by laser-cutting, in

which case the superelastic-plastic model would be useful at predicting a possible permanent deformation.

The stent design process can greatly benefit from this model implementation by predicting the smallest catheter diameter that would not lead to plastic deformation of the stent. R-squared values were computed for both models and overall, the superelastic-plastic model with an R-squared value of 91.6% is more efficient in capturing the crimping behaviour of the braided stent. However, when only the radial resistive forces are of interest, the viscoelastic model gives the best prediction with an R-squared of 96.87% as oppose to 90.34% in the case of the superelastic-plastic model.

8.5 Conclusion

In the present chapter, nonlinear FEA was used to evaluate two Nitinol material models: a viscoelastic and a superelastic-plastic material model. The effectiveness of the two models in capturing the complex mechanical behaviour of a self-expanded braided stent during crimping and uncrimping was compared. Radial resistive forces and chronic outward forces were considered as measures of the models' accuracy. Three experiments were performed including a uniaxial tensile test for capturing the superelastic-plastic behaviour of the Nitinol material, a DSC analysis to assess the transformation temperature range following the ageing treatment conducted on the Nitinol stent and a radial compression test performed on braided stent prototypes.

The results suggest that:

1. both material models can be used in capturing the stent's behaviour - when only the radial resistive forces are of interest, the viscoelastic model is the most accurate - when both loading and unloading steps are of interest, the superelastic-plastic model performs better;
2. ageing the Nitinol stent for 10 min at 450°C increases the A_f from 10°C to 29.57°C;
3. martensite formation is stress induced when crimping the braided structure below a diameter of 18 mm;

4. B31 and B32 beam elements are both suitable for modelling the wire in the braid.

The present study shows a good attempt at creating a viscoelastic model for Nitinol. However, in order to improve the accuracy of its predictions, more material characterisation experiments would be required, e.g. a stress relaxation test or a shear creep test performed on the Nitinol wire under investigation. Although the proposed material models are applied to a specific stent design, the present study is believed to be a step forward to better understand the complexity that Nitinol material creates in the engineering of implantable devices.

Chapter 9
Conclusions

9.1 Summary

In this chapter, the contributions of the work to the current state of knowledge are presented. The contributions are offered from the point of view of area of research, contributions to the methodology and to the finite element analysis strategy.

The literature reviewed presented in Chapter 2 showed little scientific effort in the area of braided SX stent. The FE studies carried out involved building FE models upon linear elastic material models in case of polymeric stents, or upon superelastic models in case of Nitinol braided stents. Some radial compression simulations were performed, however, they do not realistically reflect the crimping process a braided stent would be subjected to when using a crimping device. In this thesis, the main contribution to the area of research is in creating validated finite element models for the braided stent in order to investigate the mechanical behaviour of the stent subjected to crimping and to be able to identify the influence of implementing the viscoelastic behaviour in the material definition for Polydioxanone and Nitinol. Also in this chapter, there is an up-to-date classification of stents based on design and engineering characteristics, classification which gives an account of typical materials and current raw materials form, stent geometry and fabrication techniques. Also, an interpretation of the stent design criteria extending the knowledge regarding the four perspectives that must be addressed in order for a stent to be considered successful: safety, performance, deliverability and manufacturability.

In terms of contributions to the methodology, Chapter 3 presented a corrected version of the existing analytical model, which is adapted to include the braiding angle. The analytical model was also extended by introducing elements of mandrel design, braid cover factor and jamming conditions. The analytical study based on the Wahl's (1944) theory of mechanical springs as suggested by Jedwab and Clerc (1993) was carried out in order to determine equations that would help with computing elements of the braid geometry, with designing the mandrel required in the stent fabrication and with building the prototypes. Some mechanical properties of the stent subjected to axial loading and radial compression were also presented in this analytical model. The axial force, axial and radial stiffness and the equivalent stress were calculated in terms of braid angle. A step-by-step fabrication process of the single wire looped ends braided stent was also presented in this chapter. Stent prototypes were manually braided in-house using the PDO suture monofilament and medical grade Nitinol wire. The prototypes were braided from a single piece of wire in a diamond pattern in a seamless design.

Chapter 4 described the experimental techniques required in order to calibrate the materials models investigated. Tensile test and creep test data for the Polydioxanone material were made available. Similarly, in the case of the Nitinol wire under investigation, tensile test data and DSC test data were generated. Two mechanical tests performed in order to determine the mechanical properties of the PDO suture material: uniaxial tensile test and tensile creep test were presented in detail in this chapter. The short-term uniaxial tensile test helped in determining the instantaneous elastic modulus for the polymer, while the creep test was used to determine its viscoelastic, time-dependent behaviour. The test results were used to determine parameters for a viscoelastic material model and material constants for the Abaqus' Prony series. The radial force testing or stent crimping experiment was performed on the braided stent prototypes fabricated in house. A detailed description of the experiment and the technique used to capture raw data required for the calculation of radial force was presented as well. Material characterisation for Nitinol wire included performing a Discrete Scanning Calorimetry analysis and a uniaxial tensile test. The thermal analysis helped with identifying the new transformation temperature range of the material following the ageing treatment that the prototypes were subjected to.

The uniaxial tensile test was required to obtain the material constants needed in the calibration of the superelastic-plastic and viscoelastic material models.

The contributions to the Finite Element Analysis strategy for simulations involving braided stents are covered in Chapter 5. The step-by-step process required for creating and calibrating a viscoelastic material model in Abaqus was presented here. Stent crimping simulation is a very challenging non-linear quasi-static problem involving complex geometry and complex contact conditions. One of the reasons why lesser number of FE studies was carried out to date, is the complex geometry of the braided stent. CAD tools such as SolidWorks do not offer a parametrical approach to building braids, therefore making the process lengthy and tedious. A different approach to braid modelling by combining pyFormex with Abaqus was described in this chapter. The element formulation strategy employed the linear beam elements B31, which is the formulation of choice for the FE work in this area of research, but also the quadratic beam elements B32 to ensure high accuracy of the solution. In order to perform the crimping process, three different types of crimping tools were designed and the creation of their 3D geometrical models were presented. Contact modelling strategy led to the implementation of two types of contact interactions, depending on the type of crimper model used in the simulation: a general contact when the 8 plates crimper model was used and a surface-to-surface contact when an octagonal or a cylindrical crimper model was used. The stent crimping was based on a displacement driven simulation strategy, with the stent deformation obtained by imposing a specified displacement Boundary Condition (BC) to the crimper model.

Chapter 6, 7 and 8 described in detail the simulation strategies for the particular cases that are presented. In this study, the simulation strategy was to use Abaqus/Standard analysis in solving the problem and to create a mosaic of case scenarios using different solver controls, contact formulations, analysis types, element formulations and crimping tool models, in order to identify the combination that would lead to the most accurate solution without an impact on the solution cost.

FEA was used to compare the performance of the two braided stents: looped ends and open ends braided stent in Chapter 6. The analytical and FEA approach used in this chapter helped to better understand the mechanics of braided biotextiles and

provide a framework for stent design optimisation. The study showed that the looped ends and open ends designs have similar functionality with regards the radial forces and stresses developed in the middle of the device while the stent is subjected to crimping. However, the analytical model could not predict the radial forces and peak stresses of the looped ends braided stent. This study emphasises the effect of stent design to the mechanical behaviour of the braided stents.

Chapters 7 and 8 presented the development and calibration of linear viscoelastic models for PDO and Nitinol. The chapters present the predictive validation of the material models, including a comparison of simulated and experimental results of the crimping test. Though a linear elastic material model is most commonly used in determining the mechanical behaviour of polymeric braided stents subjected to loading, the numerical results can be prone to errors if the time-dependent nature of the material is ignored. The technique described in this thesis and presented in Chapter 7 was developed to take into account the viscoelastic nature of the material. FE was used to simulate the mechanical response of the viscoelastic material subjected to crimping and led to excellent agreement between the numerical simulations and the crimping experiments of the PDO stent. The most accurate prediction, with an R-squared of 94.4%, was generated by a FE model which had a linear viscoelastic material model implemented for the polymer. The Nitinol viscoelastic model was assessed in comparison to the superelastic-plastic model in Chapter 8 and both material models proved to be capable of capturing the stent's behaviour. With an R-squared of 96.87%, the viscoelastic model was the most accurate in capturing the radial resistive forces, while the superelastic-plastic model gave better prediction for the chronic outward forces. Overall, the superelastic-plastic model with an R-squared value of 91.6% is more efficient in capturing the crimping behaviour of the braided stent.

The feasibility of using a viscoelastic material model to model the time-dependent material behaviour was demonstrated and the effectiveness of using FEA research tool in the stent analysis was confirmed. pyFormex proved to be suitable in modelling the geometry of the braided stent. The methodology described in this paper can help engineers to better understand the mechanical behaviour of the viscoelastic braided stent and therefore to better optimise its design for particular

clinical applications. The work can be used to shorten the development cycle of stents by reducing the amount of in vitro testing and ultimately may help advance the state-of-the-art in both malignant and benign luminal obstruction management.

9.2 Testing the Hypotheses

The current research work has been carried out on the basis of the hypotheses outlined in Chapter 1, section 1.2.2. The research findings from work presented in Chapter 3 to Chapter 8 were used to test these hypotheses.

Hypothesis 1: The crimping process of a viscoelastic braided stent can be realistically modelled using commercial finite element analysis software.

This study has demonstrated that the viscoelastic braided stent can be realistically modelled using commercial finite element analysis software. Due to the high complexity of the geometry, the braided stent was modelled in pyFormex using a parametrical approach. The material models were created and calibrated in Abaqus and the crimping process was modelled successfully.

Hypothesis 2: The linear viscoelastic material model developed for a PDO braided stent shows an improvement in the accuracy of the stent's crimping behaviour in comparison to a purely elastic material model.

This study has confirmed the validity of this hypothesis. By using the linear viscoelastic material model, it was demonstrated that it is possible to predict an accurate behaviour of the PDO braided stent during the crimping and uncrimping. The simulation results showed a good agreement with the experiment and confirmed the effectiveness of using FEA research tool in the stent analysis. As shown in Chapter 7, the best prediction, with an R-squared of 94.4%, was observed in a crimping simulation which used a linear viscoelastic model for the stent material, an octagonal crimper and a displacement applied by tabular amplitude.

Hypothesis 3: The linear viscoelastic material model developed for a Nitinol braided stent shows an improvement in the accuracy of the stent's crimping behaviour in comparison to a superelastic-plastic material model.

This study has found that the linear viscoelastic model gives the best prediction only of the radial resistive forces. An R-squared of 96.87% during the crimping step has been reported in Chapter 8. However, during the uncrimping step, the hypothesis is not valid. Overall, the superelastic-plastic model with an R-squared value of 91.6% is more efficient in capturing the crimping behaviour of the braided stent.

9.3 Future Work

The findings of this thesis can be used to further the research in some areas that are outlined below.

Although the linear viscoelastic model in the case of a polymeric braided stent proved to be more accurate than a purely elastic model developed for this material, the difference in response in minimal. The accuracy of the model could benefit from a customised implementation of the viscoelastic constitutive equation. The viscoelastic material model could be further developed by incorporating temperature effects and biodegradability.

Both viscoelastic models created for the PDO and Nitinol braided stent showed a higher stiffness in the uncrimping step in comparison with the experimental data. This behaviour might be due to the type of connector element used to model the wire intersections. It would be interesting to investigate this further to identify an element type or implement the interlocking of wires in a different way in a quest to further improve the accuracy of the model.

An interesting area that could be investigated is the stent deployment inside the target lumen. The crimping and uncrimping processes investigated in this thesis were performed at room temperature. In contrast, stent deployment occurs at body temperature; therefore, FEA using a viscoelastic braided stent model would be very helpful for the design engineers in understanding the impact that the test temperature has on the chronic outward forces that are imparted to the lumen. For this purpose, it would be valuable to perform a series of deployment simulations monitoring the radial forces, the stresses that occur in the stent beams at the tip of the catheter and the stresses imparted to the lumen host.

Chapter 10 References

Abaqus (2004) 'UMAT for Superelasticity of shape memory alloys Output from UMAT / Superelasticity', *Main*, (August).

Abaqus Inc (2014) 'Analysis 6.14 User's Guide', III: MATER, 294.

Abbott Vascular (2017) MULTI-LINK ULTRA Coronary Stent System [online], available: http://www.abbottvascular.com/us/products/coronary-intervention/multi-link-ultra.html [accessed 29 May 2017].

Adanur, S. (1995) *Wellington Sears Handbook of Industrial Textiles*, Technocomic Publishing Company, Inc.: Lancaster, Pennsylvania, US.

Alger, M.S.M. (1996) *Polymer Science Dictionary*, 2nd ed, Chapman & Hall: London.

Ashby, M.F., Jones, D.R.H. (1994) *Engineering Materials 2 : An Introduction to Microstructures, Processing and Design*, Pergamon.

Auricchio, F., Conti, M., De Beule, M., De Santis, G., Verhegghe, B. (2011) 'Carotid artery stenting simulation: from patient-specific images to finite element analysis.', *Medical engineering & physics*, 33(3), 281–9.

Auricchio, F., Taylor, R.L. (1997) 'Shape-memory alloys: modelling and numerical simulations of the finite-strain superelastic behavior', *Computer Methods in Applied Mechanics and Engineering*, 143(1–2), 175–194.

Auricchio, F., Taylor, R.L., Lubliner, J. (1997) 'Shape-memory alloys: macromodelling and numerical simulations of the superelastic behavior', *Computer Methods in Applied Mechanics and Engineering*, 146(3–4), 281–312.

Baer, G.M., Small, W., Wilson, T.S., Benett, W.J., Matthews, D.L., Hartman, J., Maitland, D.J. (2007) 'Fabrication and in vitro deployment of a laser-activated shape memory polymer vascular stent.', *Biomedical engineering online*, 6, 43.

Balossino, R., Gervaso, F., Migliavacca, F., Dubini, G. (2008) 'Effects of different stent designs on local hemodynamics in stented arteries', *Journal of Biomechanics*, 41(5), 1053–1061.

Bataillard, L., Bidaux, J.E., Gotthardt, R. (1998) 'Interaction between microstructure and multiple-step transformation in binary NiTi alloys using in-situ transmission electron microscopy observations', *Philosophical Magazine A*, 78(2), 327–44.

Behl, M., Lendlein, A. (2007) 'Shape-memory polymers', *Materials Today*, 10(4), 20–28, available: http://linkinghub.elsevier.com/retrieve/pii/S1369702107700470.

Ben-Dor, I., Waksman, R., Pichard, A.D., Lindsay, J., Satler, L.F. (2011) 'The Current Role of Bare-Metal Stents', *Cardiac Interventions Today*, (February), 40–46.

De Beule, M. (2008) *Finite Element Stent Design (PhD Thesis)*, Ghent, Belgium.

De Beule, M., Van Cauter, S., Mortier, P., Van Loo, D., Van Impe, R., Verdonck, P., Verhegghe, B. (2009) 'Virtual optimization of self-expandable braided wire stents.', *Medical engineering & physics*, 31(4), 448–53, available: http://www.ncbi.nlm.nih.gov/pubmed/19117791 [accessed 12 Jun 2014].

De Beule, M., Impe, R. Van, Verdonck, P., Verhegghe, B. (2007) 'Finite element stent design', *Symposium FEA U Gent BE*, 4–5.

De Beule, M., Mortier, P., Santis, G. De, Conti, M., Segers, P., Verdonck, P., Verhegghe, B. (2009) 'A Virtual Product Development Strategy for Minimally Invasive Medical Devices', in *2009 SIMULIA Customer Conference*, 19–27.

De Beule, M., Mortier, P., Santis, G. De, Conti, M., Segers, P., Verdonck, P.,

Verhegghe, B. (2010) 'A Virtual Product Development Strategy for Minimally Invasive Medical Devices', *Trends Biomater. Artif. Organs*, 24(1), 19–26.

Blausen.com Staff (2014) 'Blausen gallery 2014', *Wikiversity Journal of Medicine*, 1(2).

Bonsignore, C. (2003) 'A Decade of Evolution in Stent Design', in Pelton, A.R. and Duerig, T., eds., *Proceedings of the International Conference on Shape Memory and Superelastic Technologies, SMST-2003*, Pacific Grove, California, USA.

Boston Scientific (2014) Ultraflex [online], available: https://www.bostonscientific.com/content/dam/bostonscientific/endo/portfolio-group/ultraflex-transbronchial-stent/ENDO-274113-AA_Ultraflex Brochure_FINAL.pdf [accessed 22 Nov 2016].

Boston Scientific (2015) 2015 Peripheral Interventions Product Catalog [online], available: http://www.bostonscientific.com/content/dam/bostonscientific/pi/portfolio-group/resources/ProductCatalog/PI-2015-Product-Catalog-StentsVasc-and-NonVasc.pdf/ [accessed 27 Jan 2017].

Boylan, J.F. (2003) 'The Development of Radiopaque nitinol', in *Proc of the International Conf on Shape Memory and Superelastic Technologies*, Pacific Grove, CA, US, 1–6.

Boylan, J.F., Cox, D.L., Kramer-Brown, P.A. (2006) 'Radiopaque and MRI compatible nitinol alloys for medical devices'.

Briguori, C., Sarais, C., Pagnotta, P., Liistro, F., Montorfano, M., Chieffo, A., Sgura, F., Corvaja, N., Albiero, R., Stankovic, G., Toutoutzas, C., Bonizzoni, E., Di Mario, C., Colombo, A. (2002) 'In-stent restenosis in small coronary arteries: impact of strut thickness.', *Journal of the American College of Cardiology*, 40(3), 403–9.

Brinson, H.F., Brinson, L.C. (2008) *Polymer Engineering Science and Viscoelasticity - An Introduction*, Springer Science+Business Media, LLC.

Canic, S., Ravi-Chandar, K., Krajcer, Z., Mirkovic, D., Lapin, S. (2005) 'Mathematical Model analysis of Wallstent and Aneurx: dynamic responses of bare-metal endoprosthesis compared with those of stent-graft.', *Texas Heart Institute journal / from the Texas Heart Institute of St. Luke's Episcopal Hospital, Texas Children's Hospital*, 32(4), 502–506.

Carr, S. (2011) *The Development of a Radiopaque Nitinol Alloy: Radiopacity and Thermodynamic Stability*.

Chovan, D., Nolan, M., Tofail, S. a. M. (2015) 'First principles simulations of elastic properties of radiopaque NiTiPt', *Journal of Alloys and Compounds*, 630, 54–59.

Clerc, C.O., Jedwab, M.R., Mayer, D.W., Thompson, P.J., Stinson, J.S. (1997) 'Assessment of wrought astm f1058 cobalt alloy properties for permanent surgical implants', *Journal of Biomedical Material Research*, 38, 229–34.

Conti, M. (2007) *Finite Element Analysis of Self-Expanding Braided Wirestent (MSc Thesis)*, University of Ghent: Ghent, Belgium.

Cook Medical (1987) Gianturco-Roubin Flex Stent [online], *Angioplasty.org*, available: http://www.ptca.org/news/2013/0701_COOK.html [accessed 29 May 2017].

Cook Medical (2013a) Formula 418 Biliary BX Stent [online], available: https://www.cookmedical.com/data/resources/PI-BUSM-F418BMP-EN-201301_M3.pdf [accessed 31 May 2016].

Cook Medical (2013b) Zilver Biliary SX Stent [online], available: https://www.cookmedical.com/data/resources/ESC-WM-50138-EN-201306_ZILVER.pdf [accessed 31 May 2016].

Cook Medical (2013c) Evolution Esophageal Stent [online], available: https://www.cookmedical.com/data/resources/ESC-WM-50062-EN-201306.pdf [accessed 31 May 2016].

Corbman, B.P. (1983) *Textiles: Fiber to Fabric*, 6th, Inter ed, McGraw-Hill, Inc.: New

York.

Courtney, T.H. (2005) *Mechanical Behavior of Materials*, 2nd ed, Waveland Press: Long Grove, Illinois, US.

Covidien (2015) EverFlex Biliary Stent [online], available: https://www.ev3.net/peripheral/us/se-biliary-stents/protg-everflex-selfexpanding-biliary-stent-system.htm [accessed 29 May 2017].

Dieter, G.E. (1961) 'Yielding Criteria for Ductile Metals', in Mehl, R.. and Bever, M.B., eds., *Mechanical Metallurgy*, McGraw-Hill Book Company, 646.

Dotter, C.T., Buschmann, P.A.C., McKinney, M.K., Rosch, J. (1983) 'Transluminal expandable nitinol coil stent grafting: preliminary report', *Radiology*, 147, 259–60.

Dotter, C.T., Judkins, M.P. (1964) 'Transluminal Treatment of Arteriosclerotic Obstruction: Description of a New Technic and a Preliminary Report of Its Application', *Circulation*, 30(5), 654–670, available: http://circ.ahajournals.org/cgi/doi/10.1161/01.CIR.30.5.654 [accessed 30 Apr 2015].

Duda, S.H., Wiskirchen, J., Tepe, G., Bitzer, M., Kaulich, T.W., Stoeckel, D., Claussen, C.D. (2000) 'Physical properties of endovascular stents: an experimental comparison.', *Journal of vascular and interventional radiology : JVIR*, 11(5), 645–654.

Duerig, T., Pelton, A. (2002) 'An Overview of Superelastic Stent Design', *Materials Science Forum*, 394–395, 1–8.

Duerig, T., Pelton, A., Stockel, D. (1999) 'An overview of nitinol medical applications', *Materials Science and Engineering*, A273-275, 149–160.

Duerig, T.W., Melton, K.N., Stöckel, D. (1990) *Engineering Aspects of Shape Memory Alloys*, Elsevier Ltd.

Duerig, T.W., Wholey, M. (2002) 'A comparison of balloon- and self-expanding

stents', *Min Invas Ther & Allied Technol*, 11(4), 173–178.

Dyet, J.F., Watts, W.G., Ettles, D.F., Nicholson, a a (2000) 'Mechanical properties of metallic stents: how do these properties influence the choice of stent for specific lesions?', *Cardiovascular and interventional radiology*, 23(1), 47–54.

Frost, M., Sedlák, P., Kruisová, A., Landa, M. (2014) 'Simulations of Self-Expanding Braided Stent Using Macroscopic Model of NiTi Shape Memory Alloys Covering R-Phase', *Journal of Materials Engineering and Performance*.

Gall, K., Yakacki, C.M., Liu, Y., Shandas, R., Willett, N., Anseth, K.S. (2005) 'Thermomechanics of the shape memory effect in polymers for biomedical applications', *Journal of Biomedical Materials Research Part A*, 73A(3), 339–348.

Garasic, J.M., Edelman, E.R., Squire, J.C., Seifert, P., Williams, M.S., Rogers, C. (2000) 'Stent and artery geometry determine intimal thickening independent of arterial injury', *Circulation*, 101, 812–8.

Grube, E., Sonoda, S., Ikeno, F., Honda, Y., Kar, S., Chan, C., Gerckens, U., Lansky, A.J., Fitzgerald, P.J. (2004) 'Six- and Twelve-Month Results From First Human Experience Using Everolimus-Eluting Stents With Bioabsorbable Polymer', *Circulation*, 109(18), 2168–2171.

Guagliumi, G., Sirbu, V., Musumeci, G., Bezerra, H.G., Aprile, A., Kyono, H., Fiocca, L., Matiashvili, A., Lortkipanidze, N., Vassileva, A., Popma, J.J., Allocco, D.J., Dawkins, K.D., Valsecchi, O., Costa, M.A. (2010) 'Strut coverage and vessel wall response to a new-generation paclitaxel-eluting stent with an ultrathin biodegradable abluminal polymer: Optical Coherence Tomography Drug-Eluting Stent Investigation (OCTDESI)', *Circ Cardiovasc Interv*, 3(4), 367–375.

Hager, M.D., Bode, S., Weber, C., Schubert, U.S. (2015) 'Shape memory polymers: Past, present and future developments', *Progress in Polymer Science*.

Hall, G.J., Kasper, E.P. (2006) 'Comparison of Element Technologies for Modeling Stent Expansion', *Journal of Biomechanical Engineering*, 128(5), 751.

Healthwise Inc. (2016) Peripheral Vascular Stenting [online], available: https://myhealth.alberta.ca/Health/tests-treatments/_layouts/15/healthwise/media/medical/hw/h9991299_004.jpg [accessed 29 May 2017].

Hetrick, K. (2009) 'Laser Processing in Stent Production', *Today's Medical Developments for Design, Manufacturing and Assembly of Medical Equipment and Devices*, (May).

Hitov, J.J., Rainer, W.C., Redding, E.M., Sloan, A.W., Stewart, W.D. (1964) 'Polyethylene product and process (US Patent 3144398A)'.

Honda, Y., Fitzgerald, P.J. (2003) 'Stent thrombosis: An issue revisited in a changing world', *Circulation*, 108(1), 2–5.

Hu, J., Zhu, Y., Huang, H., Lu, J. (2012) 'Recent advances in shape-memory polymers: Structure, mechanism, functionality, modeling and applications', *Progress in Polymer Science*, 37(12), 1720–1763.

Isayama, H., Nakai, Y., Hamada, T., Yamamoto, N., Koike, K. (2015) 'Development of an ideal self-expandable metallic stent design', *Gastrointestinal Intervention*, 4(1), 46–49.

Isayama, H., Nakai, Y., Toyokawa, Y., Togawa, O., Gon, C., Ito, Y., Yashima, Y., Yagioka, H., Kogure, H., Sasaki, T., Arizumi, T., Matsubara, S., Yamamoto, N., Sasahira, N., Hirano, K., Tsujino, T., Toda, N., Tada, M., Kawabe, T., Omata, M. (2009) 'Measurement of radial and axial forces of biliary self-expandable metallic stents.', *Gastrointestinal endoscopy*, 70(1), 37–44.

ISO (2002) 'ISO 10993-4:2002/Amd 1:2006 Biological evaluation of medical devices Part 4: Selection of tests for interactions with blood'.

ISO (2009a) 'ISO 10993-1:2009 Biological evaluation of medical devices Part 1: Evaluation and testing in the risk management process'.

ISO (2009b) 'ISO 10993-5:2009 Biological evaluation of medical devices Part 5: Tests

for in vitro cytotoxicity'.

Jamshidi, P., Mahmoody, K., Erne, P. (2008) 'Covered stents: a review.', *International journal of cardiology*, 130(3), 310–8.

Jedwab, M.R., Clerc, C.O. (1993) 'A study of the Geometrical and Mechanical Properties of Self-Expanding metallic Stent-Theory and Experiment', *Journal of applied biomaterials*, 4(1), 77.

Kandzari, D.E., Leon, M.B., Popma, J.J., Fitzgerald, P.J., O'Shaughnessy, C., Ball, M.W., Turco, M., Applegate, R.J., Gurbel, P. a., Midei, M.G., Badre, S.S., Mauri, L., Thompson, K.P., LeNarz, L. a., Kuntz, R.E. (2006) 'Comparison of Zotarolimus-Eluting and Sirolimus-Eluting Stents in Patients With Native Coronary Artery Disease. A Randomized Controlled Trial', *Journal of the American College of Cardiology*, 48(12), 2440–2447.

Kastrati, A., Mehilli, J., Dirschinger, J., Dotzer, F., Schuhlen, H., Neumann, F.-J., Fleckenstein, M., Pfafferott, C., Seyfarth, M., Schomig, A. (2001) 'Intracoronary Stenting and Angiographic Results : Strut Thickness Effect on Restenosis Outcome (ISAR-STEREO) Trial', *Circulation*, 103(23), 2816–2821, available: http://circ.ahajournals.org/cgi/doi/10.1161/01.CIR.103.23.2816.

Kastrati, A., Schömig, A., Dirschinger, J., Mehilli, J., von Welser, N., Pache, J., Schühlen, H., Schilling, T., Schmitt, C., Neumann, F.J. (2000) 'Increased risk of restenosis after placement of gold-coated stents: results of a randomized trial comparing gold-coated with uncoated steel stents in patients with coronary artery disease', *Circulation*, 101(21), 2478–83.

Kemp, T., Ritchey, J. (2011) 'Testing of Stents and Stent Materials (Instron)'.

Khennane, A. (2013) 'Introduction to Finite Element Analysis Using MATLAB® and Abaqus'.

Kim, J.H., Kang, T.J., Yu, W.-R. (2008) 'Mechanical modeling of self-expandable stent fabricated using braiding technology.', *Journal of biomechanics*, 41(15), 3202–12.

Kim, J.H., Kang, T.J., Yu, W.-R. (2010) 'Simulation of mechanical behavior of temperature-responsive braided stents made of shape memory polyurethanes.', *Journal of biomechanics*, 43(4), 632–43.

Ko, F.K. (1987) 'Braiding', in Dostal, C.A., Woods, M.S., Frissell, H.J. and Ronke, A.W., eds., *Engineered Materials Handbook. Vol.1, Composites*, ASM International: USA, 519–28.

Kozarek, R., Baron, T., Song, H. (2013) *Self-Expandable Stents in the Gastrointestinal Tract*, Springer Science & Business Media: New York.

Kumbar, S., Laurencin, C., Deng, M. (2014) *Natural and Synthetic Biomedical Polymers*, 1st ed, Newnes, Elsevier.

Lagoudas, D.C. (Ed.) (2008) *Shape Memory Alloys: Modeling and Engineering Applications*, Springer Science+Business Media, LLC: New York.

Lally, C., Dolan, F., Prendergast, P.J. (2005) 'Cardiovascular stent design and vessel stresses: a finite element analysis.', *Journal of biomechanics*, 38(8), 1574–81.

Lally, C., Kelly, D.J., Prendergast, P.J. (2006) 'Stents', *Wiley Encyclopedia of Biomedical Engineering*, (APRIL 2006).

Lau, K.-W., Mak, K.-H., Hung, J.-S., Sigwart, U. (2004) 'Clinical impact of stent construction and design in percutaneous coronary intervention.', *American heart journal*, 147(5), 764–773.

Liu, C., Qin, H., Mather, P.T. (2007) 'Review of progress in shape-memory polymers', *Journal of Materials Chemistry*, 17(16), 1543.

Liu, G.H. (2006) 'Radial Compressive Properties of the Biodegradable Braided Regeneration Tubes for Peripheral Nerve Repair', *Journal of Industrial Textiles*, 36(1), 35–46.

Liu, Y., Du, H., Liu, L., Leng, J. (2014) 'Shape memory polymers and their composites in aerospace applications: a review', *Smart Materials and Structures*, 23(2), 23001.

Love, A.E.H. (1927) *A Treatise on the Mathematical Theory of Elasticity*, 4th ed, Dover Publications: New York.

Ma, D., Dargush, G.F., Natarajan, S.K., Levy, E.I., Siddiqui, A.H., Meng, H. (2012) 'Computer modeling of deployment and mechanical expansion of neurovascular flow diverter in patient-specific intracranial aneurysms.', *Journal of biomechanics*, 45(13), 2256–63.

MatWeb (2016) Special Metals Nitinol High-Strength Superelastic Ni-Ti Alloy [online], *MatWeb*, available: http://www.matweb.com/search/DataSheet.aspx?MatGUID=7bf10705e0494dfbbc07626e82729b04 [accessed 23 May 2017].

MatWeb (2017a) Polydioxanone [online], available: http://www.matweb.com/search/datasheet.aspx?matguid=5b60d08220b0478d907177140962ed19&ckck=1 [accessed 23 May 2017].

MatWeb (2017b) AISI Type 316L Stainless Steel, Annealed Sheet [online], available: http://www.matweb.com/search/datasheet.aspx?matguid=1336be6d0c594b55afb5ca8bf1f3e042&n=1 [accessed 23 May 2017].

MatWeb (2017c) Carpenter MP35N Ni-Co-Cr-Mo Alloy, 65% Cold Reduction [online], available: http://www.matweb.com/search/datasheet.aspx?matguid=64f260df11094625b18d000211deedb8 [accessed 23 May 2017].

MatWeb (2017d) Phynox Cobalt-Chromium-Nickel Alloy [online], available: http://www.matweb.com/search/datasheet.aspx?matguid=6fba14a928fe4b0aaa14478c28cbc423 [accessed 23 May 2017].

McGrath, D.J., O'Brien, B., Bruzzi, M., Kelly, N., Clauser, J., Steinseifer, U., McHugh, P.E. (2016) 'Evaluation of cover effects on bare stent mechanical response', *Journal of the Mechanical Behavior of Biomedical Materials*, 61, 567–580.

McKeen, L.W. (2014) *Plastics Used in Medical Devices*, Handbook of Polymer Applications in Medicine and Medical Devices, Elsevier Inc.

Medtronic Vascular (2003) Advantages of Cobalt Alloy for Coronary Stents [online], available: http://wwwp.medtronic.com/newsroom/content/1110132739468.pdf [accessed 24 Jul 2015].

Miyazaki, S., Otsuka, K. (1986) 'Deformation and transition behavior associated with the R-phase in Ti-Ni alloys', *Metallurgical Transactions A*, 17(1), 53–63.

Mondal, S., Hu, J.L. (2006) 'Temperature stimulating shape memory polyurethane for smart clothing', *Indian Journal of Fibre and Textile Research*, 31(1), 66–71.

Mortier, P. (2010) *Computer Modelling of Coronary Bifurcation Stenting (PhD Thesis)*, University of Ghent: Ghent, Belgium.

MPT Europe (2014) *Radial Force Tester Operation on Single Column Zwick*, NUI Galway, Galway.

Muliana, A., Rajagopal, K.R. (2012) 'Modeling the response of nonlinear viscoelastic biodegradable polymeric stents', *International Journal of Solids and Structures*, 49(7–8), 989–1000.

Ni, X.-Y., Pan, C.-W., Gangadhara Prusty, B. (2014) 'Numerical investigations of the mechanical properties of a braided non-vascular stent design using finite element method', *Computer methods in biomechanics and biomedical engineering*, (May 2014), 1–9.

Nolan, B.W., Schermerhorn, M.L., Powell, R.J., Rowell, E., Fillinger, M.F., Rzucidlo, E.M., Wyers, M.C., Whittaker, D., Zwolak, R.M., Walsh, D.B., Cronenwett, J.L. (2005) 'Restenosis in gold-coated renal artery stents', *Journal of Vascular Surgery*, 42(1), 40–46.

Nuutinen, J.-P., Clerc, C., Reinikainen, R., Törmälä, P. (2003) 'Mechanical properties and in vitro degradation of bioabsorbable self-expanding braided stents.', *Journal of biomaterials science. Polymer edition*, 14(3), 255–266.

Pache, J. ürge., Kastrati, A., Mehilli, J., Schühlen, H., Dotzer, F., Hausleiter, J. ör.,

Fleckenstein, M., Neumann, F.-J., Sattelberger, U., Schmitt, C., Müller, M., Dirschinger, J., Schömig, A. (2003) 'Intracoronary stenting and angiographic results: strut thickness effect on restenosis outcome (ISAR-STEREO-2) trial', *Journal of the American College of Cardiology*, 41(8), 1283–1288.

Peirlinck, M. (2013) *Design of Biodegradable Esophageal Stents (PhD Thesis)*, University of Ghent: Ghent, Belgium.

Pelton, A.R., DiCello, J., Miyazaki, S. (2000) 'Optimization of Processing and Properties of Medical - Grade Nitinol Wire', in Russell, S. and Pelton, A., eds., *Proceedings of the Int'l Conference on Shape Memory and Superelastic Technologies SMST-2000*.

Pelton, a R., Schroeder, V., Mitchell, M.R., Gong, X.-Y., Barney, M., Robertson, S.W. (2008) 'Fatigue and durability of Nitinol stents.', *Journal of the mechanical behavior of biomedical materials*, 1(2), 153–64.

Perrone, R.J. (1967) 'Heat-shrinkable Articles made from Silicone Rubber Polyethylene Compositions (US Patent 3326869)'.

Poncet, P.P. (2000) Nitinol Medical Device Design Considerations [online], available: http://memry.com/sites/default/files/documents/Nitinol_Medical_Device_Considerations_SMST00.pdf [accessed 2 Nov 2015].

Raj, S. V., Noebe, R.D. (2013) 'Low temperature creep of hot-extruded near-stoichiometric NiTi shape memory alloy part I: Isothermal creep', *Materials Science and Engineering A*, 581, 145–153, available: http://dx.doi.org/10.1016/j.msea.2013.04.040.

Rebelo, N., Gong, X.-Y., Connally, M. (2003) 'Finite Element Analysis of Plastic Behavior in Nitinol', *International Conference on Shape Memory and Superelastic Technologies, Proceedings on*, 501–507.

Ring, M. (2001) 'How a Dentist's Name Became a Synonym for a Life-saving Device: The Story of Dr. Charles Stent', *Journal of the History of Dentistry*, 49(2), 77–80.

ROFIN (2014) The Future of Medical Manufacturing - Laser Solutions For The Medical Device Technology [online], available: https://www.rofin.com/fileadmin/user_upload/content/6_branchen/10_medizintechnik/COHERENT_ROFIN_Bro_Medical_E_2016-12_BI_web.pdf [accessed 14 Oct 2015].

Rousseau, H., Puel, J., Joffre, F., Sigwart, U., Duboucher, C., Imbert, C., Knight, C., Kropf, L., Wallsten, H. (1987) 'Self-expanding endovascular prosthesis: an experimental study', *Radiology*, 164(3), 709–14.

Schatz, R.A. (1989) 'A view of vascular stents', *Circulation*, 79(2), 445–457.

De Scheerder, I., Wang, K., Sohier, J., Verbeken, E., Zhou, X.R., Frooyen, L., Van Humbeeck, J., Van de Werf, F. (1998) 'Metallic surface treatment using electrochemical polishing decreases thrombogenicity and neointimal hyperplasia after coronary stent implantation in a porcine model', *Journal of the American College of Cardiology*, 31(s1), 277.

Schillinger, M., Sabeti, S., Loewe, C., Dick, P., Amighi, J., Mlekusch, W., Schlager, O., Cejna, M., Lammer, J., Minar, E. (2006) 'Balloon Angioplasty versus Implantation of Nitinol Stents in the Superficial Femoral Artery', *The New England Journal of Medicine*, 354(18), 1879–1888.

Sedlák, P., Frost, M., Benešová, B., Ben Zineb, T., Šittner, P. (2012) 'Thermomechanical model for NiTi-based shape memory alloys including R-phase and material anisotropy under multi-axial loadings', *International Journal of Plasticity*, 39, 132–151.

Serruys, P.W., Sianos, G., Abizaid, A., Aoki, J., den Heijer, P., Bonnier, H., Smits, P., McClean, D., Verheye, S., Belardi, J., Condado, J., Pieper, M., Gambone, L., Bressers, M., Symons, J., Sousa, E., Litvack, F. (2005) 'The effect of variable dose and release kinetics on neointimal hyperplasia using a novel paclitaxel-eluting stent platform: the Paclitaxel In-Stent Controlled Elution Study (PISCES).', *Journal of the American College of Cardiology*, 46(2), 253–60.

Simonds, A.K., Irving, J.D., Clarke, S.W., Dick, R. (1989) 'Use of expandable metal stents in the treatment of bronchial obstruction', *Thorax*, 44(May), 680–681.

Simpson, J.A., Boylan, J.F. (2013) 'Radiopaque markers comprising binary alloys of titanium (US Patent 8500786 B2)'.

Singapore National Defence R&D Organisation DSO (2012) *Delivering Systems*, The Pride Within.

Small, IV, W., Singhal, P., Wilson, T.S., Maitland, D.J. (2010) 'Biomedical applications of thermally activated shape memory polymers', *Journal of Materials Chemistry*, 20(17), 3356.

Stoeckel, D., Bonsignore, C., Duda, S., Dunitz, M. (2002) 'A survey of stent designs.', *Minimally invasive therapy & allied technologies : MITAT : official journal of the Society for Minimally Invasive Therapy*, 11(4), 137–47.

Stoeckel, D., Pelton, A., Duerig, T. (2003) 'Self-expanding nitinol stents: material and design considerations.', *European Radiology*.

Sugioka, K., Cheng, Y. (2014) 'Ultrafast lasers—reliable tools for advanced materials processing', *Light: Science & Applications*, 3(4), e149.

Tanigawa, N., Sawada, S., Kobayashi, M. (1995) 'Reaction of the aortic wall to six metallic stent materials', *Academic Radiology*, 2(5), 379–84.

Tanous, A.C. (2010) Laser Cutting Takes the Heat out of Stent Manufacturing - Industrial Laser Solutions [online], available: http://www.industrial-lasers.com/articles/2010/01/-laser-cutting-takes.html [accessed 14 Oct 2015].

US Department of Health & Human Services Food and Drug Administration (1993) *Premarket Approval Application (PMA: P910030) for Gianturco-Roubin Flex-StentN Coronary Stent*.

US Department of Health & Human Services Food and Drug Administration (2010) 'Guidance for Industry and FDA Staff - Non-Clinical Engineering Tests and Recommended Labeling for Intravascular Stents and Associated Delivery

Systems'.

US Department of Health & Human Services National Heart Lung and Blood Institute (2013) Carotid Artery Stenting [online], *Wikipedia, The Free Encyclopedia*, available: https://en.wikipedia.org/wiki/Carotid_stenting#/media/File:Cad_stentplacement.jpg [accessed 5 Sep 2015].

Verhegghe, B. (2013) 'pyFormex Documentation'.

Vernon, L.B., Vernon, H.M. (1941) 'Producing Molded Articles such as Dentures from Thermoplastic Synthetic Resins (US Patent 2234993)'.

Wache, H.M., Tartakowska, D.J., Hentrich, A., Wagner, M.H. (2003) 'Development of a polymer stent with shape memory effect as a drug delivery system', *Journal Materials Science: Materials in Medicine*, 14, 109–12.

Wahl, A.M. (1944) *Mechanical Springs*, 1st ed, Penton Pub. Co.: Cleveland, Ohio, USA.

Wallsten, H.I. (1987) 'Prosthesis comprising an expansible or contractile tubular body (US Patent 4655771)'.

Wallsten, H.I., Imbert, C. (1991) 'Self-expanding prosthesis (US Patent 5061275)'.

Wang, R., Ravi-Chandar, K. (2004) 'Mechanical Response of a Metallic Aortic Stent—Part I: Pressure-Diameter Relationship', *Journal of Applied Mechanics*, 71(5), 697.

Wang, Z., Li, N., Li, R., Li, Y., Ruan, L. (2014) 'Biodegradable intestinal stents: A review', *Progress in Natural Science: Materials International*, 24(5), 423–432.

White, C.J., Ramee, S.R., Collins, T.J. (1994) 'Elective placement of the Wiktor stent after coronary angioplasty', *American Journal of Cardiology*, 1;74(3), 274–6.

Wholey, M.H., Ender, A.F. (2007) 'Designing the Ideal Stent', *Endovascular Today*, (March), 1–6.

Wijns, W., Pyxaras, S. a. (2012) 'Self-Expanding Stents for Primary Percutaneous Coronary Intervention During Acute Myocardial Infarction', *JACC: Cardiovascular Interventions*, 5(12), 1220–1222.

Wiktor, D.M. (1989) 'Intravascular radially expandable stent and method of implant (US Patent 4886062)'.

Wilson, G.E., Walshaw, M.J., Hind, C.R. (1996) 'Treatment of large airway obstruction in lung cancer using expandable metal stents inserted under direct vision via the fibreoptic bronchoscope.', *Thorax*, 51(3), 248–252.

Wineman, A.S., Rajagopal, K.R. (2000) *Mechanical Response of Polymers: An Introduction*, Cambridge University Press: Cambridge, England.

Wischke, C., Neffe, A.T., Steuer, S., Lendlein, A. (2009) 'Evaluation of a degradable shape-memory polymer network as matrix for controlled drug release', *Journal of Controlled Release*, 138(3), 243–250.

Wood, D.E. (2001) 'Airway Stenting', *Chest Surgery Clinics of North America*, 11(4), 841–60.

Yuan, T., Zheng, R., Yu, J., Edmonds, L., Wu, W., Cao, J., Gao, F., Zhu, Y., Cheng, Y., Cui, W. (2016) 'Fabrication and evaluation of polymer-based esophageal stents for benign esophagus stricture insertion', *RSC Adv.*, 6(20), 16891–16898.

Záhora, J., Bezrouk, A., Hanus, J. (2007) 'Models of stents - comparison and applications', *Physiological research / Academia Scientiarum Bohemoslovaca*, 56 Suppl 1, S115-21.

Zhang, Q., Beale, D., Adanur, S., Broughton, R.M., Walker, R.P. (1997) 'Structural Analysis of a Two-dimensional Braided Fabric', *Journal of the Textile Institute*, 88(1), 41–52.

Zhao, H., Humbeeck, J. Van, Sohier, J., De Scheerder, I. (2002) 'Electrochemical polishing of 316L stainless steel slotted tube coronary stents', *Journal of Materials Science: Materials in Medicine*, 13(10), 911–6.

Zhao, H., Liu, Y., Ni, X., Xia, F., Zhang, X. (2013) 'Mechanical Performance of Cup-spherical-shaped and Straight Form Braided Esophageal Stent', *TELKOMNIKA*, 11, 6657–63.

Zhao, S., Liu, X. (Cheryl), Gu, L. (2012) 'The Impact of Wire Stent Fabrication Technique on the Performance of Stent Placement', *Journal of Medical Devices*, 6(1), 11007.

Appendix 1
Stent Materials

Appendix 1.1 316L Stainless Steel

316L Stainless Steel is a low-carbon molybdenum-bearing austenitic stainless steel with the chemical composition denoted in Table 16. The addition of molybdenum and nickel content gives the alloy a superior resistance to corrosion. The alloy, with the mechanical properties depicted in Table 17, offers high tensile strength and excellent formability.

Table 16: 316L Stainless Steel chemical composition.

Material	Fe	Co	Cr	Ni	Mo	S	Mn	Si	C
316L Stainless Steel[1]	61.9-72 % As balance	0.045 % max	16-18%	10-14%	2.0-3.0%	0.03 % max	2.0% max	0.75 % max	0.03 % max

Table 17: 316L Stainless Steel mechanical properties.

Property	Yield Strength (MPa)	Ultimate Tensile Strength (MPa)	Tensile Modulus (GPa)	Elongation (%) in 50mm	Hardness	
					Rockwell B	Brinell
316L Stainless Steel	235	560	193	55	79	146

[1] MatWeb (2017b)

Appendix 1.2 Cobalt Alloys

Cobalt Alloy MP35N is a Nickel-Cobalt base alloy with a unique combination of properties: high strength, outstanding corrosion resistance and fatigue resistance. Table 18 presents its chemical composition, while in Table 19 the main mechanical characteristics are shown.

Table 18: Cobalt Alloy MP35N chemical composition.

Material	Fe	Co	Cr	Ni	Mo	Ti	Mn	Si	C
Cobalt Alloy[2]	1.0 % max	33%	19-21%	33-37%	9-10.5 %	1.0% max	0.15 % max	0.15 % max	0.025 % max

Table 19: Cobalt Alloy MP35N mechanical properties.

Property	Yield Strength (MPa)	Ultimate Tensile Strength (MPa)	Modulus of Elasticity (GPa)	Poisson ratio	Shear Modulus (GPa)	Elongation (%)
Cobalt Alloy	1620	1931	234.8	0.226	80.95	11

ASTM F1058, marketed as Phynox, is a Cobalt-Chromium-Nickel alloy with excellent biocompatibility and corrosion resistance. Its chemical composition indicated in Table 20 and mechanical properties are presented in Table 21.

Table 20: Phynox wire chemical composition.

Material	Fe	Co	Cr	Ni	Mo	Mn
Phynox[3]	11.5-20.5% As balance	39-41%	19-21%	14-16%	6.0-8.0%	1.5-2.5%

[2] MatWeb (2017b)
[3] MatWeb (2017)

Table 21: Phynox mechanical mroperties.

Property	Yield Strength (MPa)	Ultimate Tensile Strength (MPa)	Modulus of Elasticity (GPa)	Poisson ratio	Shear Modulus (GPa)
Phynox	1900	2200	203.4	0.32	77

Appendix 1.3 Nitinol

Nitinol is a near equiatomic shape memory alloy (SMA) utilised extensively in the medical engineering world due to its amazing shape-memory effect, superelasticity, biocompatibility and fatigue resistance properties. Nitinol chemical composition is depicted in Table 22. Mechanical properties are presented in Table 14.

Table 22: Nitinol wire chemical composition.

Material	C	Fe	Ni	O	Ti
Nitinol[4] (high strength, superelastic)	0.05% max	0.05% max	55.4 - 56.4%	0.05% max	43.54 - 44.6%

[4] MatWeb (2016)

Materials and Design
2017, 121 pp. 143-153
Viscoelastic braided stent: Finite element modelling and validation of crimping behaviour
Shanahan, Camelia, Tofail, Syed A.M, Tiernan, Peter
http://dx.doi.org/10.1016/j.matdes.2017.02.044

Appendix 2
BraidedStent.py

```
1  # $Id: 954dbe2 on Mon Mar 25 13:11:26 2013 +0100 by Benedict
Verhegghe $
2  ##
3  ##  This file is part of pyFormex 0.9.0  (Mon Mar 25 13:52:29 CET
2013)
4  ##  pyFormex is a tool for generating, manipulating and transforming
3D
5  ##  geometrical models by sequences of mathematical operations.
6  ##  Home page: http://pyformex.org
7  ##  Project page:  http://savannah.nongnu.org/projects/pyformex/
8  ##  Copyright 2004-2012 (C) Benedict Verhegghe
(benedict.verhegghe@ugent.be)
9  ##  Distributed under the GNU General Public License version 3 or
later.
10 ##
11 ##
12 ##  This program is free software: you can redistribute it and/or
modify
13 ##  it under the terms of the GNU General Public License as published
by
14 ##  the Free Software Foundation, either version 3 of the License, or
15 ##  (at your option) any later version.
16 ##
17 ##  This program is distributed in the hope that it will be useful,
18 ##  but WITHOUT ANY WARRANTY; without even the implied warranty of
19 ##  MERCHANTABILITY or FITNESS FOR A PARTICULAR PURPOSE.  See the
20 ##  GNU General Public License for more details.
21 ##
22 ##  You should have received a copy of the GNU General Public License
23 ##  along with this program.  If not, see
http://www.gnu.org/licenses/.
24 ##
25
26 """Braided Stent
27 This file was developed by Camelia Shanahan by rewriting the
WireStent.py
28 demo file available on pyFormex. It is intended only for educational
purposes.
29
30 level = 'normal'
31 topics = ['geometry']
32 techniques = ['dialog', 'persistence', 'color']
33 """
34 from __future__ import print_function
35 _status = 'checked'
36 _level = 'normal'
37 _topics = ['geometry']
38 _techniques = ['dialog', 'persistence', 'color']
39
```

```
class DoubleHelixStent(object):
    """Constructs a double helix braided stent.

    A stent is a tubular shape such as used for opening obstructed
    blood vessels. This stent is made from sets of wires spiralling
    in two directions.
    The geometry is defined by the following parameters:
      L  : approximate length of the stent
      De : external diameter of the stent
      D  : average stent diameter
      d  : wire diameter
      be : pitch angle (degrees)
      p  : pitch
      nx : number of wires in one spiral set
      ny : number of modules in axial direction
      ds : extra distance between the wires (default is 0.0 for
           touching wires)
      dz : maximal distance of wire centre to average cylinder
      nb : number of elements in a strut (a part of a wire between two
           crossings), default 4
    The stent is created around the z-axis.
    By default, there will be connectors between the wires at each
    crossing. They can be switched off in the constructor.
    The returned formex has one set of wires with property 1, the
    other with property 3. The connectors have property 2. The wire
    set with property 1 is winding positively around the z-axis.
    """
    def __init__(self,De,L,d,nx,be,ds=0.0,nb=4,connectors=True):
        """Create the Braided Stent."""
        D = De - 2*d - ds
        r = 0.5*D
        dz = 0.5*(ds+d)
        p = pi*D*tand(be)
        nx = int(nx)
        ny = int(round(nx*L/p))  # The actual length may differ a bit
from L
        # a single bumped strut, oriented along the x-axis
        bump_z=lambda x: 1.-(x/nb)**2
        base = Formex('l:1').replic(nb,1.0).bump1(2,[0.,0.,dz],bump_z,0)
        # scale back to size 1.
        base = base.scale([1./nb,1./nb,1.])

        # create bent strut (stent ends)
        BS = base.mirror(0).translate(0,-1.).setProp(4)
        BS += BS.rotate(180.,2).reflect(2)
        BS = BS.translate(1,-
sqrt(2.)).cylindrical([1,0,2],[1.,90./4,0.5]).rotate(90.,2).translate(0,2.)

        # NE and SE directed struts
        NE = base.shear(1,0,1.)
        SE = base.reflect(2).shear(1,0,-1.)
        NE.setProp(1)
        SE.setProp(3)
        # a unit cell of crossing struts
        cell1 = (NE+SE).rosette(2,180)
        # add a connector between first points of NE and SE
        if connectors:
            cell1 += Formex([[NE[0][0],SE[0][0]]],2)
```

```
98          # create its mirror
99          cell2 = cell1.reflect(2).translate([2.,2.,0.])
100         base = cell1 + cell2
101
102         # reposition to base to origin [0,0]
103         base = base.translate(-base.bbox()[0])
104
105         # Create the full pattern by replication
106         dx,dy = base.bbox()[1][:2]
107         F = base.replic2(nx,ny,dx,dy)
108
109         self.F = F
110         self.ny = ny
111
112     def getFormex(self):
113         """Return the Formex with all bar elements.
114
115         This includes the elements along all the wires, as well as the
116         connectors between the wires.
117         """
118         return self.F
119
120     def getWireAxes(self):
121         """Return the wire axes as curves.
122
123         The return value is two lists of curves (PolyLines),
representing the
124         individual wire axes for each wire direction.
125         """
126         import connectivity
127         M = self.F.toMesh()
128         ML = [ M.withProp(i) for i in [1,3] ]
129         wires = [ connectivity.connectedLineElems(Mi.elems) for Mi in
ML ]
130         wireaxes = [ [ Formex(M.coords[wi]).toCurve() for wi in wiresi
] for wiresi in wires ]
131         return wireaxes
132
133
134       def run():
135     """Ask the user for data and show the corresponding Wire Stent."""
136     wireframe()
137     reset()
138
139     res = askItems([
140         _I('L',51.,text='Length of the stent'),
141         _I('D',22.,text='Diameter of the stent'),
142         _I('n',15 ,text='Total number of wires'),
143         _I('b',40.,text='Pitch angle of the wires'),
144         _I('d',0.62,text='Diameter of the wires'),
145         _I('show',itemtype='radio',choices=['Formex','Curves']),
146         ])
147
148     if not res:
149         return
150
151     globals().update(res)
152
153     H = DoubleHelixStent(D,L,d,n,b)
154     clear()
```

Appendix 3
Material Models

Appendix 3.1 PDO Viscoelastic Material Model

Table 23: Conversion of tensile creep compliance into normalised shear creep compliance based on the results of the PDO tensile creep experiment. The values are reported as mean ± standard deviation (SD).

Time (s)	Tensile Creep Compliance $D(t) \pm SD1$	Shear Creep Compliance $J(t) \pm SD2$	Normalised Shear Creep Compliance $j(t) \pm SD3$
1	1.22E-03 ± 1.22E-04	3.53E-03 ± 0.705	1 ± 0.0
600	1.33E-03 ± 5.83E-05	3.85E-03 ± 0.773	1.1 ± 0.069
1200	1.37E-03 ± 2.67E-05	3.97E-03 ± 0.798	1.13 ± 0.097
1800	1.4E-03 ± 2.35E-05	4.05E-03 ± 0.814	1.15 ± 0.104
2400	1.41E-03 ± 2.22E-05	4.09E-03 ± 0.822	1.17 ± 0.106
3000	1.42E-03 ± 1.82E-05	4.12E-03 ± 0.829	1.18 ± 0.109
3600	1.44E-03 ± 7.11E-06	4.16E-03 0.838	1.19 ± 0.124
5400	1.45E-03 ± 6.41E-06	4.21E-03 ± 0.847	1.20 ± 0.123
7200	1.46E-03 ± 1.18E-05	4.25E-03 ± 0.855	1.22 ± 0.125
10800	1.49E-03 ± 1.18E-05	4.32E-03 ± 0.869	1.23 ± 0.122
14400	1.50E-03 ± 8.89E-06	4.36E-03 ± 0.877	1.24 ± 0.124
18000	1.51E-03 ± 2.22E-05	4.39E-03 ± 0..883	1.25 ± 0.121
36000	1.56E-03 ± 3.55E-05	4.52E-03 ± 0.91	1.29 ± 0.128
72000	1.58E-05 ± 3.20E-05	4.58E-03 ± 0.922	1.31 ± 0.124

Appendix 3.2 Nitinol Viscoelastic Material Model

Table 24: Conversion of tensile creep compliance into normalised shear creep compliance based on the results of the Nitinol tensile creep data from the literature (Raj and Noebe 2013).

Time (s)	Tensile Creep Compliance $D(t)$	Shear Creep Compliance $J(t)$	Normalised Shear Creep Compliance $j(t)$
1	0.000024	0.00006384	1
12000	0.0000249	0.000066234	1.0375
24000	0.00002535	0.000067431	1.05625
48000	0.00002586	6.87876E-05	1.0775
96000	0.00002605	0.000069293	1.085416667
192000	0.000026125	6.94925E-05	1.088541667
384000	0.000026175	6.96255E-05	1.090625
768000	0.0000262	0.000069692	1.091666667
153600	0.00002625	0.000069825	1.09375
3072000	0.00002629	6.99314E-05	1.095416667
6144000	0.0000263	0.000069958	1.09833333

Appendix 4
Publications

Materials and Design
2017, 121 pp. 143-153
Viscoelastic braided stent: Finite element modelling and validation of crimping behaviour
Shanahan, Camelia, Tofail, Syed A.M, Tiernan, Peter
http://dx.doi.org/10.1016/j.matdes.2017.02.044